

NAG1-1522

IN-05-CR

49859

SAILPLANE GLIDE PERFORMANCE AND CONTROL USING

FIXED AND ARTICULATING WINGLETS

P. 100

A Thesis

by

JAMES DAVID COLLING

Submitted to the Office of Graduate Studies of
Texas A&M University
in partial fulfillment of the requirement for the degree of

MASTER OF SCIENCE

May 1995

Major Subject: Aerospace
College of Engineering

(NASA-CR-198579) SAILPLANE GLIDE
PERFORMANCE AND CONTROL USING FIXED
AND ARTICULATING WINGLETS M.S.
Thesis (Texas A&M Univ.) 100 p

N95-27180

Unclassified

G3/05 0049859

104 P 403904

SAILPLANE GLIDE PERFORMANCE AND CONTROL USING
FIXED AND ARTICULATING WINGLETS

A Thesis

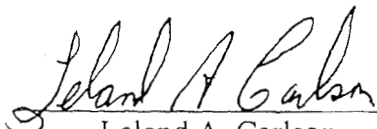
by

JAMES DAVID COLLING

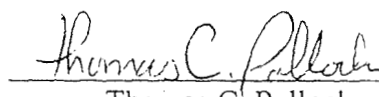
Submitted to Texas A&M University
in partial fulfillment of the requirements
for the degree of

MASTER OF SCIENCE

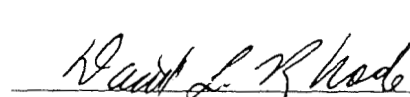
Approved as to style and content by:



Leland A. Carlson
(Chairman of Committee)



Thomas C. Pollock
(Member)



David L. Rhode
(Member)



Donald T. Ward
(Head of Department)

May 1995

Major Subject: Aerospace
College of Engineering

ABSTRACT

Sailplane Glide Performance and Control Using Fixed
and Articulating Winglets. (May 1995)

James David Colling, B.S., Texas A&M University

Chair of Advisory Committee: Dr. Leland A. Carlson

An experimental study was conducted to investigate the effects of controllable articulating winglets on glide performance and yawing moments of high performance sailplanes. Testing was conducted in the Texas A&M University 7x10 foot Low Speed Wind Tunnel using a full-scale model of the outboard 5.6 feet of a 15 meter class high performance sailplane wing. Different wing tip configurations could be easily mounted to the wing model. A winglet was designed in which the cant and toe angles as well as a rudder on the winglet could be adjusted to a range of positions. Cant angles used in the investigation consisted of 5, 25, and 40 degrees measured from the vertical axis. Toe-out angles ranged from 0 to 22.5 degrees. A rudder on the winglet was used to study the effects of changing the camber of the winglet airfoil on wing performance and wing yawing moments. Rudder deflections consisted of -10, 0, and 10 degrees. Test results for a fixed geometry winglet and a standard wing tip are presented to show the general behavior of winglets on sailplane wings, and the effects of boundary-layer turbulators on the winglets are also presented. By tripping the laminar boundary-layer to turbulent before laminar separation occurs, the wing performance was increased at low Reynolds numbers. The effects on the lift and drag, yawing moment, pitching moment, and wing root bending

moment of the model are presented. Oil flows were used on the wing model with the fixed geometry winglet and the standard wing tip to visualize flow directions and areas of boundary layer transition.

A cant angle of 25 degrees and a toe-out angle of 2.5 degrees provided an optimal increase in wing performance for the cant and toe angles tested. Maximum performance was obtained when the winglet rudder remained in the neutral position of zero degrees. By varying the cant, toe, and rudder angles from their optimized positions, wing performance decreases. Although the winglet rudder proved to be more effective in increasing the yawing moment compared to varying the cant and toe angles, the amount of increased yawing moment was insignificant when compared to that produced by the vertical tail. A rudder on the winglet was determined to be ineffective for providing additional yaw control.

ACKNOWLEDGMENT

The author would like to thank the committee members, Dr. Thomas C. Pollock, Dr. David L. Rhode, and especially Dr. Leland A. Carlson for their guidance and assistance and to Dr. Kenneth D. Korkan, who was the original advisor on this project. Special appreciation is given to Mr. Oran W. Nicks for his guidance and assistance during the investigation. Thanks are also given to Mr. Greg G. Steen, and all the Texas A&M wind tunnel staff for their assistance. The author would like to thank Mr. Peter C. Masak for allowing the use of his winglet design for my research and for sponsoring the construction of the wind tunnel model. I would like to thank Dr. Michael Card for sponsoring this research from NASA Langely Research Center through grant number NAG 1-1522.

TABLE OF CONTENTS

	Page
ABSTRACT	iii
ACKNOWLEDGMENTS	v
TABLE OF CONTENTS	vi
LIST OF FIGURES	vii
NOMENCLATURE	xiii
INTRODUCTION	1
WIND TUNNEL MODEL	7
OIL FLOW VISUALIZATION RESULTS	8
FIXED GEOMETRY WINGLET RESULTS	13
ARTICULATING WINGLET RESULTS	19
SUMMARY AND CONCLUSIONS	27
REFERENCES	29
APPENDIX	30
VITA	87

LIST OF FIGURES

Figure	Page
1. Winglets Mounted on a High Performance Sailplane	30
2. High Performance Sailplane Being Towed by a Powered Aircraft	31
3. Geometry and Dimensions of Fixed Geometry Winglet	32
4. Winglet Relative Angle of Attack	33
5. Thrust and Side Component of Winglet Force Vector	34
6. The Effect of Winglets on the Wing Lift Distribution	35
7. Fixed Geometry Winglet and Standard Wing Tip Used During First Wind Tunnel Test	36
8. Winglet Rudder Angle	37
9. Definition of Toe and Cant Angles Presented in Results	38
10. Wind Tunnel Model Dimensions	39
11. Wing Model Installation and Wall Clearance	40
12. Flow Visualization of Standard Wing Tip Suction Side. $\alpha = 2.5^\circ, Q = 10.85 \text{ lb/ft}^2$	41
13. Flow Visualization of Standard Wing Tip Suction Side. $\alpha = 5.0^\circ, Q = 10.85 \text{ lb/ft}^2$	42
14. Flow Visualization of Standard Wing Tip Suction Side. $\alpha = 7.5^\circ, Q = 10.85 \text{ lb/ft}^2$	43
15. Flow Visualization of Standard Wing Tip Suction Side. $\alpha = 10.0^\circ, Q = 10.85 \text{ lb/ft}^2$	44

Figure	Page
16. Flow Visualization of Standard Wing Tip Pressure Side. $\alpha = 2.5^\circ, Q = 10.85 \text{ lb/ft}^2$	45
17. Flow Visualization of Standard Wing Tip Pressure Side. $\alpha = 0^\circ, Q = 40.6 \text{ lb/ft}^2$	46
18. Flow Visualization of Winglet Suction Side. $\alpha = 0^\circ, Q = 10.85 \text{ lb/ft}^2$	47
19. Flow Visualization of Winglet Suction Side. $\alpha = 0^\circ, Q = 40.6 \text{ lb/ft}^2$	48
20. Flow Visualization of Winglet Suction Side. $\alpha = 2.5^\circ, Q = 10.85 \text{ lb/ft}^2$	49
21. Flow Visualization of Winglet Suction Side. $\alpha = 5.0^\circ, Q = 10.85 \text{ lb/ft}^2$	50
22. Flow Visualization of Winglet Suction Side. $\alpha = 7.5^\circ, Q = 10.85 \text{ lb/ft}^2$	51
23. Flow Visualization of Winglet Suction Side. $\alpha = 10.0^\circ, Q = 10.85 \text{ lb/ft}^2$	52
24. Flow Visualization of Winglet Pressure Side. $\alpha = 0^\circ, Q = 10.85 \text{ lb/ft}^2$	53
25. Flow Visualization of Winglet Pressure Side. Laminar Separation $\alpha = 2.5^\circ, Q = 10.85 \text{ lb/ft}^2$	54
26. Flow Visualization of Winglet Pressure Side. Laminar Flow to 98 Percent. $\alpha = 10.0^\circ, Q = 10.85 \text{ lb/ft}^2$	55
27. Installation of Turbulator Strip on Pressure Side of Winglet Prevents Laminar Flow Separation	56
28. Installation of Turbulator Strip on Suction Side of Winglet Prevents Laminar Separation Bubble	57

Figure	Page
29. Drag Polar, Lift Curve, Side Force Curve, and Pitching Moment Coefficients for the Standard Wing Tip, Clean Winglet, and Turbulated Winglet. Reynolds Number $6.1 \times 10^5 \text{ ft}^{-1}$	58
30. Drag Polar, Lift Curve, Side Force Curve, and Pitching Moment Coefficients for the Standard Wing Tip, Clean Winglet, and Turbulated Winglet. Reynolds Number $8.2 \times 10^5 \text{ ft}^{-1}$	59
31. Lift to Drag Ratio for Standard Wing Tip, Clean Winglet , and Turbulated Winglet. Reynolds Number $6.1 \times 10^5 \text{ ft}^{-1}$	60
32. Lift to Drag Ratio for Standard Wing Tip, Clean Winglet , and Turbulated Winglet. Reynolds Number $8.2 \times 10^5 \text{ ft}^{-1}$	61
33. Climb Parameter for Standard Wing Tip, Clean Winglet , and Turbulated Winglet. Reynolds Number $6.1 \times 10^5 \text{ ft}^{-1}$	62
34. Climb Parameter for Standard Wing Tip, Clean Winglet , and Turbulated Winglet. Reynolds Number $8.2 \times 10^5 \text{ ft}^{-1}$	63
35. Rolling Moment for Standard Wing Tip, Clean Winglet , and Turbulated Winglet. Reynolds Number $6.1 \times 10^5 \text{ ft}^{-1}$	64
36. Rolling Moment for Standard Wing Tip, Clean Winglet , and Turbulated Winglet. Reynolds Number $8.2 \times 10^5 \text{ ft}^{-1}$	65
37. Drag Polar and Lift Curve of Baseline Comparison for the First and Second Wind Tunnel Test	66

Figure	Page
38. Effects of Cant Angle on the Drag Polar, Lift Curve, Side Force Curve, and Pitching Moment Coefficients at a Toe-Out Angle of 2.5 Degrees. Reynolds Number $5.2 \times 10^5 \text{ ft}^{-1}$	67
39. Effects of Toe-Out Angle on the Drag Polar, Lift Curve, Side Force Curve, and Pitching Moment Coefficients at a Cant Angle of 85 Degrees. Reynolds Number $5.2 \times 10^5 \text{ ft}^{-1}$	68
40. Effects of Winglet Rudder Angle on the Drag Polar, Lift Curve, Side Force Curve, and Pitching Moment Coefficients at a Cant Angle of 65 Degrees, Toe-Out Angle of 2.5 Degrees. Reynolds Number $5.2 \times 10^5 \text{ ft}^{-1}$	69
41. Effects of Winglet Rudder Angle on the Drag Polar, Lift Curve, Side Force Curve, and Pitching Moment Coefficients at a Cant Angle of 85 Degrees, Toe-Out Angle of 2.5 Degrees. Reynolds Number $5.2 \times 10^5 \text{ ft}^{-1}$	70
42. Effects of Cant Angle on the Lift to Drag Ratio at a Toe-Out Angle of 2.5 Degrees. Reynolds Number $5.2 \times 10^5 \text{ ft}^{-1}$	71
43. Effects of Toe-Out Angle on the Lift to Drag Ratio at a Cant Angle of 85 Degrees. Reynolds Number $5.2 \times 10^5 \text{ ft}^{-1}$	72
44. Effects of Winglet Rudder Angle on the Lift to Drag Ratio at a Cant Angle of 65 Degrees and Toe-Out angle 2.5 Degrees. Reynolds Number $5.2 \times 10^5 \text{ ft}^{-1}$	73

Figure	Page
45. Effects of Winglet Rudder Angle on the Lift to Drag Ratio at a Cant Angle of 85 Degrees and Toe-Out angle 2.5 Degrees. Reynolds Number $5.2 \times 10^5 \text{ ft}^{-1}$	74
46. Effects of Cant Angle on the Climb Parameter at a Toe-Out Angle of 2.5 Degrees. Reynolds Number $5.2 \times 10^5 \text{ ft}^{-1}$	75
47. Effects of Toe-Out Angle on the Climb Parameter at a Cant Angle of 85 Degrees. Reynolds Number $5.2 \times 10^5 \text{ ft}^{-1}$	76
48. Effects of Winglet Rudder Angle on the Climb Parameter. Cant Angle 65 Degrees. Toe-Out angle 2.5 Degrees. Reynolds Number $5.2 \times 10^5 \text{ ft}^{-1}$	77
49. Effects of Winglet Rudder Angle on the Climb Parameter. Cant Angle 85 Degrees. Toe-Out angle 2.5 Degrees. Reynolds Number $5.2 \times 10^5 \text{ ft}^{-1}$	78
50. Effects of Cant Angle on the Rolling Moment. Toe-Out Angle 2.5 Degrees. Reynolds Number $5.2 \times 10^5 \text{ ft}^{-1}$	79
51. Effects of Toe-Out Angle on the Rolling Moment. Cant Angle 85 Degrees. Reynolds Number $5.2 \times 10^5 \text{ ft}^{-1}$	80
52. Effects of Winglet Rudder Angle on the Rolling Moment. Cant Angle 65 Degrees. Toe-Out angle 2.5 Degrees. Reynolds Number $5.2 \times 10^5 \text{ ft}^{-1}$	81

Figure	Page
53. Effects of Winglet Rudder Angle on the Rolling Moment. Cant Angle 85 Degrees. Toe-Out angle 2.5 Degrees. Reynolds Number $5.2 \times 10^5 \text{ ft}^{-1}$	82
54. Effects of Cant Angle on the Yawing Moment at a Toe-Out Angle of 2.5 Degrees. Reynolds Number $5.2 \times 10^5 \text{ ft}^{-1}$	83
55. Effects of Toe-Out Angle on the Yawing Moment. Cant Angle 85 Degrees. Reynolds Number $5.2 \times 10^5 \text{ ft}^{-1}$	84
56. Effects of Winglet Rudder Angle on the Yawing Moment. Cant Angle 65 Degrees. Toe-Out angle 2.5 Degrees. Reynolds Number $5.2 \times 10^5 \text{ ft}^{-1}$	85
57. Effects of Winglet Rudder Angle on the Yawing Moment. Cant Angle 85 Degrees. Toe-Out angle 2.5 Degrees. Reynolds Number $5.2 \times 10^5 \text{ ft}^{-1}$	86

NOMENCLATURE

C_D	Drag Coefficient
C_L	Lift Coefficient
$C_L^{3/2}/C_D$	Climb Parameter
CM_p	Pitching Moment Coefficient
CM_Y	Yawing Moment Coefficient
CS	Side Force Coefficient
ft	Foot
lb	Pounds Force
L/D	Lift to Drag Ratio
mph	Miles per Hour, Statute
P	Power
Q	Dynamic Pressure
RC	Rate of Climb
S	Wing Surface Area
W	Weight
α	Angle of attack
η_p	Propeller Efficiency

INTRODUCTION

Winglets are vertically mounted, cambered wing extensions that are attached at the wing tips of aircraft to provide aerodynamic performance enhancements such as improved lift to drag ratio. Figure 1 shows a high performance sailplane, called a Schreder HP-18, with winglets installed. An experimental investigation was conducted to determine whether the glide performance of high performance sailplanes can be further improved over that of fixed geometry winglets by controlling the toe, cant, and winglet rudder angles in flight. Another purpose of this investigation was to study the effect of asymmetric control of the winglets on the yawing moment of the aircraft.

Modern high performance sailplane designs achieve lift to drag ratios (L/D) which range from 40/1 to 60/1. These glide ratios are accomplished through the extensive use of composite materials and natural laminar flow airfoils. For the fifteen-meter racing class of sailplanes, the L/D will typically range from 42/1 at the best L/D speed of 70 mph to 30/1 at a cruise speed of 105 mph. At a gross weight of 1188 lbs, the drag of the sailplane at the best L/D speed would amount to 28 lbs. Since the total drag of a sailplane is small compared to the lift, a small decrease in the amount of drag can produce a large increase in the lift to drag ratio. Methods of obtaining drag reduction include sealing all gaps along the control surfaces, sealing pushrod exits, and removing the roughness and waviness from the wing surface. Winglets have been shown both in flight testing and wind tunnel testing to improve the glide ratio and the climb rate.

High performance sailplanes can fly great distances without any form of mechanical propulsion except for an initial tow to a typical altitude of 2,000 feet by a powered aircraft, as shown in Figure 2, or a launch by a winch or automobile. Cross country flight in sailplanes is accomplished by climbing in rising air currents called thermals and cruising at speeds around 105 mph between thermals. To maximize the average speed of the sailplane on a cross country flight, the glide ratio of the sailplane should be as high as possible for the entire range of airspeeds encountered. During sailplane racing competitions of 15-meter class sailplanes, the ratio of cruising flight to climbing flight is generally in the range of 70 percent cruising and 30 percent climbing. Therefore, improving the climb rate of sailplanes is also important. The climb equation¹ for a propeller driven powered aircraft is given by,

$$RC = 33,000 \left(\frac{\eta_p}{W/P} - \{(W/S)^{1/2}/19(C_L^{3/2}/C_D) \} \right) \quad (1)$$

Where RC is the rate of climb in feet per minute, W is the weight of the aircraft, S is the wing surface area, η_p is the propeller efficiency, and P is the power. To maximize the rate of climb for a powered aircraft, the climb parameter, $C_L^{3/2}/C_D$, should be as high as possible. Similarly for sailplanes, if the value of $C_L^{3/2}/C_D$ is increased from that obtained from a sailplane without winglets, the rate of climb in a thermal will increase for the sailplane with winglets. The percentage difference in $C_L^{3/2}/C_D$ between the sailplane with winglets and the one without equals the percentage change in rate of climb. As mentioned above, to increase the lift to drag ratio of a sailplane it is more effective to reduce the amount of drag. However, for the climb parameter to increase, an increase in the lift coefficient has more of an effect than reducing the drag since the coefficient of lift is

raised to the three halves power.

The geometry of winglets is defined by cant angle, toe angle, sweep angle, twist distribution, and airfoil selection. Cant angle is defined as the angle of the winglet surface from the vertical axis. Figure 3 shows the geometry which defines the winglet and the dimensions of the fixed geometry winglet used for the investigation. Proper design of winglets can provide an increase in the aerodynamic efficiency of aircraft by reducing the lift induced drag of the wing²⁻³. An inflow of air is created at the wing tip by a wing tip vortex, as shown in Figure 4, which changes the relative angle of attack of the winglet airfoil with respect to the freestream airflow. As a result, a force directed toward the fuselage and in the forward direction is produced by the winglet as shown in Figure 5. This "thrust" component of the winglet force accounts for part of the total drag reduction of the aircraft⁴. With the installation of winglets, the wing tip boundary condition no longer requires that the lift be reduced to zero at the wing tip. Thus, as portrayed in Figure 6, the lift distribution of the wing can be changed such that the same amount of lift will be produced at a lower angle of attack, which reduces the wing induced drag thus reducing the total drag of the aircraft as described by Nicks⁵.

For this investigation, two separate wind tunnel tests were conducted. The first test studied the general behavior of fixed geometry winglets for sailplanes, and performance comparisons were made to a standard sailplane wing tip. The fixed geometry winglet and the standard wing tip tested are shown in Figure 7. Some tests were also conducted without a contoured wing tip to provide a baseline comparison for future testing.

A series of tests were conducted with the fixed geometry winglet and the standard wing tip for a range of Q values. Force and moment balance data were obtained to measure wing performance with different wing tip configurations, and oil film flow visualization was conducted with the fixed geometry winglet and standard wing tip to investigate surface flow directions near the wing tip and to locate areas of boundary layer transition and separation. Low Reynolds number effects such as laminar separation bubbles and laminar flow separation can occur on the winglet surfaces at low airspeeds. By forcing the laminar boundary-layer to become turbulent at the proper location by means of a turbulator strip, winglet performance can often be improved. Thus, the effects of turbulators on the winglet surface were investigated using both flow visualization and force and moment balance data. The turbulator strip used for the test was 14 mil 30 degree zig-zag tape. This type of turbulator is used on most high performance sailplanes to prevent laminar separation bubbles from forming on the bottom surface of the wing.

With increased airspeed winglets become less effective in drag reduction because the lift coefficient of the wing is less and there is a corresponding reduction in the amount of induced drag produced by the wing². Therefore, at higher airspeeds the added surface area of the winglet will add to the skin friction drag causing a reduction in glide performance as compared to an aircraft without winglets³. As a result, there is always a trade off between low speed and high speed performance. The point at which the winglets begin to increase the drag as compared to the same aircraft with a standard wing tip is called the crossover point, and for a good winglet design, the crossover point will be at an airspeed that is typically not reached in flight.

The second wind tunnel test was directed towards the investigation of various winglet cant and toe angles on wing performance and to determine whether the crossover point could be raised or eliminated.. An articulating winglet was designed to have the capability of changing the toe and cant angles. The effect of deflecting a rudder on the winglet was also investigated to determine whether improved glide and climb performance could be achieved and whether the yawing moment produced by the winglet was sufficient to provide yaw control. As shown on Figure 8, a rudder on the winglet could be deflected from a neutral position of zero degrees to +10 and -10 degrees. A positive deflection was outward and increased the camber of the winglet airfoil while a negative deflection was inward and decreased the camber of the winglet airfoil.

Toe angle is defined as either toe-in or toe-out. Toe angles are measured from the winglet airfoil chord line with respect to a line parallel to the aircraft centerline. For toe-out, the leading-edge of the airfoil is moved away from the aircraft centerline and the trailing-edge moves toward the aircraft centerline. As depicted on Figure 9, the zero degree toe angle position of the winglet is parallel to the aircraft centerline, and toe angles are measured about the pivot point of the articulating mechanism. The articulating winglet was designed such that when the winglet was at a toe-out angle of 2.5 degrees, the leading-edge and trailing-edge of the winglet lined up with the fairing that covered the articulating mechanism.

In this investigation, cant angle was referenced from the horizontal axis as opposed to the standard definition which measures the angle from the vertical axis. In the actual tests, cant angle measurements were taken from an axis parallel to the top surface of the

wing, as shown in Figure 9. True cant angle would therefore be 90 degrees minus the referenced cant angle. Cant angles used for this investigation consisted of 50, 65, and 85 degrees from horizontal measured from top surface of the wing model. For the remainder of this investigation the cant angle will be defined as that measured from the horizontal axis.

Due to unforeseen structural problems with the articulating winglet mechanism, all the test cases involving toe-out angles other than the neutral position of 2.5 degrees were conducted at a cant angle of 85 degrees. At the 85 degree position, the winglet mechanism was against its physical stop which prevented undue deflection of the winglet. For toe angles near the neutral position, the winglet could be forced to remain in its current position at any cant angle by using tape. Thus, to prevent excessive deflections, the wind tunnel dynamic pressure was limited to 8 lb/ft² for the duration of the test.

WIND TUNNEL MODEL

A fiberglass composite wing section was built using an extruded polystyrene foam core covered with a fiberglass skin. The natural laminar flow Wortmann 79-K-144 airfoil, which is used on many German sailplane designs, was used for the wing model. The wing planform used for the model was the outboard 5.6 feet of an elliptic leading-edge 15-meter class sailplane wing, and the dimensions of the model are shown in Figure 10. The fixed geometry winglet used in this study was designed by Mr. Peter Masak. In addition, a standard wing tip from a German sailplane design called a Discus was used during the first series of wind tunnel tests to provide performance comparisons with the fixed geometry winglet.

The wing model, as depicted in Figure 11, was mounted vertically in the Texas A&M 7 x 10 foot Low Speed Wind Tunnel facility. The proximity of the tip to the ceiling was a concern in the model design, but it was decided to build the model as large as possible so that the loads measured would be high. A tip clearance of 1.4 feet was provided between the outboard surface of the winglet and the ceiling of the wind tunnel for the fixed geometry winglet, but clearance with the articulating winglet at a cant angle of 50 degrees was less than a foot. At cant angles of 65 and 85 degrees, the wall clearance was in the same range as the fixed geometry winglet. The root of the model was mounted such that the floor clearance was 0.1 inch. Wind tunnel blockage corrections and wall corrections were made using standard wind tunnel correction procedures described by Rae and Pope⁶. Forces and moments were reduced to coefficient form so that direct comparisons could be made between different wing tip configurations.

OIL FLOW VISUALIZATION RESULTS

Oil flow visualization of the standard wing tip and the fixed geometry winglet was conducted during the first series of wind tunnel tests. Surface flows and areas of boundary layer transition and separation were investigated in the wing tip region. Areas of laminar and turbulent flow were determined by the presence of turbulent spots as described by Schlichting⁷. These turbulent spots propagated downstream to form turbulent wedges, which were formed by particulates in the oil film that trip the laminar boundary-layer to turbulent prematurely. As measured by Schubauer and Klebanoff⁸, a turbulent wedge on a flat plate spreads at a 22.6 degree included angle. During the flow visualization testing, turbulent wedges formed at angles close to those found on flat plates. Areas of laminar flow were characterized by the oil film streaking back to the transition point, but in areas of turbulent flow, the oil film was smooth and uniform due to turbulent mixing in the boundary-layer. When a turbulent wedge propagated to an area of normal transition, it first spread at the 22.6 degree included angle, then stopped when the flow became fully turbulent and remained parallel to the other streamlines. In areas of laminar separation, the turbulent wedge regions would remain attached through the separated flow because of the additional energy provided by the turbulent flow. Separated flow was characterized by the following observations: brush marks from the application of the oil remaining undisturbed through the duration of the test, oil running down to the floor of the wind tunnel due to gravity, backflow observed during the test, or oil collecting in areas of separated flow during the test.

A series of oil film flow visualization test cases was run for the standard wing tip.

At an angle of attack of 2.5 degrees and a dynamic pressure of 10.85 lb/ft^2 , the point of transition on the top surface or suction side of the wing was located at 73 percent of chord for most of the wing as shown in Figure 12. Near the wing tip, however, the point of transition moved forward to 49 percent and a laminar separation bubble was present in this area. The streamlines at the wing tip were measured to be 20 degrees inward from the freestream flow indicating the direction of the inflow at the wing tip surface. Figure 12 also indicates the presence of a turbulent wedge that was used to distinguish areas of laminar and turbulent flow. When the angle of attack was increased to 5 degrees, the point of transition moved forward to around 50 percent of chord as shown in Figure 13. In this case, the transition was fairly uniform along the entire wing, but inflow was again measured to be 20 degrees on the top surface near the wing tip. At an angle of attack of 7.5 degrees, the point of transition made a sudden jump to the leading edge as indicated by the white arrow on the left side of Figure 14. The sudden jump of the boundary-layer transition was a result of a leading-edge suction peak⁹. This behavior is typical of natural laminar flow airfoils. Premature separation of the turbulent boundary-layer near the trailing-edge, which is indicated by the white arrow on the right side of Figure 14, was a result of the forward shift of the transition. Backflow was evident on the upper aileron surface during testing. Similar to the 2.5 degree angle of attack case, the transition area near the wing tip occurred at 50 percent of chord. Streamlines at the wing tip indicate the inflow on the top surface of the wing being at 15 degrees. At a 10 degree angle of attack, transition was at the leading-edge along most of the wing and premature turbulent separation occurred ahead of the aileron as shown in Figure 15. A large amount of

backflow was present on the aileron top surface during testing. Again, the streamlines at the wing tip were measured to be at an inward flow angle of 15 degrees.

On the bottom surface or pressure side of the wing, transition was measured to be at 63 percent of chord when at an angle of attack of 2.5 degrees and a dynamic pressure of 10.85 lb/ft^2 , Figure 16. A strong laminar separation bubble, characterized by brush marks from the application of the oil remaining undisturbed during the duration of the test, was present on the bottom surface for all cases at a dynamic pressure of 10.85 lb/ft^2 . When the angle of attack was increased, the point of transition moved further back by just a few percentage points. A wing tip skid was installed on the lower surface of the wind tunnel model to resemble the typical wing tip configuration found on most sailplanes. This tip skid appeared to create a region of flow which resembles a junction vortex. At a higher Reynolds number with a Q of 40.6 lb/ft^2 , the laminar separation bubble on the bottom surface was no longer present, Figure 17. The point of transition appeared to move further back on the pressure side although the presence of numerous turbulent wedges, which are highlighted in Figure 17, made accurate measurement difficult.

A similar series of flow visualization tests was conducted for the fixed geometry winglet with similar results. At an angle of attack of 0 degrees and a dynamic pressure of 10.85 lb/ft^2 , boundary-layer transition was measured at 70 percent of chord on the suction side of the wing as shown in Figure 18. A laminar separation bubble was present on the winglet surface in which transition began at 53 percent of chord at the root of the winglet and 40 percent of chord at the winglet tip. For the same configuration at a higher dynamic pressure of 40.6 lb/ft^2 , there was no longer a laminar separation bubble present on the

winglet, Figure 19. Boundary-layer transition on the wing was measured at 75 percent of chord on the wing at the higher Reynolds number.

At an angle of attack of 2.5 degrees and a dynamic pressure of 10.85 lb/ft², the boundary-layer transition location on the wing top surface moved forward to 66 percent of chord as shown in Figure 20. This transition location was further forward than that of the standard wing tip at the same conditions which indicates an increased lift for the same angle of attack. Numerous turbulent wedges were present on the upper surface of the wing and are highlighted. The laminar separation bubbles present on the suction side of the wing and winglet are indicated by the black arrows. Transition on the suction side of the winglet moved forward to 50 percent at the root and 35 percent at the winglet tip.

At a 5 degree angle of attack, boundary layer transition on the wing was around 50 percent of chord as shown in Figure 21. The boundary-layer transition on the winglet moved forward to 46 percent at the root and 25 percent at the winglet tip.

When the angle of attack was increased to 7.5 degrees, the point of boundary-layer transition moved to the leading-edge of the wing as shown in Figure 22. Near the junction of the wing and winglet, the point of transition moved back to 50 percent of chord. Premature turbulent separation occurred before the aileron along the trailing-edge of the wing.

At a 10 degree angle of attack, turbulent separation was more pronounced and backflow was visible on the aileron top surface during testing as shown in Figure 23. Transition on the winglet surface appeared to stabilize at 20 percent of chord.

On the bottom surface of the wing at an angle of attack of 0 degrees, the point of

transition was a fairly constant 67 percent of chord, Figure 24. With increased angle of attack, the point of transition moved back only by a few percentage points.

Laminar separation on the pressure side of the winglet was measured at 90 percent of chord at an angle of attack of 2.5 degrees and a dynamic pressure of 10.85 lb/ft^2 as shown in Figure 25. When the angle of attack was increased to 10 degrees, the laminar separation point on the winglet moved back to very near the trailing-edge as shown in Figure 26. The surface streamlines at the junction of the wing and winglet can be seen to wrap around on the bottom surface as they apparently flow from the junction vortex created by the wing tip skid as mentioned previously. With the installation of a turbulator strip on pressure side of the winglet, the laminar boundary-layer was tripped to turbulent in a controlled manner before separation occurred as shown in Figure 27. The installation of a turbulator strip ahead of the laminar separation bubble on the suction side of the winglet tripped the laminar boundary-layer to turbulent before a laminar separation bubble could be formed as shown in Figure 28. The effects on the performance of the winglet with turbulators installed were measured during the force and moment balance data acquisition phase of the wind tunnel testing.

FIXED GEOMETRY WINGLET RESULTS

For the fixed geometry winglet and standard wing tip, data is presented for a dynamic pressures of 10.85 lb/ft^2 and 20.8 lb/ft^2 , which corresponds to Reynolds numbers of $6.1 \times 10^5 \text{ ft}^{-1}$ and $8.2 \times 10^5 \text{ ft}^{-1}$ and airspeeds of 65 and 90 miles per hour respectively. In Figures 29 and 30, the lift curves, drag polars, and pitching moment coefficients for the model are presented. The winglet without turbulator strips installed is referred to as the clean winglet whereas the winglet with the turbulators is referred to as the turbulated winglet. Included in the figures is a lift curve type of graph for the winglet. This plot is a measure of the winglet force component directed toward the base of the model. A lift coefficient calculation was made for the winglet by using the winglet surface area for non-dimensionalization. This coefficient will be referred to as the coefficient of side force and will be given the symbol CS. As mentioned above, the winglet force measured by the wind tunnel balance is a vector component of the total force produced by the winglet. Therefore the coefficient of side force is not a true lift coefficient for the winglet. However, the side force coefficient gives a general idea of the behavior of the winglet with changes in the angle of attack of the wing and is useful for comparisons between different winglet configurations.

Winglets tend to increase the lift of the wing for the same angle of attack. In Figure 29, the lift curves for the wing model at a dynamic pressure 10.85 lb/ft^2 are presented. From the lift curves it can be seen that the lift was greater when using the winglets. At an angle of attack of 7.5 degrees, the lift curve slope for all three wing tip configurations was reduced by about 30 percent. As mentioned previously in the flow

visualization section, at an angle of attack of 7.5 degrees, the boundary-layer transition location moves from 50 percent chord to the leading-edge as a result of a leading-edge suction peak. Above this angle of attack, the lift curve is that of an airfoil having turbulent flow on the top surface of the wing. At higher angles of attack, premature separation of the turbulent boundary-layer was apparent near the trailing edge. This separation resulted in a loss of lift and the onset of stall and corresponds to angle of attack where the natural laminar flow airfoil was operating well outside of its design condition⁹.

The shift of the boundary-layer transition point to the leading-edge resulted in the pitching moment coefficient suddenly becoming less negative. Pitching moment was higher in magnitude, i.e. more negative, with winglets than with the standard wing tip. The installation of turbulators on the winglet changed the pitching moment to values between that of the standard wing tip and the clean winglet.

The side force produced by the winglet increased as the angle of attack of the wing was increased, and the winglet began to stall when the angle of attack of the wing was 7.5 degrees. A greater amount of side force was produced with the clean winglet as opposed to the turbulated winglet.

From the drag polar it can be seen that the shift in the boundary-layer transition location to the leading-edge corresponds to an increase in the drag coefficient. The drag polar also indicates that turbulators installed on the winglets further reduces the drag coefficient at C_L values above 0.25.

By increasing the wind tunnel dynamic pressure to a Q of 20.8 lb/ft^2 , which corresponds to a Reynolds number of $8.2 \times 10^5 \text{ ft}^{-1}$, no significant change was noticeable in

the lift, drag, and pitching moment coefficient plots from that of the 10.85 lb/ft² case described above. These plots are presented on Figure 30. The maximum side force coefficient of the winglet was greater but the slope was the same. Results are also presented for the wing with no wing tip installed, since these can serve as a baseline for the future testing. For this configuration, the drag was higher, the lift curve slope was lower, and the pitching moment was less negative than the wing with the standard wing tip.

The parameters used to measure the performance of the wind tunnel model for the different wing tip configurations were the lift to drag ratio and the climb parameter. Since the results presented are for the model and not for a full-scale aircraft, percentage differences in the L/D between the different wing tip configurations cannot be used directly to determine aircraft performance. For example, a 9 percent improvement in the L/D of the model does not mean that a 9 percent improvement will be achieved for a full-scale aircraft. However, extrapolation could be used to estimate performance for a simple wing geometry such as a constant chord wing. For this investigation, only the outboard 20 percent of the semi-span was used; and in order to get an accurate measure of the performance for the entire wing, more information would be needed. Nevertheless, with the force and moment data obtained for the model, general trends as to the effects of different wing tip configurations can be determined.

In Figure 31, the L/D results at a dynamic pressure of 10.85 lb/ft² are presented. The greatest value of L/D was achieved at a C_L of 0.625 using the winglet with the turbulator strip installed, and a nine percent improvement in the maximum L/D over the standard wing tip was measured. An L/D increase of one percent was provided by the

clean winglet at this dynamic pressure. At a dynamic pressure of 20.8 lb/ft², as shown on Figure 32, the L/D increased for the standard wing tip and the winglet from that of the lower Q value. The clean winglet provided the maximum improvement over the standard wing tip although the turbulated winglet provided almost the same benefit. Even though the addition of turbulators on the winglet produces a small amount of extra drag at the higher Reynolds number. Note that at a higher dynamic pressure, the laminar separation bubble on the suction side of the winglet and the laminar separation on the pressure side no longer occurred. The data shows that the clean winglet provides a 9.7 percent improvement while the turbulated winglet provides an improvement of 8.3 percent. When no wing tip was installed, the maximum L/D was 4.2 percent less with the standard wing tip. In all cases, the maximum L/D of the model was achieved at a C_L around 0.625.

The climb parameter, $C_L^{3/2}/C_D$, was used to measure the relative change in the climb rate between the different wing tip configurations. As mentioned above, a direct comparison in percentage differences in the climb parameter cannot be used to determine the effects on full-scale aircraft. General trends can however be made. In Figure 33, the climb parameter is plotted against the lift coefficient for a dynamic pressure of 10.85 lb/ft². The maximum value of climb rate parameter was achieved at a C_L of 0.83. Above a C_L of 1.0, the climb rate parameter suddenly decreased in value. This region corresponded to the boundary-layer transition location moving to the leading-edge of the wing. Overall, for this case, the turbulated winglet provided the maximum gain in the climb parameter with an 11 percent increase over the standard wing tip value. The clean winglet, however, provided a six percent improvement.

At the higher dynamic pressure value of 20.8 lb/ft², as shown on Figure 34, the clean winglet provided the maximum climb parameter. However, the turbulated winglet provided almost the same benefit as the clean winglet at this dynamic pressure. At this Q, the maximum improvement in the climb parameter over that of the standard wing tip was 11.7 percent; and with no wing tip installed, the climb parameter decreased by nine percent from that of the standard wing tip. Above a C_L of 1.0, which corresponds to the boundary-layer transition point on the suction side of the wing moving to the leading-edge, the climb parameter began to drop in value for all wing tip configurations.

One of the problems with winglets is that they tend to increase the wing root bending moment due to the side load produced by the winglet. However, the increase in wing root bending produced by the winglet is much less than that produced by a comparable wing tip extension. The difference in the amount of bending moment between a winglet and a wing tip extension is due to differences in the moment arm and the force location in each situation. For the winglet, the moment arm is based on the height of the winglet whereas the moment arm of a wing tip extension is based on the wing semi-span. For the present tests, the rolling moment measured at the base of the wind tunnel model is a measure of the wing root bending moment for the model. In Figure 35, the rolling moment coefficient at the base of the model is plotted against the lift coefficient of the wing; and the magnitude of the rolling moment increases linearly with increased value of lift coefficient. At a C_L of 0.8, the rolling moment at the base of the model was increased by 4.6 percent over that of the standard wing tip. Surprisingly as shown on Figure 36, when the dynamic pressure was increased to 20.8 lb/ft², the rolling moment coefficient

variation with lift coefficient was identical to that of the 10.8 lb/ft² case. For the wing model without a wing tip installed, the rolling moment was at the minimum.

ARTICULATING WINGLET RESULTS

All balance data obtained for the articulating winglet was taken at a dynamic pressure of 8 lb/ft² due to the structural limitations of the winglet articulating mechanism. Performance comparisons were conducted for differing cant, toe, and winglet rudder angles. The wind tunnel model without a wing tip installed was used as a baseline for comparing the results of the fixed geometry winglet and the articulating winglet. Unfortunately, there was a large discrepancy in the lift and drag coefficient between the two wind tunnel tests with the same model configuration with no wing tip. In Figure 37, the lift curves and drag polars are presented for the baseline case of the first and second wind tunnel test. Discrepancies in the lift curve can be attributed to the angle of attack measurement of the model. By subtracting one degree from the lift curve data of the second wind tunnel test, the lift curves from the first and second test line up below a lift coefficient of 1.0. The discrepancies in the drag polars can be attributed to the difference in the dynamic pressure between the two tests. The first test baseline was run at a dynamic pressure of 20.85 lb/ft² and the second test was run at a dynamic pressure of 8 lb/ft². Higher drag coefficients in the second wind tunnel test are related to the lower Reynolds number.

The effects of cant angle on the drag polar, lift curve, side force curve, and pitching moment coefficient are shown in Figure 38. Above a C_L of 0.5, a cant angle of 65 degrees produced less drag than the 85 degree case. When the lift coefficient was below 0.25, the minimum drag was produced with a cant angle of 85 degrees. Between a C_L of 0.25 and 0.5, the drag coefficients with a cant angle of 85 degrees and 65 degrees were nearly the

same. However, the 50 degree cant angle produced more drag than the other two cases below a C_L of 1.0. Above a C_L of 1.0, the 50 degree cant angle case produced the same drag as the 65 degree case.

There were no significant differences in the lift curves between the different cant angles until the higher C_L values were reached, but near stall, the 50 degree cant angle produced more lift than the 85 degree case. Maximum side force was produced at a cant angle of 85 degrees, and the minimum amount of side force was produced by the 50 degree cant angle.

Cant angle also had an effect on pitching moment at C_L values above 1.0. As with the fixed geometry winglet test, the boundary-layer transition point moved to the leading-edge at an angle of attack of 7.5 degrees and a lift coefficient of around 1.0. Consequently, above an angle of attack of 7.5 degrees, the pitching moment was lower in magnitude with the 85 degree cant angle and higher in magnitude with the 50 degree cant angle. Below this angle of attack, the pitching moment was nearly identical for all three cant angles tested.

In Figure 39, the effects of toe-out angle on the drag polar, lift curve, side force, and pitching moment are presented for a cant angle of 85 degrees. Minimum drag was produced with a toe-out angle of 2.5 degrees. This value corresponds to the neutral toe angle position of the articulating winglet. The next lowest value of drag was produced with a toe-out angle of 5 degrees followed by 0 degree case. The 22.5 degree toe-out angle produced the highest amount of drag at the lower C_L values. However, at C_L values above 0.5, the 22.5 degree toe-out angle case yielded drags in the same range as the other toe-out

angles. On the lift curves, toe-out angles between 0 and 12.5 degrees had no significant effect; but for a toe-out angle of 22.5 degrees, the lift curve, while having the same slope as the other cases, had higher C_L values at corresponding angles of attack.

Opposite to that of varying the cant angle, the results indicate that the toe-out angle had an effect on pitching moment below an angle of attack of 7.5 degrees and little effect above 7.5 degrees. The pitching moment was the lower in magnitude with a toe-out angle of 0 degrees and higher in magnitude at a toe-out angle of 22.5 degrees. The other toe-out angles of 2.5, 5, and 12.5 degrees were all in order between the 0 degree and 22.5 degree case.

As expected, side force increased as the toe-out angle was increased, and the maximum side force was produced when the toe-out angle was 22.5 degrees. Interestingly, for each side force curve, the maximum side force was produced at an angle of attack of 7.5 degrees, which again, corresponded to the region where the boundary-layer transition point moved to the leading-edge as was exhibited in the fixed geometry winglet results.

The effects of changing the camber of the winglet by deflecting a rudder on the winglet was investigated for cant angles of 65 degrees and 85 degrees and a toe-out angle of 2.5 degrees. For the 65 degree cant angle case, which is given in Figure 40, minimum drag was produced when the rudder was in the neutral position. Maximum drag for a given C_L was produced when the rudder was reflexed to an angle of -10 degrees as portrayed on Figure 41. At a cant angle of 85 degrees, minimum drag was produced when the rudder angle was in neutral or in the reflexed position of -10 degrees and maximum when the rudder angle was +10 degrees.

When the cant angle was 65 degrees, the deflection of the winglet rudder in a positive direction increased the lift of the wing, and deflecting the rudder in a negative direction decreased the lift of the wing. The 85 degree cant angle case had similar results but not nearly as pronounced as with the 65 degree cant angle. No rudder deflection data were taken with the 50 degree cant angle case due to a structural problem with the articulating mechanism. In both cant angle cases, side force increased with positive rudder deflection and decreased with negative rudder deflection.

At the 65 degree cant angle, pitching moment was a lower magnitude with a rudder deflection of -10 degrees and higher magnitude with a rudder deflection of +10 degrees. However, when the cant angle was 85 degrees, the rudder had very little effect on the pitching moment.

As mentioned in the results of the fixed geometry winglet, the percentage differences in the performance parameters, L/D and $C_L^{3/2}/C_D$, between different wing tip configurations are for the model and not for a full-scale sailplane. Therefor, the results of the articulating winglet have been examined for general trends of the effects of changing cant, toe, and winglet rudder angles.

In Figure 42, the lift to drag ratio is plotted against the lift coefficient for winglet cant angles of 50, 65, and 85 degrees. The data shows that a maximum lift to drag ratio for all values of lift coefficient was achieved using a cant angle of 65 degrees. Note that the baseline case using the wing with no wing tip installed was included in all the graphs for comparison purposes.

The effects of winglet toe-out angle on the lift to drag ratio for a cant angle of 85 degrees is shown in Figure 43. Here, the maximum lift to drag ratio was achieved when the toe-out angle was in the neutral position of 2.5 degrees, and the next highest L/D was obtained using a toe-out angle of 5 degrees followed by 0 degrees. A toe-out angle of 12.5 degrees provided the minimum L/D for the cant angles presented.

As shown on Figure 43, at a cant angle of 65 degrees and a toe-out angle of 2.5 degrees, the deflection of the winglet rudder either positive or negative reduced the maximum L/D. The lowest L/D for the winglet was obtained when the winglet rudder was reflexed to an angle of -10 degrees. However, as displayed on Figure 45, when the cant angle was moved to 85 degrees, the maximum L/D was equal for both the -10 and 0 degree winglet rudder deflections. Originally this behavior was thought to be a data error because the L/D curves were close to being the same for the two cases. However, in Figure 41 it can be seen that the side force produced by the winglet with the rudder reflexed to -10 degrees was lower than that produced when the rudder was in the neutral position of 0 degrees. For the 85 degree cant angle case, the rudder deflections had no significant effect on the L/D above a C_L of 0.825.

A comparison of the climb parameter at the different winglet cant angles, as plotted in Figure 46, reveals that a cant angle of 65 degrees produced the maximum climb parameter. Below a C_L of 0.55, the climb parameter for the 85 degree cant angle was equal to that of the 65 degree case, and above a C_L of 0.825, the 50 degree cant angle climb parameter was equal to the 65 degree case. At a C_L of 0.9, which corresponds to the large shift in boundary-layer transition point, the climb parameters for the three different

cant angles were nearly equal.

The effect of the winglet toe-out angle on the climb parameter for a cant angle of 85 degrees is shown in Figure 47. The results show that a maximum value of climb parameter was obtained when the toe-out angle was in its neutral position of 2.5 degrees, and the next highest values of climb parameter were obtained by a toe-out angle of 5 degrees followed by the 0 degree case. A toe-out angle of 12.5 degrees had the minimum value of climb parameter for the winglet toe-out angles presented.

The effects of winglet rudder deflection on the climb parameter for a cant angle of 65 degrees and a toe-out angle of 2.5 degrees are presented in Figure 48. The maximum value of the climb parameter was produced with a winglet rudder in the neutral position of 0 degrees. When the winglet rudder was reflexed to an angle of -10 degrees, the climb parameter was at the minimum value. Similar to the L/D case, when the cant angle was 85 degrees, the maximum values of climb parameter were equal for the winglet rudder positions of 0 and -10 degrees as shown in Figure 49. The lowest value of climb parameter was obtained when the winglet rudder was at an angle of +10 degrees.

The effects of winglet cant angle on the wing rolling moment for the model are presented in Figure 50. Very small differences in the rolling moment between the different cant angles were observed. Higher rolling moments were produced with a cant angle of 50 degrees produced at higher values of C_L , and at low values of C_L , the rolling moment was the greatest when the cant angle was 85 degrees. As portrayed on Figure 51, winglet toe-out angle appeared to have little effect on the rolling moment of the model, but at the extreme toe-out angle of 22.5 degrees the rolling moment was increased slightly. For both

a 65 degree and 85 degree cant angle, the winglet rudder provided an increased rolling moment when deflected in a positive direction, this phenomena can be observed on Figures 52-53. The rolling moment for the 0 degree and -10 degree rudder angle cases were identical for a cant angle of 85 degrees.

The yawing moment of the model indicates which winglet configuration produced the minimum amount of drag since this moment, measured at the base of the model, can be resolved into a vector component of the total drag and the moment arm for which the force vector of the drag acts. In Figure 54, the yawing moment versus C_L plots for the cant angles of 50, 65, and 85 degrees at a toe-out angle of 2.5 degrees are presented. From this graph it can be seen that the 65 degree cant angle produced the minimum amount of yawing moment while the greatest amount of yawing moment was produced when the cant angle was 50 degrees. A toe-out angle of 2.5 degrees produced the minimum amount of yawing moment at a cant angle of 85 degrees among the various toe-out angles presented as shown in Figure 55.

The effect of the winglet rudder on the yawing moment was studied to determine whether yaw control could be achieved or supplemented. In Figures 56 and 57, the effect on yawing moment by deflecting a winglet rudder is shown for a cant angle of 65 and 85 degrees, respectively. By deflecting the rudder +10 degrees, the yawing moment was increased in both cases which indicated an increase in the drag produced by the winglet. The winglet rudder was more effective for increasing the yawing moment as compared to changing cant angle or toe-out angle. Using the data given in Figure 57, the increase in yawing moment at the base of the model would amount for 4.7 ft*lbs when the winglet

rudder is deflected +10 degrees at a Q of 8 lb/ft^2 and a C_L of 0.55. If it is assumed that the extra drag was produced entirely by the winglet and was located at the tip of the model, the additional amount of moment at the aircraft centerline would be approximately 20.8 ft*lbs . The moment arm of the vertical tail from the aerodynamic center of a sailplane is typically about twelve feet. For the vertical tail to create this moment, a side force of 1.75 lbs would have to be created. Considering the small amount of side force required by the vertical tail to produce the same amount of yawing moment as obtained by deflecting the winglet rudder, and the increased drag associated with this deflection, the winglet rudder does not appear to be an effective way of providing yaw control.

SUMMARY AND CONCLUSIONS

The general behavior and effects of winglets on high performance sailplane wings has been presented. Low Reynolds number effects such as laminar separation bubbles and laminar separation can reduce wing performance at low airspeeds. It was shown experimentally that by tripping the laminar boundary-layer on the winglet ahead of laminar separation, the L/D and climb performance parameters were improved at low airspeeds. With increased Reynolds number, the addition of a boundary-layer trip device reduced the performance from that of the clean winglet but still provided an improved performance over the standard wing tip. A wing without a contoured wing tip of any type provided the lowest performance.

By having the capability of adjusting the cant, toe, and winglet rudder angles, it was hoped that performance could have been increased over a wide range of wing lift coefficients. Even though this goal was not realized, valuable information was gathered as to the behavior of winglets with different winglet cant and toe-out angles. Surprisingly, only one optimum combination of toe-out and cant angles was obtained.

As expected the installation of winglets increased the lift coefficient of the wing for the same angle of attack. As the cant angle measured from the vertical axis was increased, the lift coefficient of the wing increased as a result of the vertical lift component of the winglet. This increased lift of the wing was accompanied by an increase in the rolling moment at the base of the model, as expected. However, even though the winglets increased the wing root bending moment, it was only by a small amount compared to the increased wing performance resulted from the installation of winglets. If a wing tip

extension which provides the same improvement obtained with the winglet were installed, a greater wing root bending moment would be produced due to the increased wing span.

By increasing the camber of the winglet with the deflection of a rudder, it was originally expected that the lift of the wing would increase, thus improving the climb parameter. Although the lift of the wing as well as the side force did increase, a subsequent increase in the amount of drag did not yield an increase in the climb parameter. Because of this increased drag, deflecting a rudder on the winglet had more of an effect on increasing the yawing moment than changing either the cant or toe-out angles. Although the winglet rudder was more effective, the additional drag and the amount of yawing moment produced, when compared with that of the vertical tail, does not justify its use. The deflection of the winglet rudder, either positive or negative, only served to decreased the wing performance in most cases.

The fixed geometry winglet tested in the first series of wind tunnel tests provided the maximum gain in the lift to drag ratio and the climb parameter compared to the standard wing tip and the articulating winglet. By adjusting the cant, toe, and rudder angles of the articulating winglet, a performance gain over a wider range of lift coefficients was not realized. Optimum performance of the articulating winglet was provided with a cant angle of 25 degrees from the vertical axis and a toe-out angle of 2.5 degrees. It was therefore concluded that maximum wing performance can be gained by the proper design of a fixed geometry winglet. The winglet rudder also proved not to be useful in providing increased wing performance or yawing moment.

REFERENCES

1. Nicks, O. W. , Landrum, D. B., "Wing Extensions for Improving Climb Performance," AIAA Paper 83-2556, Oct. 1983.
2. Van Dam, C. P., "Natural Laminar Flow Airfoil Design Considerations for Winglets on Low-Speed Airplanes," NASA Contractor Report 3853, Dec. 1984.
3. Masak, P. C., "Design of Winglets for Sailplanes," *Soaring Magazine*, Soaring Society of America, Inc., Hobbs, New Mexico, June 1993, pp. 21-27.
4. Nicks, O. W., "Experimental Comparison of Two Wing Tips," *Technical Soaring*, Soaring Society of America, Inc., Hobbs, New Mexico, Vol. 14, Number 3, 1989, pp. 81-88.
5. Nicks, O. W., "A Physical View of Wing Aerodynamics," *Technical Soaring*, Soaring Society of America, Inc., Hobbs, New Mexico, Vol. 17, Number 4, 1993, pp. 122-128.
6. Rae, X. H., Pope, A., *Low-Speed Wind Tunnel Testing*, John Wiley & Sons, 1984.
7. Schlichting, H., "Origin of Turbulence," *Boundary-Layer Theory*, 7th ed., McGraw-Hill Book Company, New York, 1979, pp. 453-456.
8. Schubauer, G. B., Klebanoff, P. S., "Contributions on the Mechanics of Boundary-Layer Transition," NACA TN 3489, 1955.
9. Vijgen, P. M. H. W., van Dam, C. P., Holmes, B. J., "Sheared Wing-Tip Aerodynamics: Wind Tunnel and Computational Investigations of Induced-Drag Reduction," AIAA Paper 87-2481 CP, Aug. 1987.



Figure 1. Winglets Mounted on a High Performance Sailplane

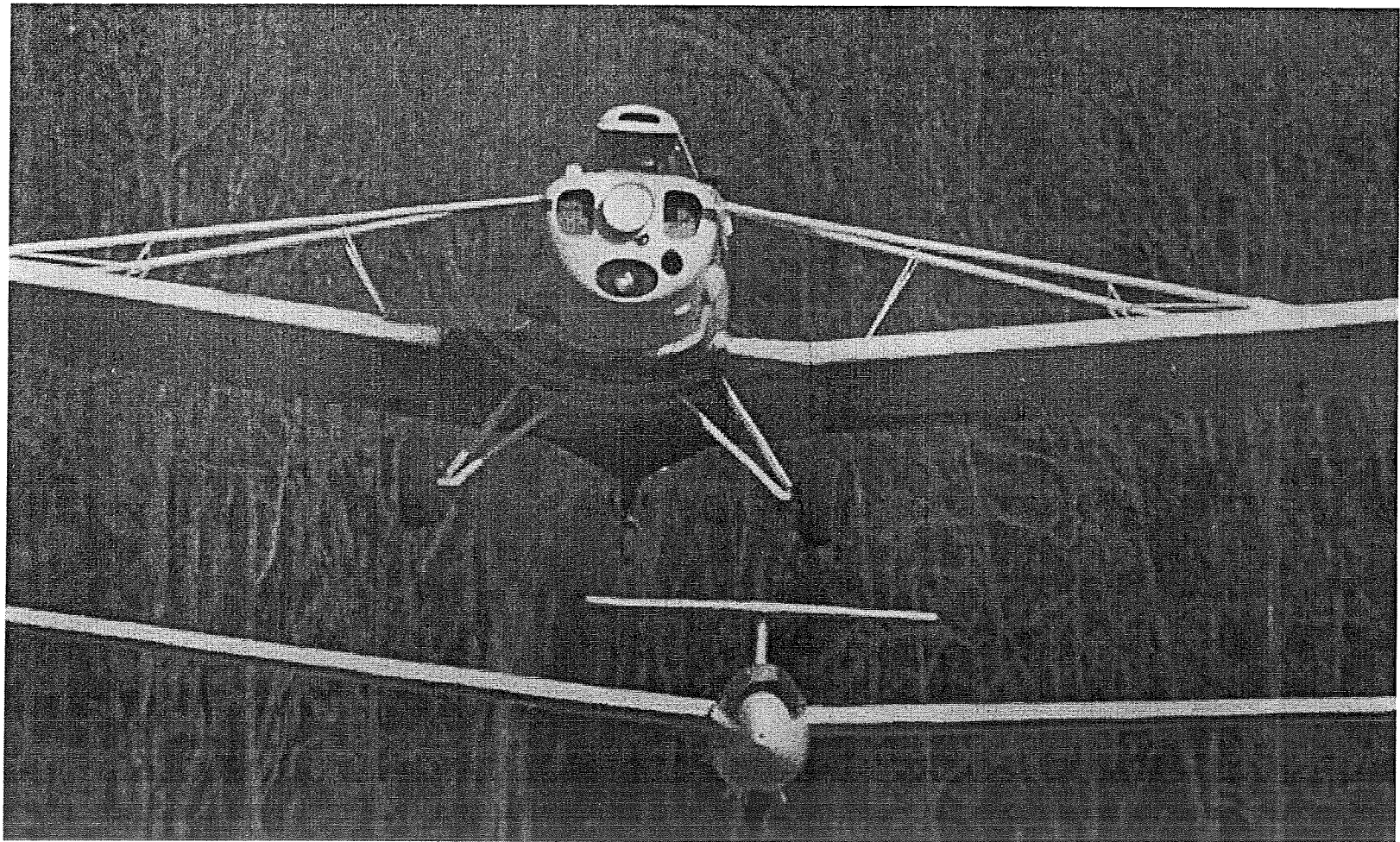


Figure 2. High Performance Sailplane Being Towed by a Powered Aircraft.

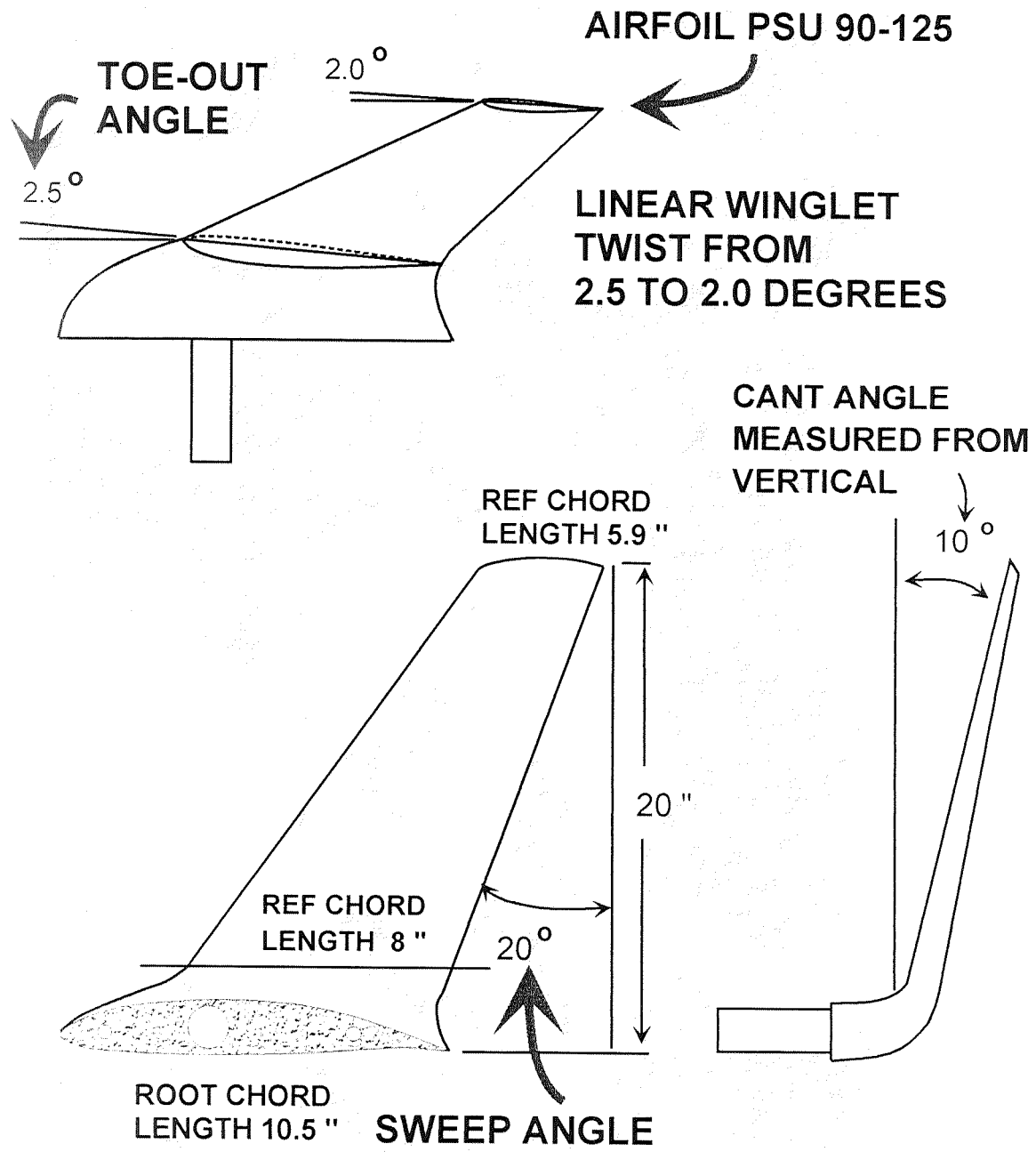


Figure 3. Geometry and Dimensions of Fixed Geometry Winglet.

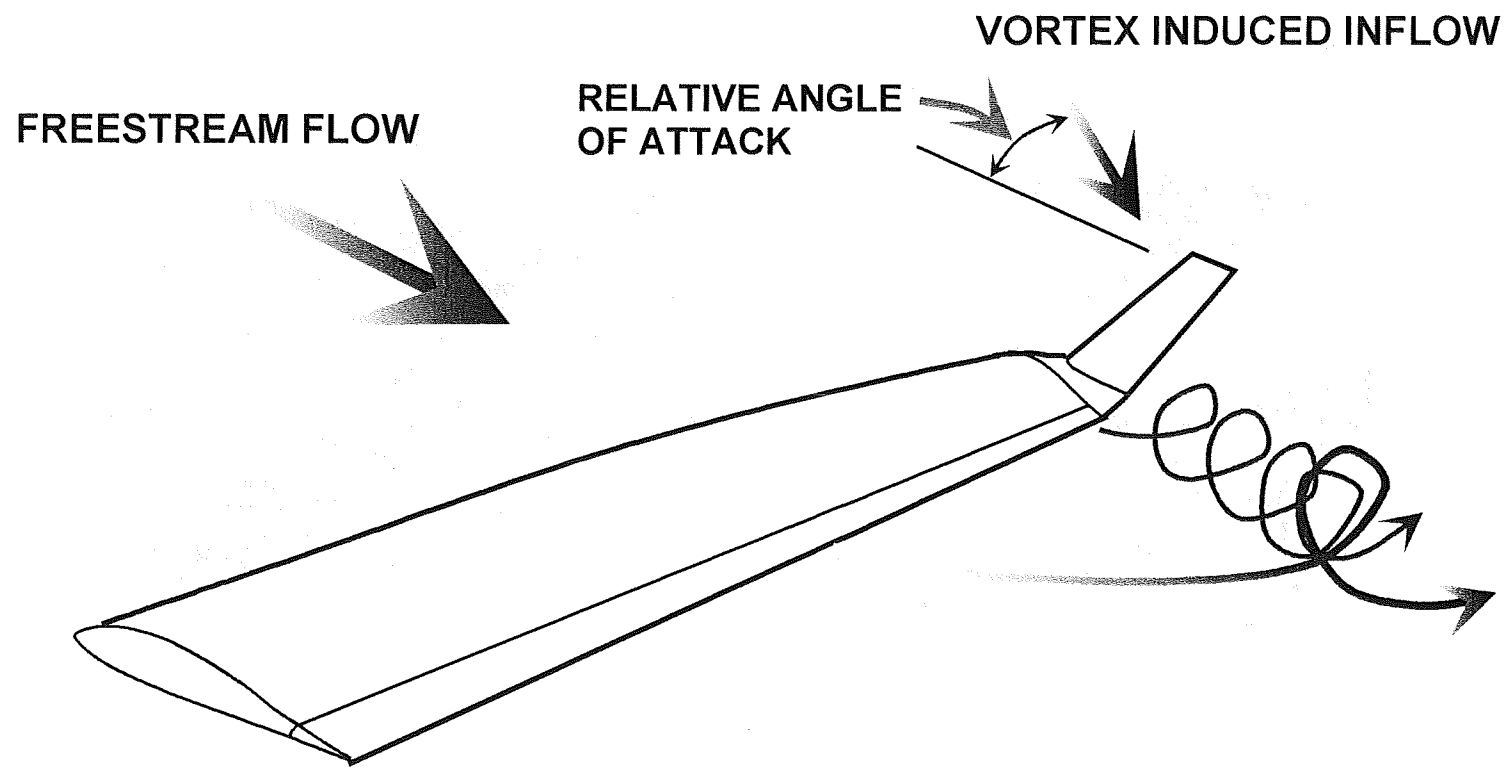


Figure 4. Winglet Relative Angle of Attack.

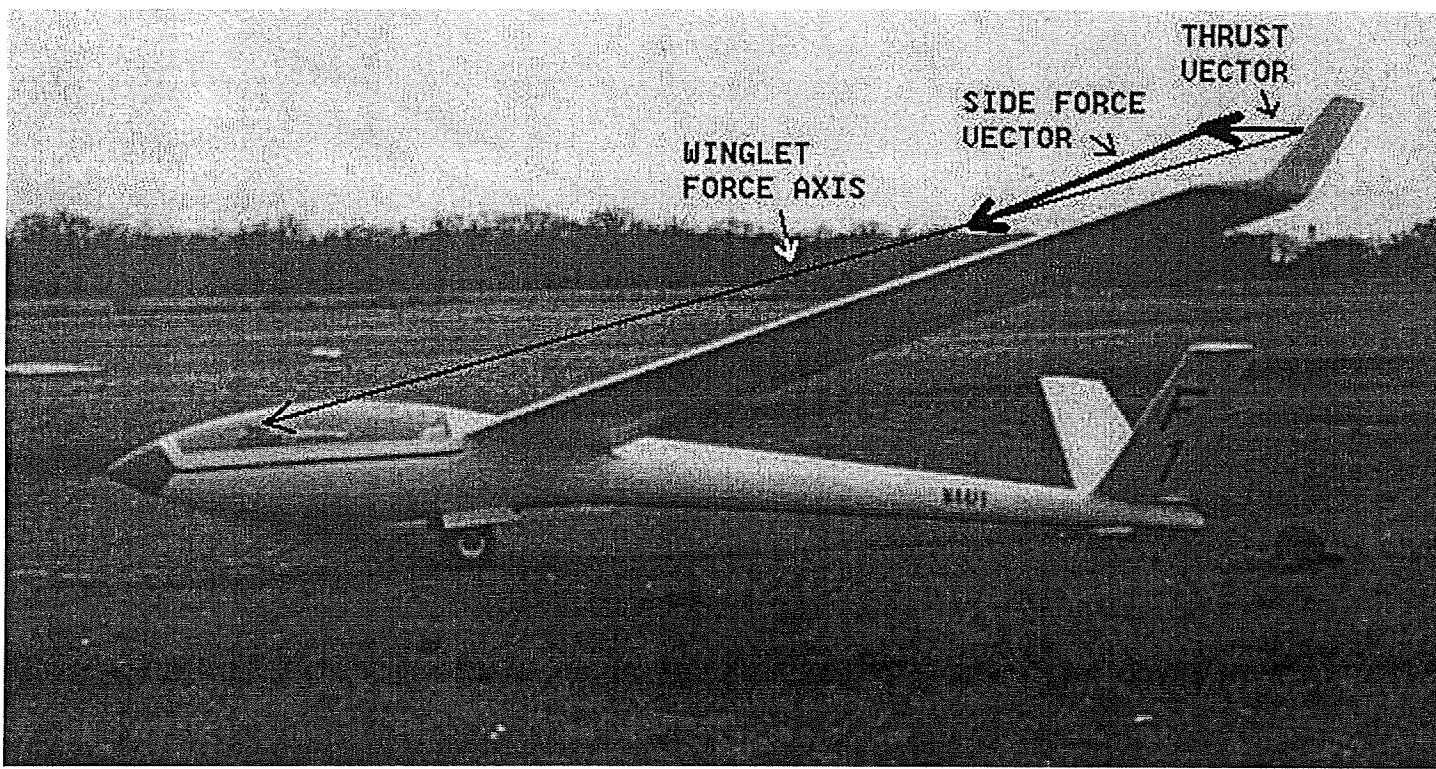


Figure 5. Thrust and Side Component of Winglet Force Vector.

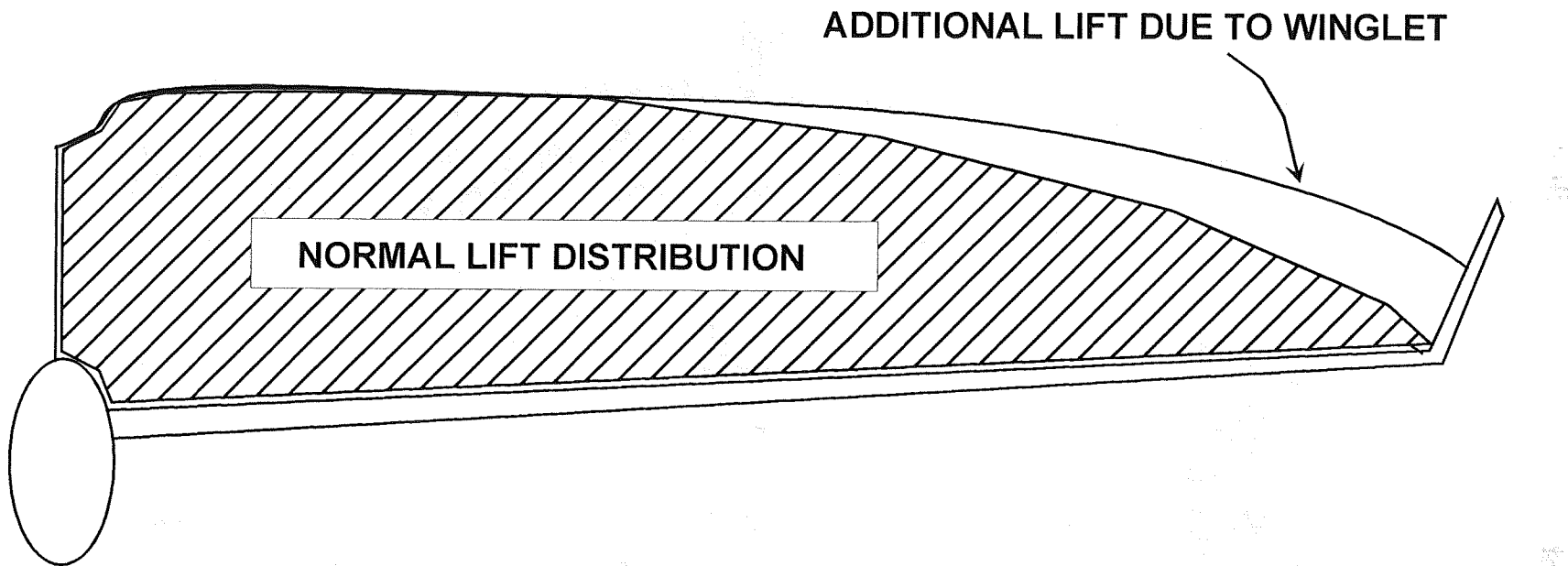


Figure 6. The Effect of Winglets on the Wing Lift Distribution.

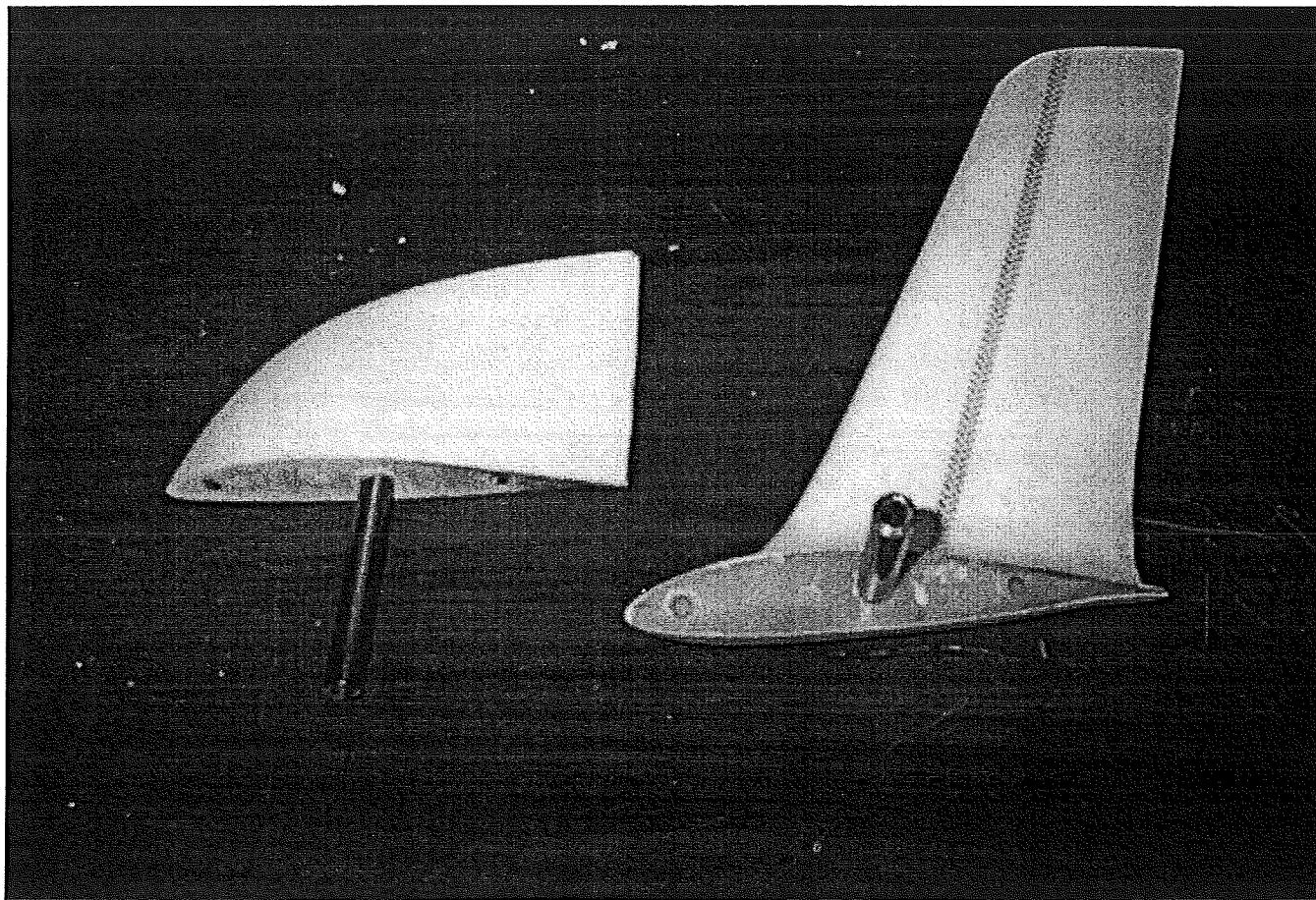


Figure 7. Fixed Geometry Winglet and Standard Wing Tip Used During First Wind-Tunnel Test.

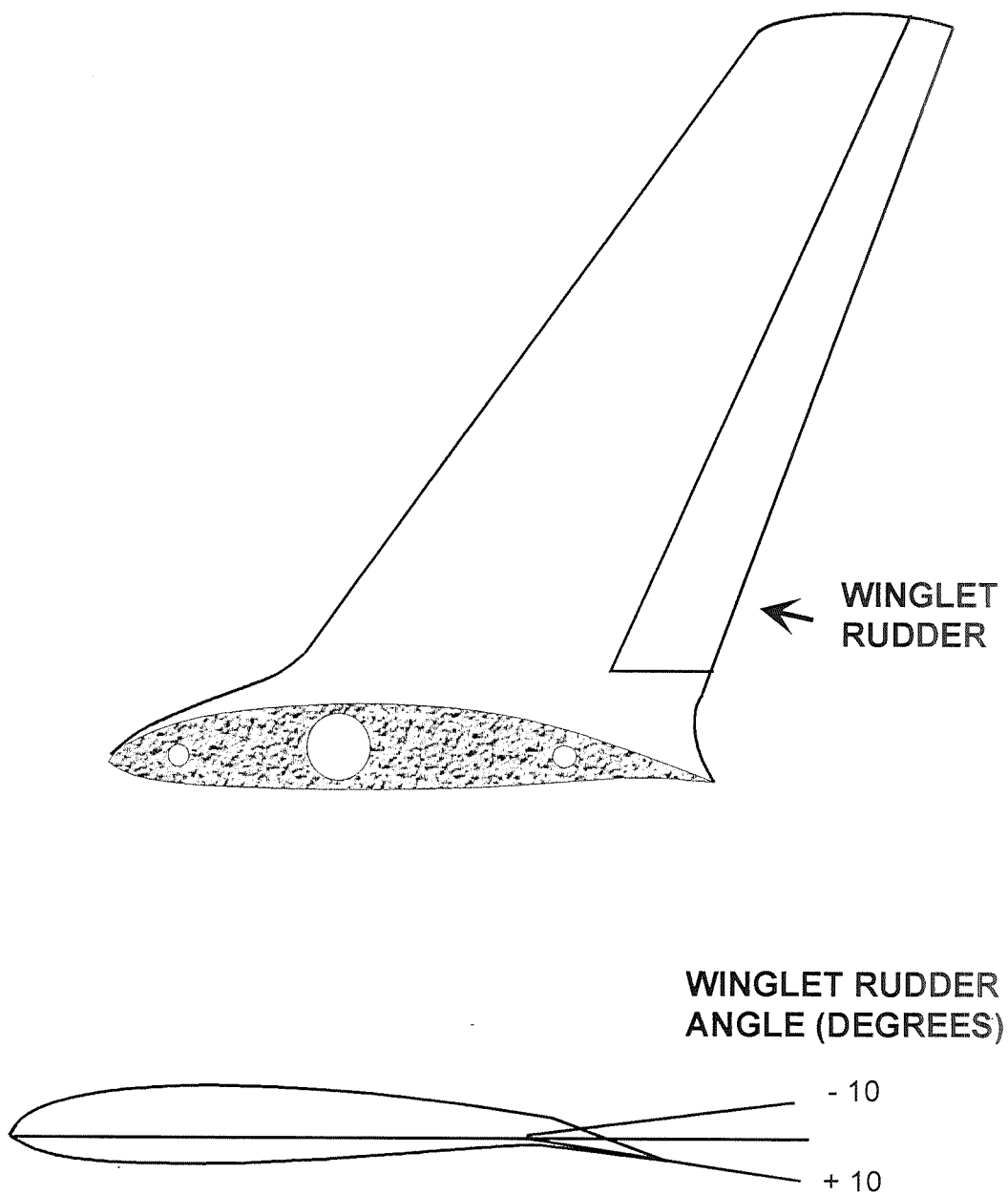


Figure 8. Winglet Rudder Angle.

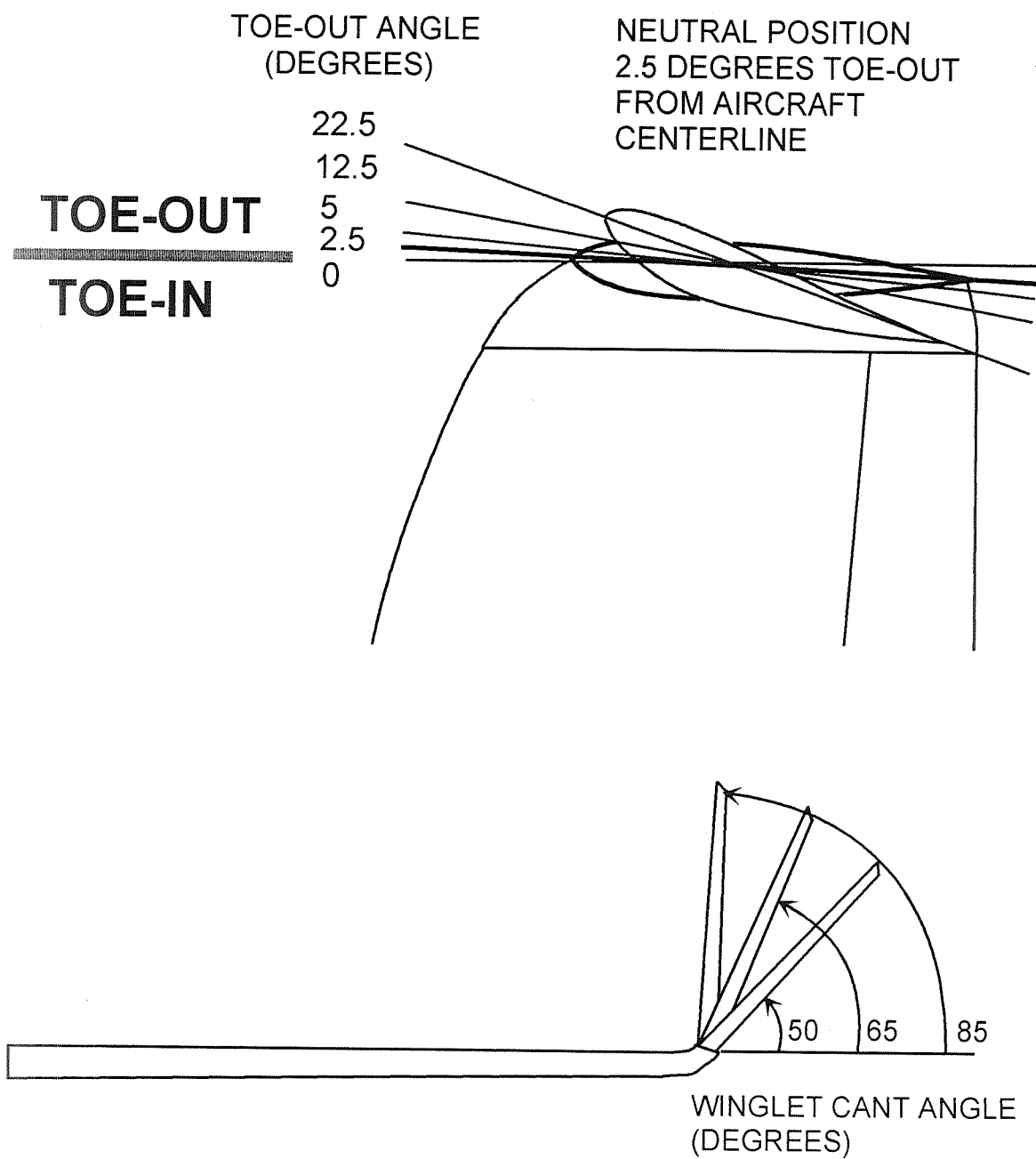


Figure 9. Definition of Toe and Cant Angles Presented in Results.

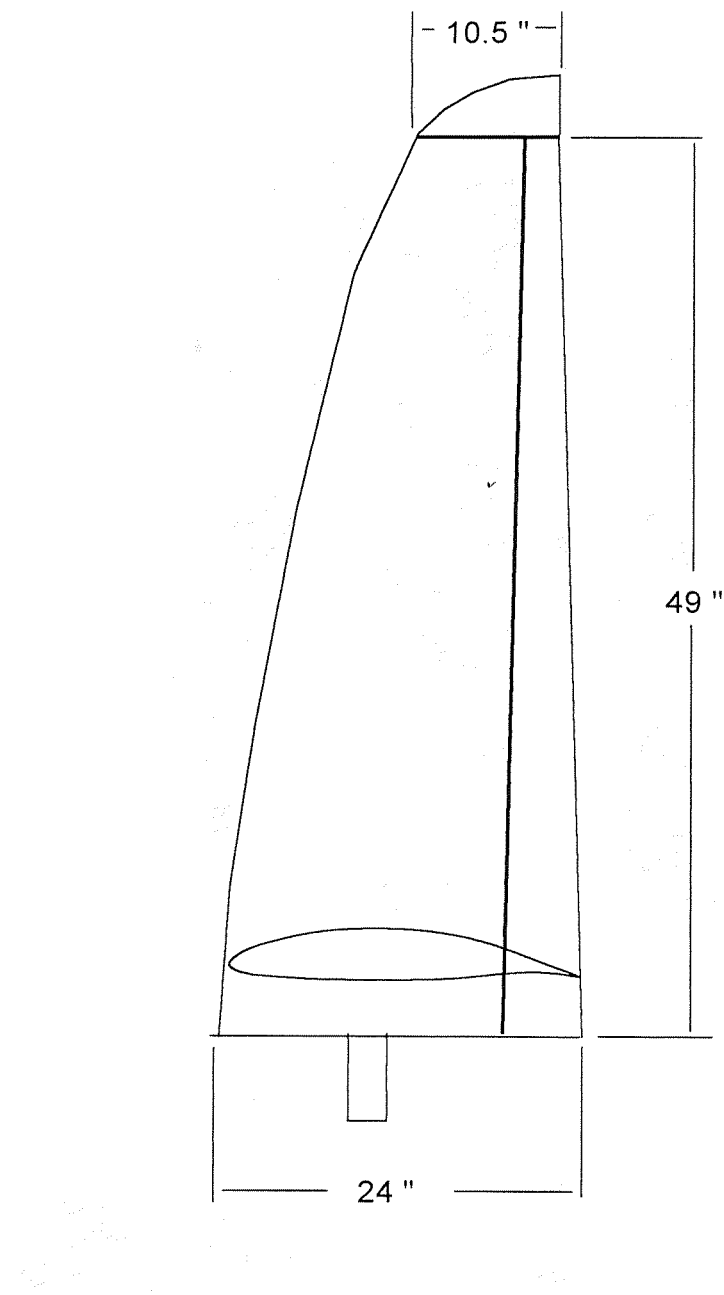


Figure 10: Wind-Tunnel Model Dimensions.

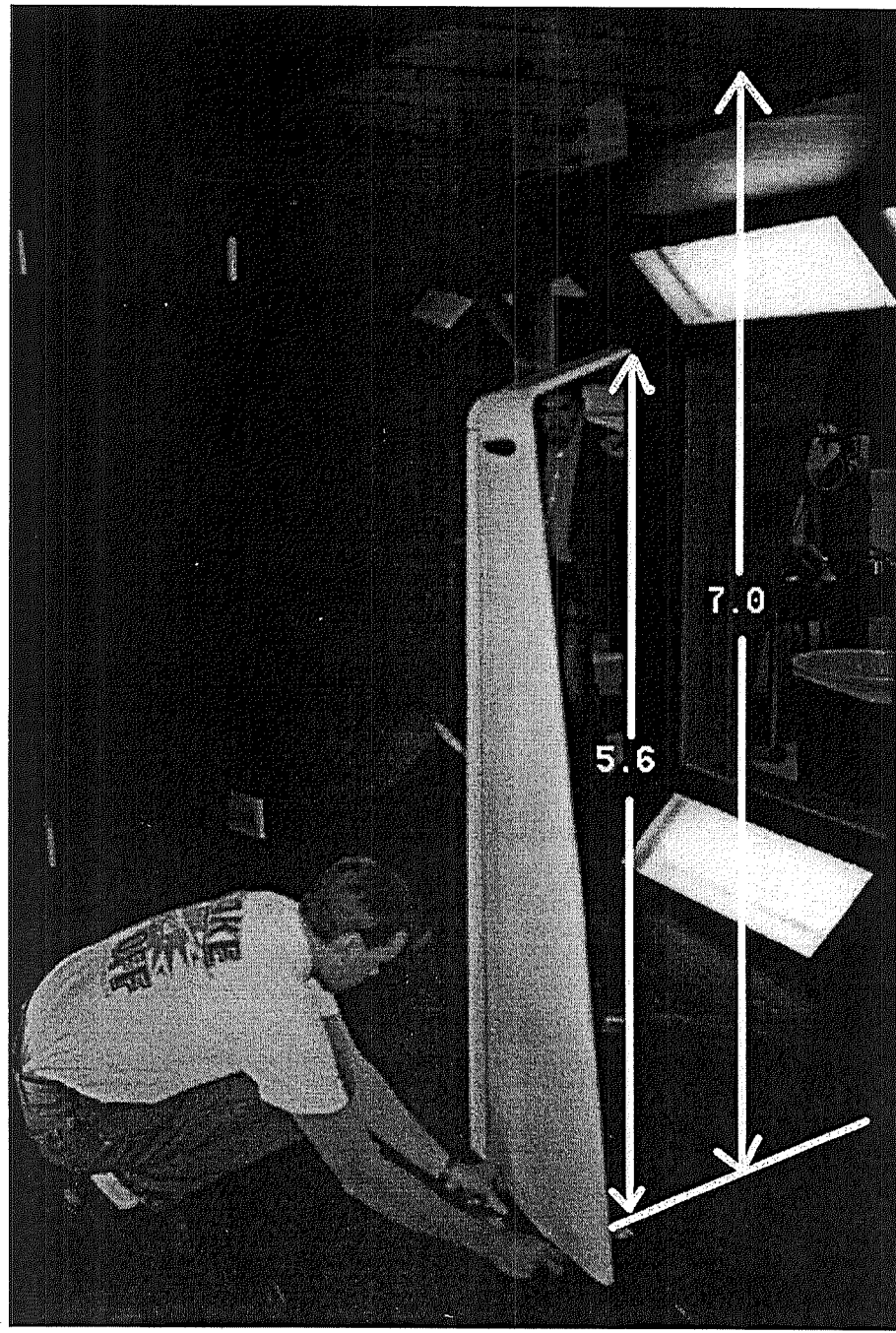


Figure 11. Wing Model Installation and Wall Clearance.

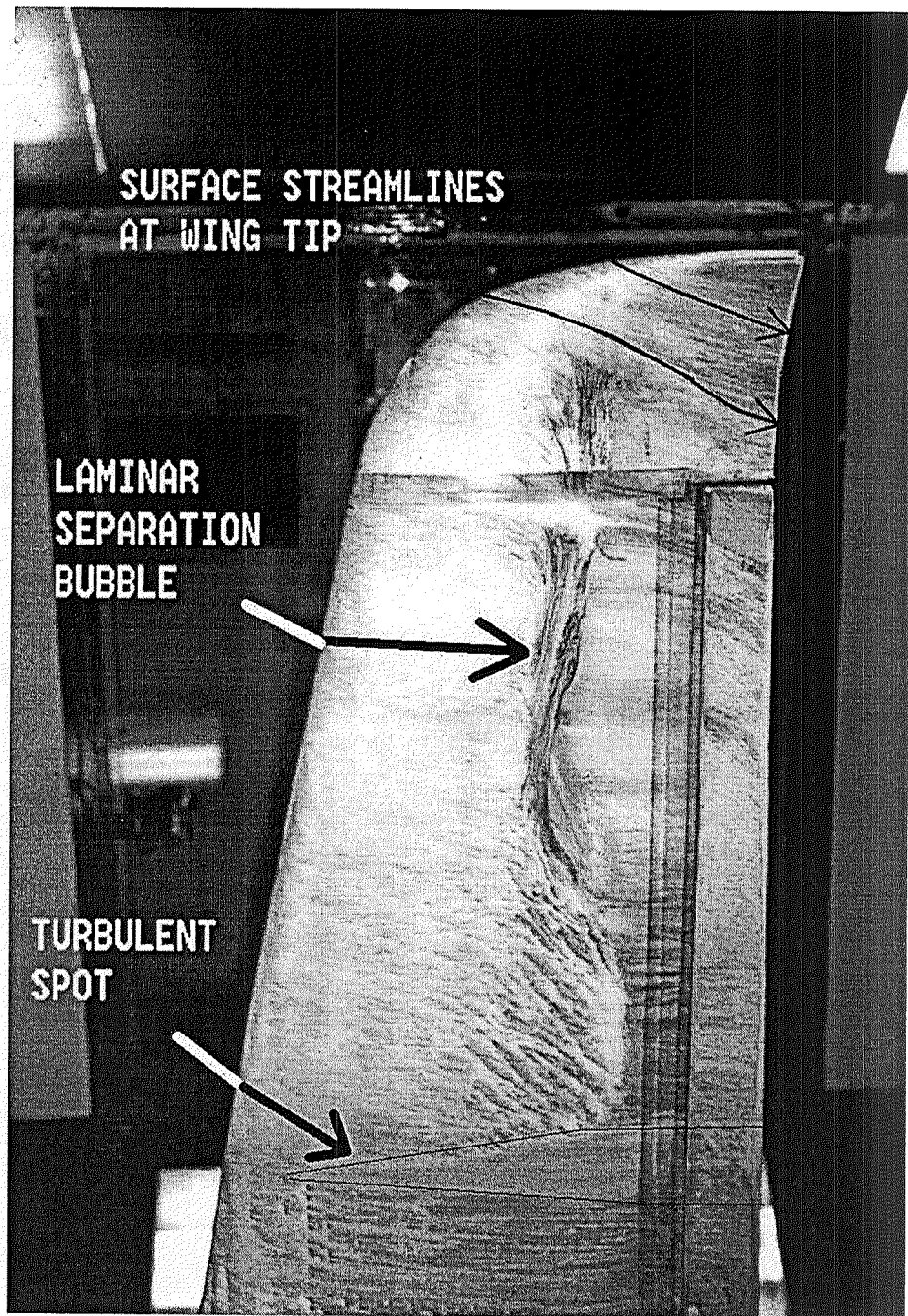


Figure 12. Flow Visualization of Standard Wing Tip Suction Side.
 $\alpha = 2.5^\circ$, $Q = 10.85 \text{ lb/ft}^2$

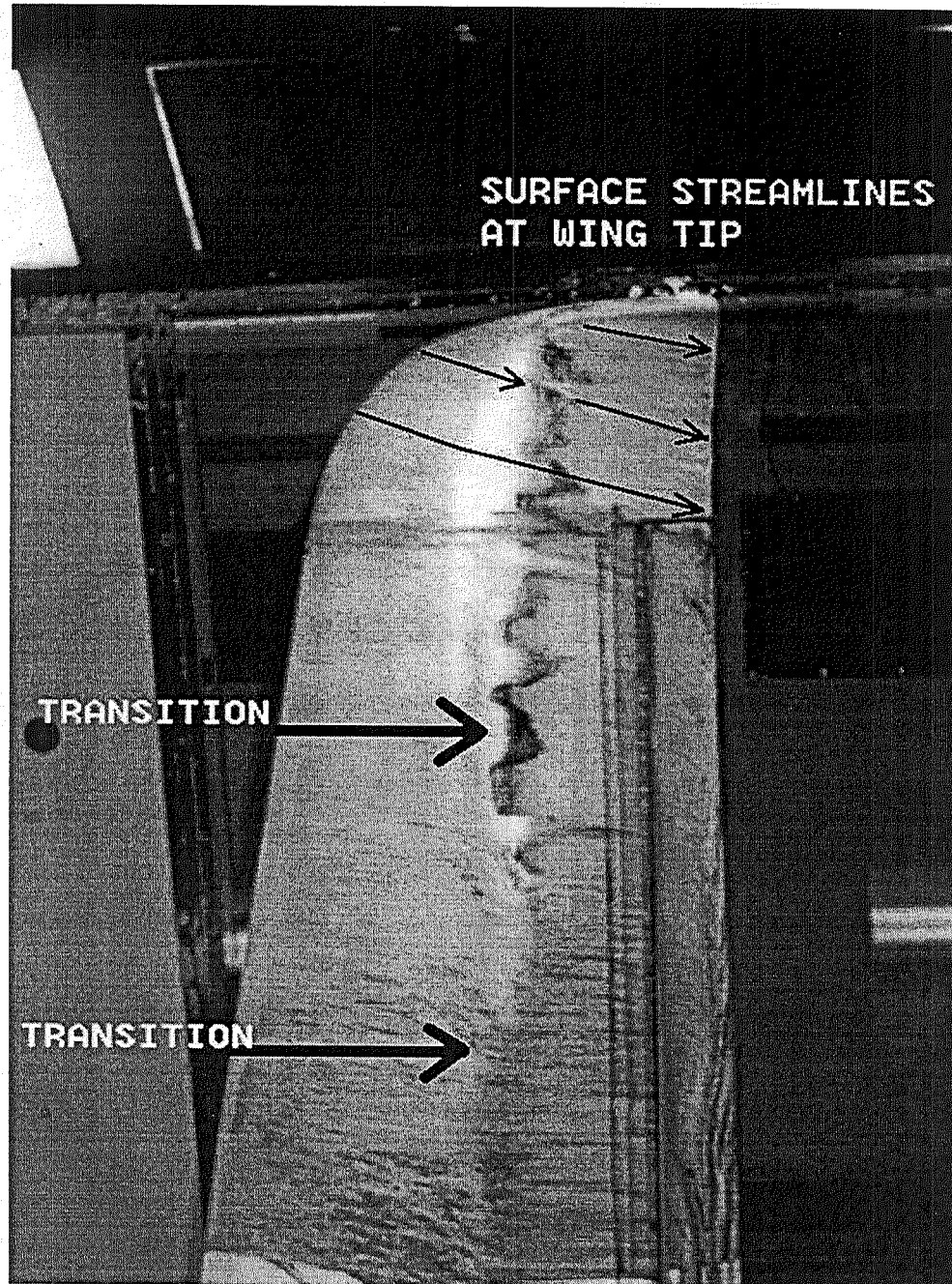


Figure 13. Flow Visualization of Standard Wing Tip Suction Side.
 $\alpha = 5.0^\circ$, $Q = 10.85 \text{ lb}/\text{ft}^2$

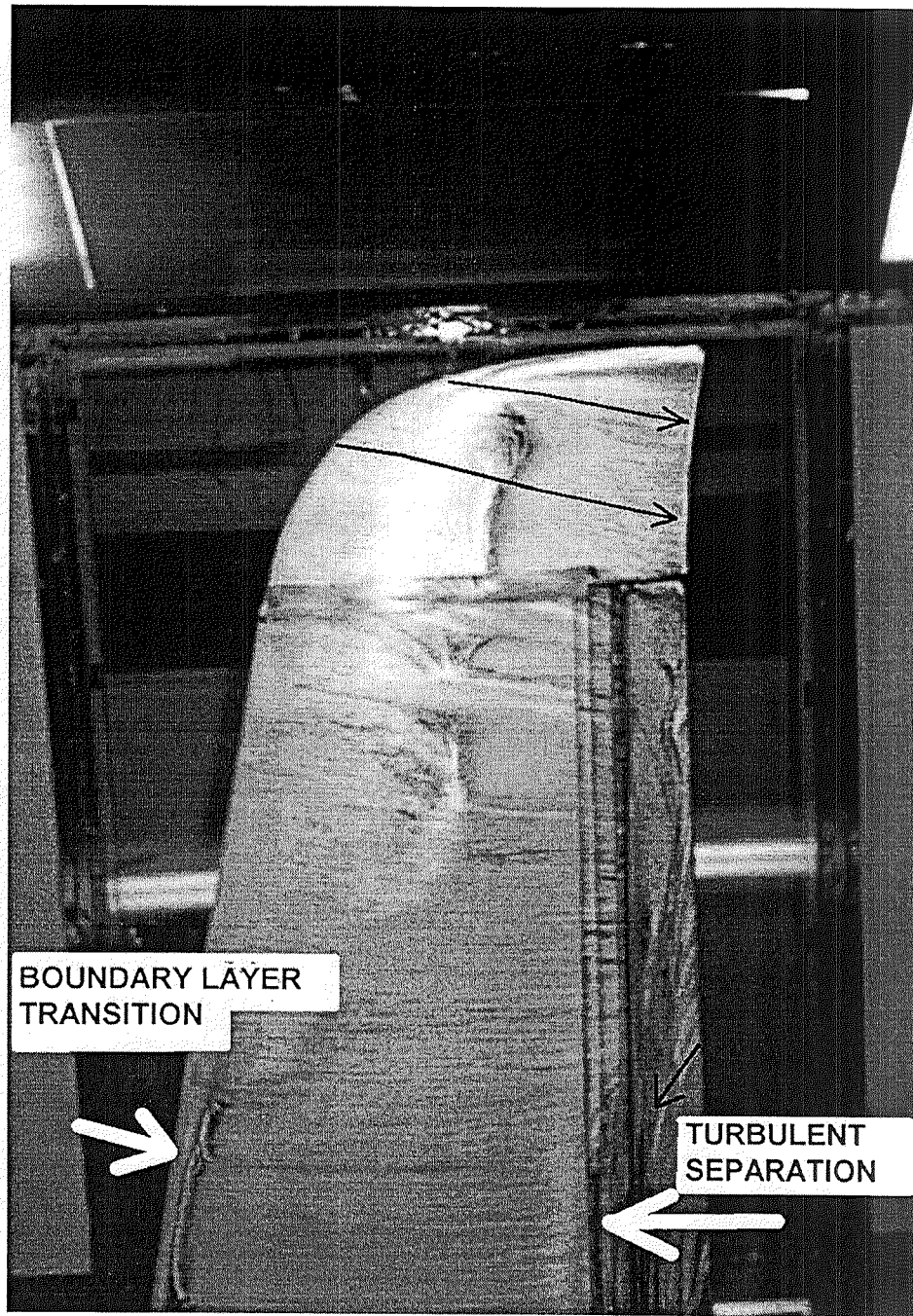


Figure 14. Flow Visualization of Standard Wing Tip Suction Side.
 $\alpha = 7.5^\circ$, $Q = 10.85 \text{ lb/ft}^2$

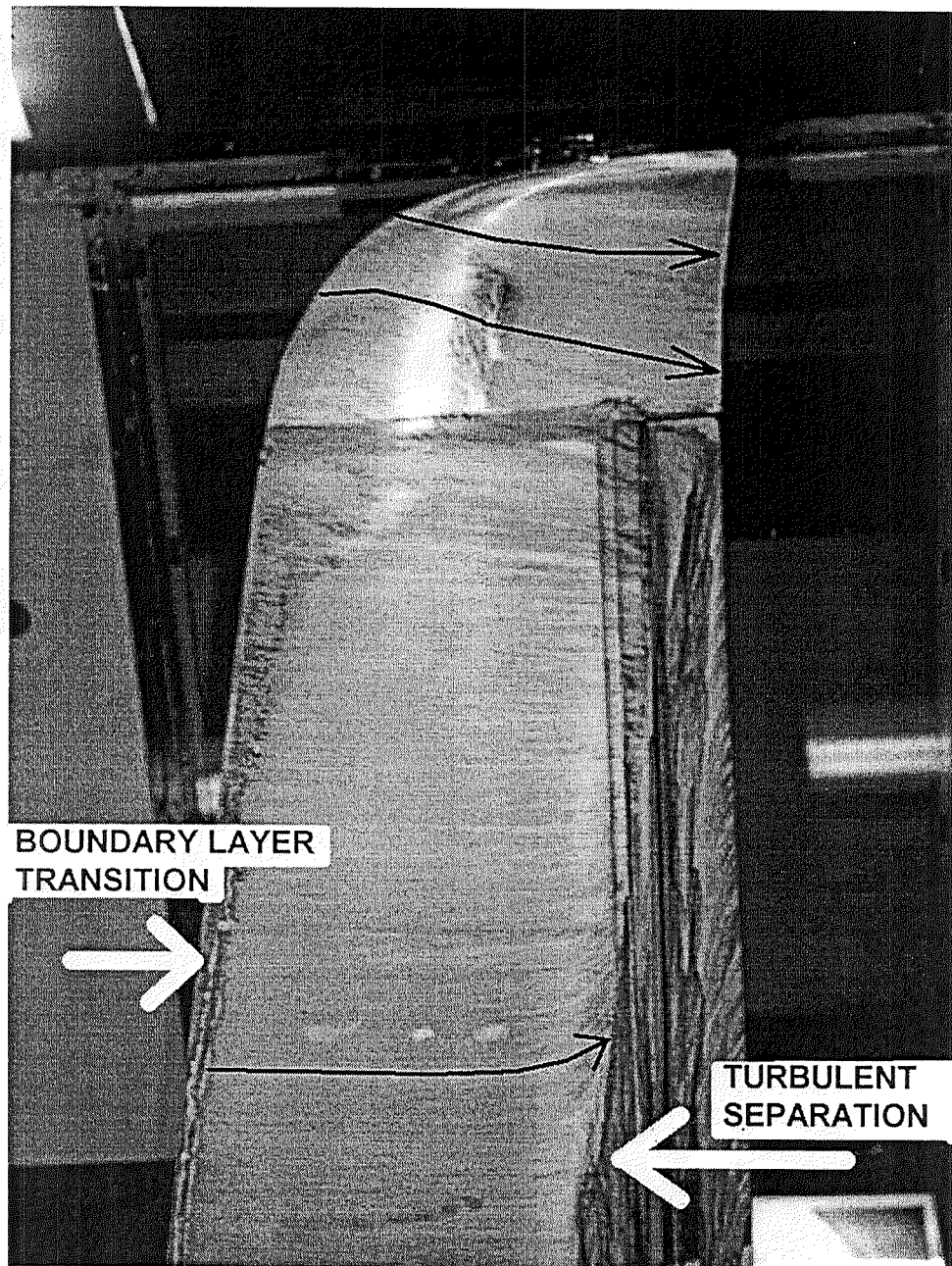


Figure 15. Flow Visualization of Standard Wing Tip Suction Side.
 $\alpha = 10.0^\circ$, $Q = 10.85 \text{ lb/ft}^2$

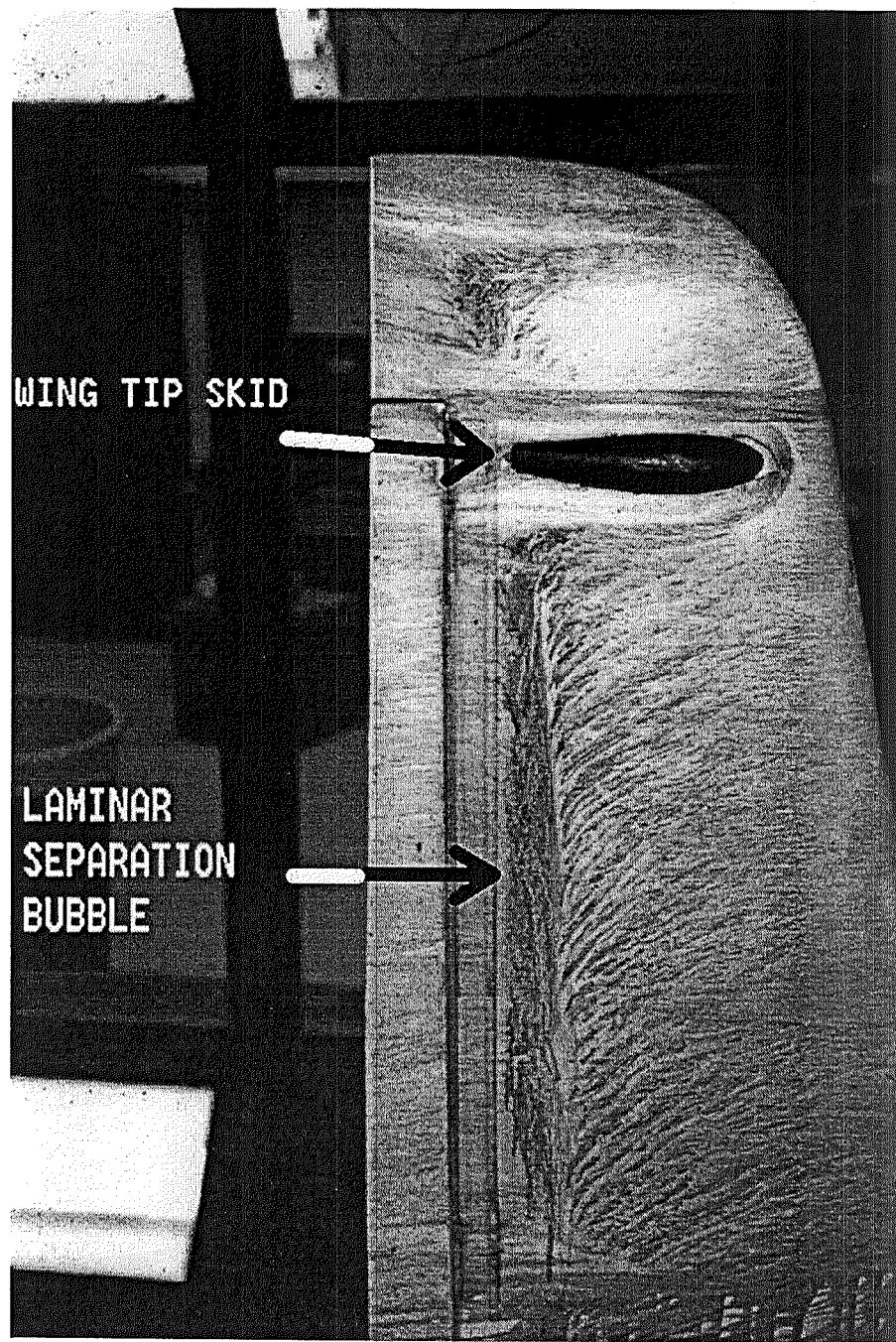


Figure 16. Flow Visualization of Standard Wing Tip Pressure Side.
 $\alpha = 2.5^\circ$, $Q = 10.85 \text{ lb/ft}^2$

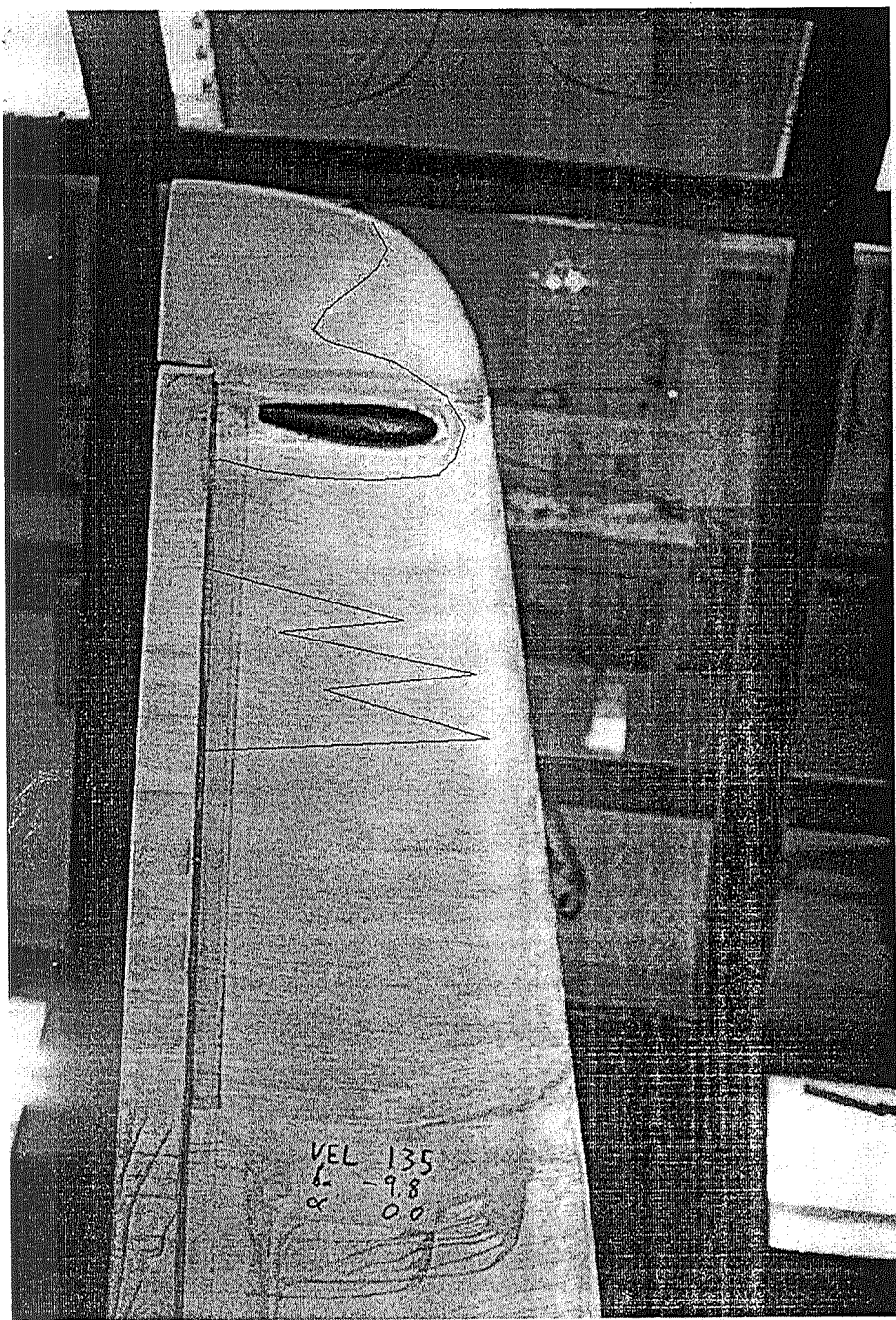


Figure 17. Flow Visualization of Standard Wing Tip Pressure Side.
 $\alpha = 0^\circ$, $Q = 40.6 \text{ lb/ft}^2$

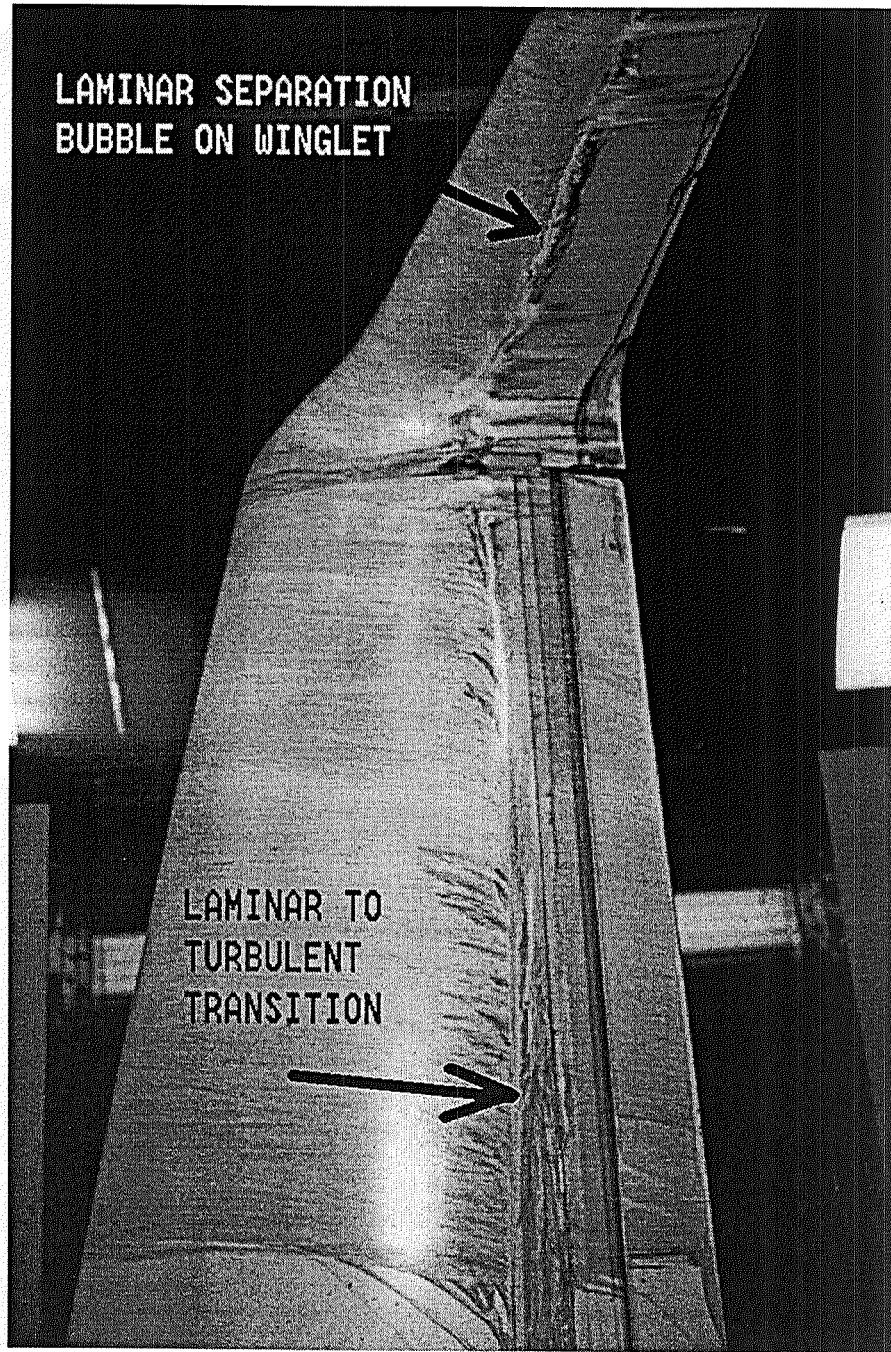


Figure 18. Flow Visualization of Winglet Suction Side.
 $\alpha = 0^\circ$, $Q = 10.85 \text{ lb/ft}^2$

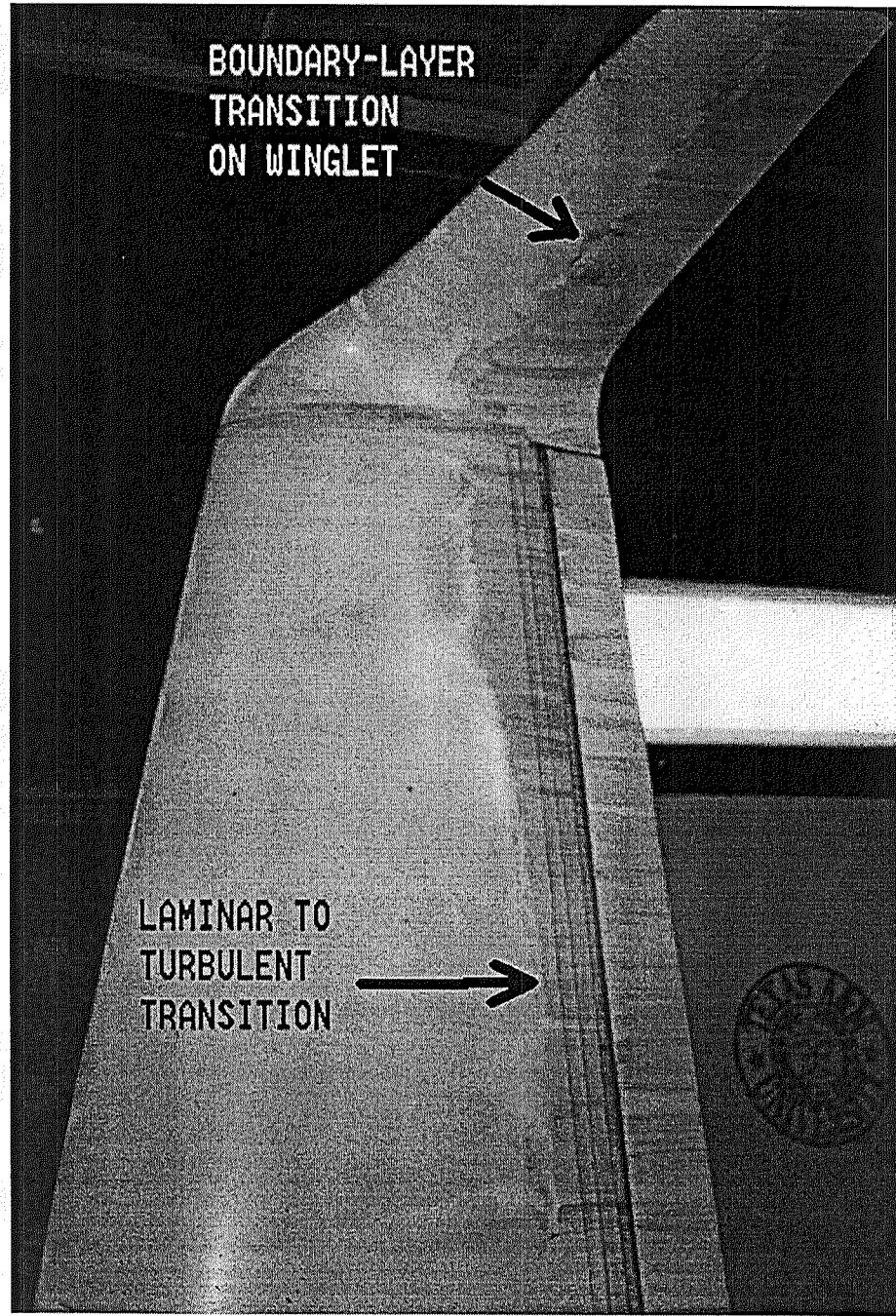


Figure 19. Flow Visualization of Winglet Suction Side.
 $\alpha = 0^\circ$, $Q = 40.6 \text{ lb/ft}^2$

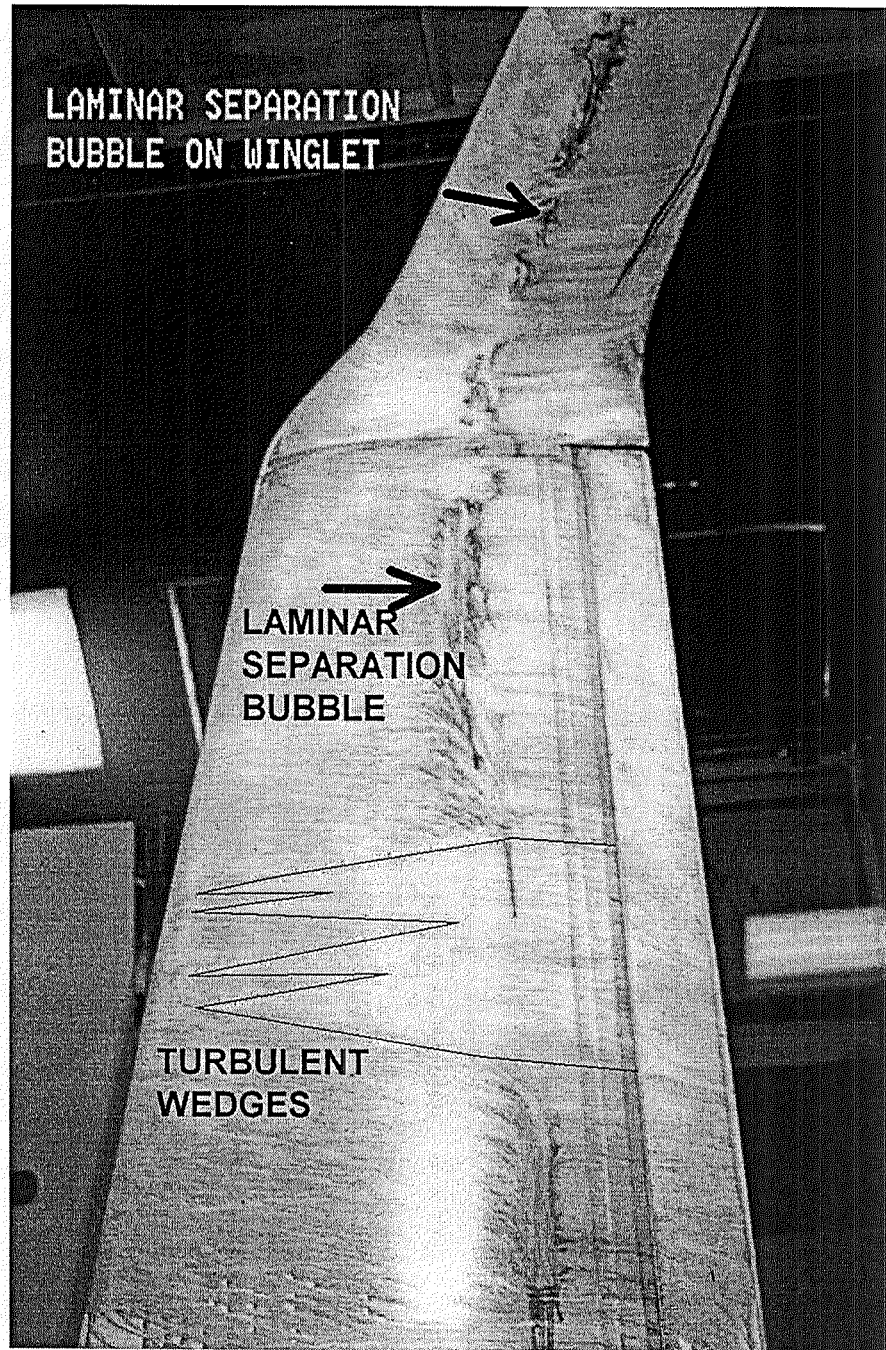


Figure 20. Flow Visualization of Winglet Suction Side.
 $\alpha = 2.5^\circ$, $Q = 10.85 \text{ lb/ft}^2$

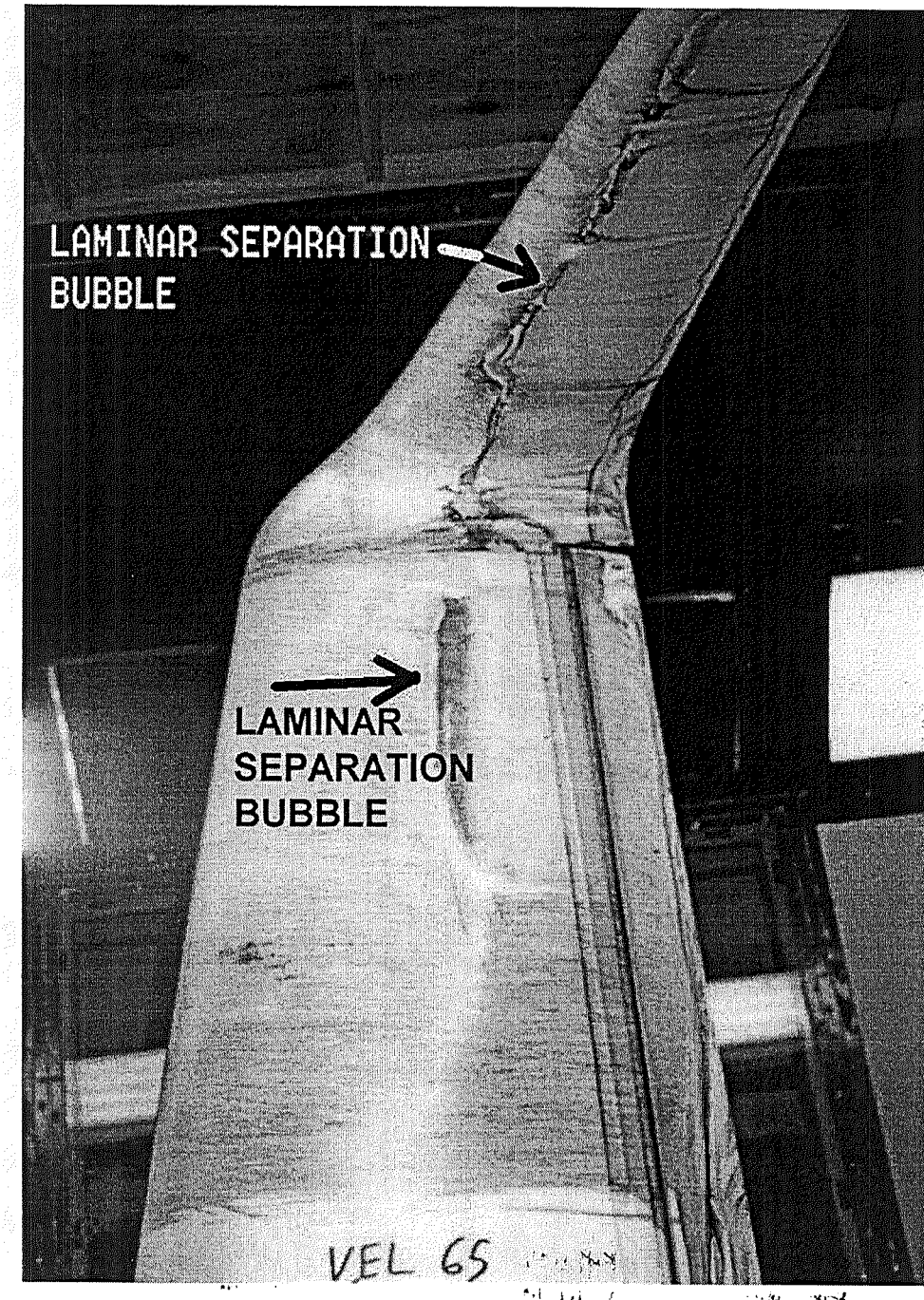


Figure 21. Flow Visualization of Winglet Suction Side.
 $\alpha = 5.0^\circ$, $Q = 10.85 \text{ lb/ft}^2$

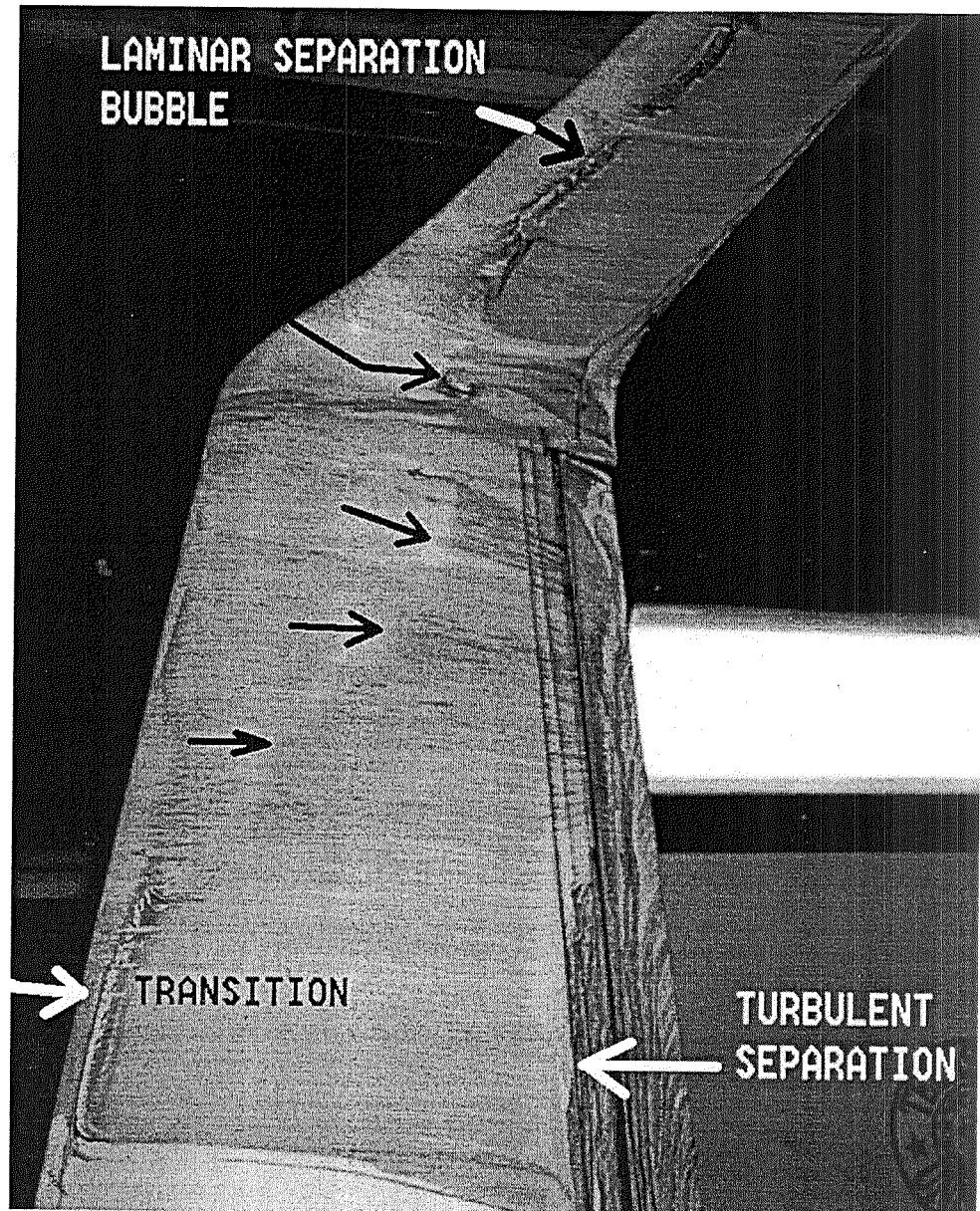


Figure 22. Flow Visualization of Winglet Suction Side.
 $\alpha = 7.5^\circ$, $Q = 10.85 \text{ lb/ft}^2$

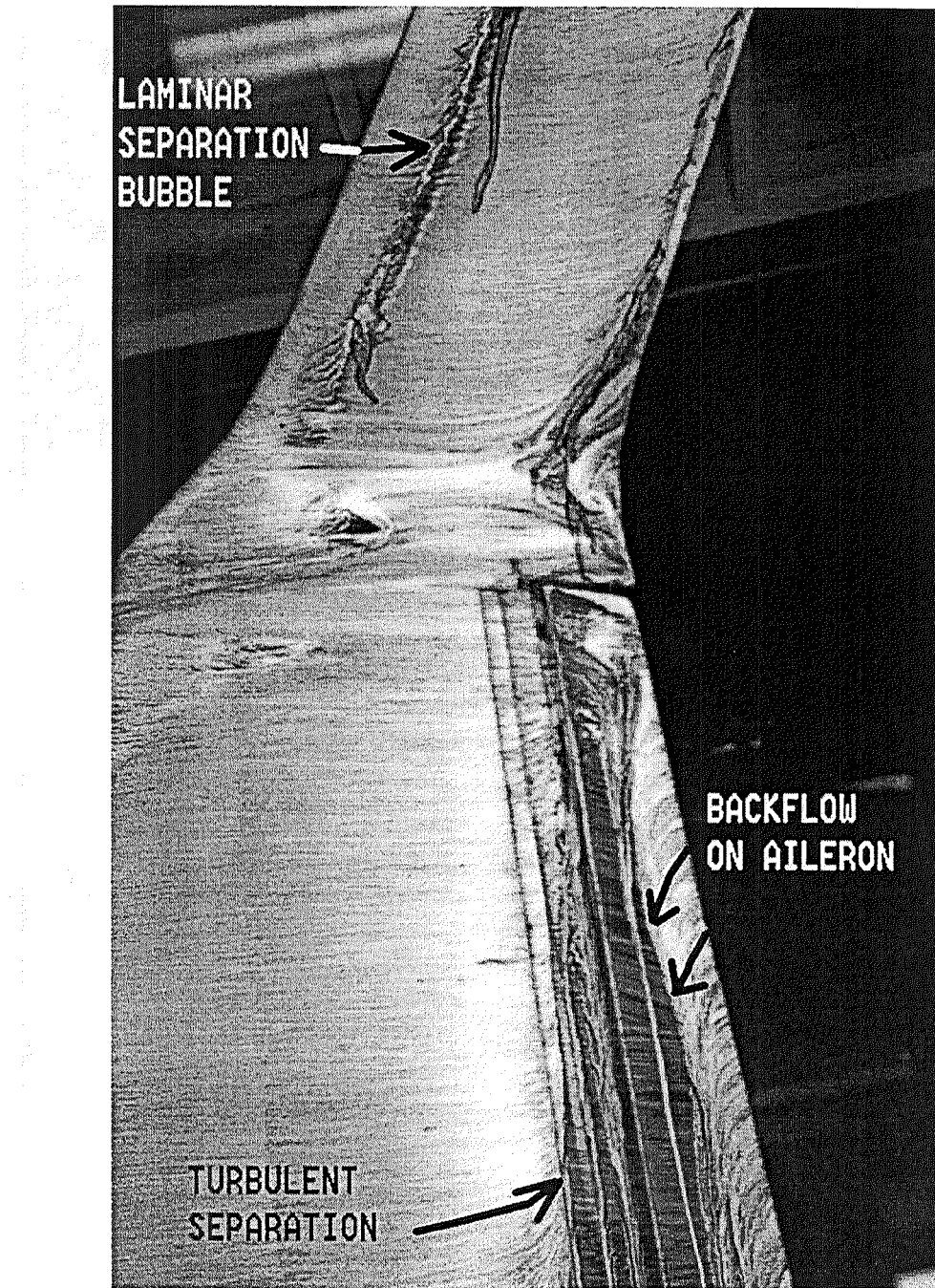


Figure 23. Flow Visualization of Winglet Suction Side.
 $\alpha = 10.0^\circ$, $Q = 10.85 \text{ lb/ft}^2$

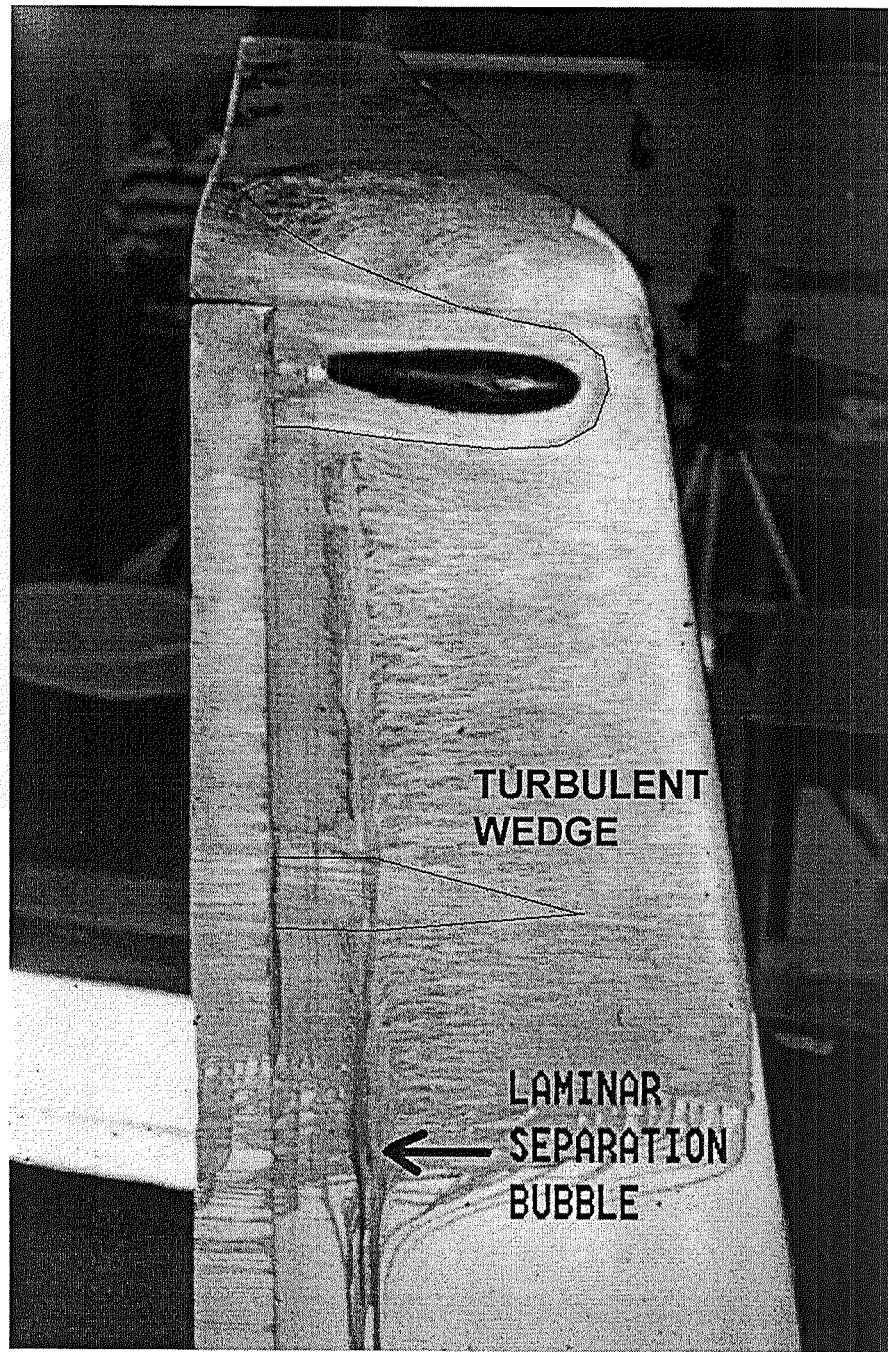


Figure 24. Flow Visualization of Winglet Pressure Side.
 $\alpha = 0^\circ$, $Q = 10.85 \text{ lb/ft}^2$

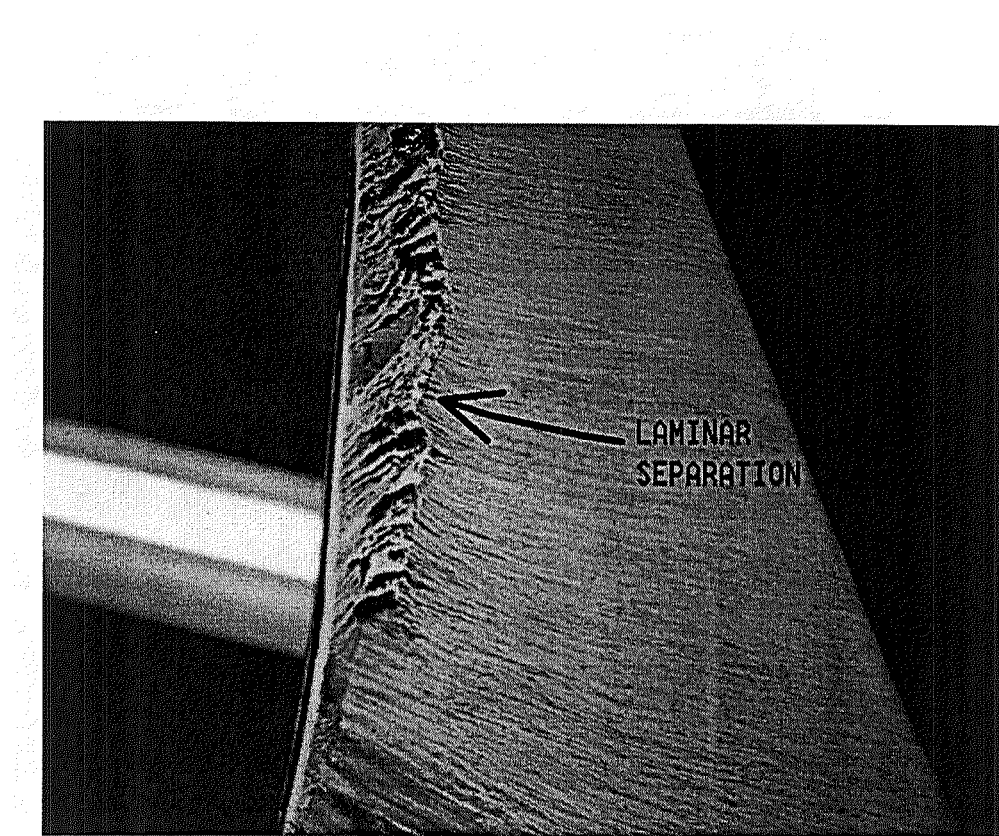


Figure 25. Flow Visualization of Winglet Pressure Side. Laminar Separation. $\alpha = 2.5^\circ$, $Q = 10.85 \text{ lb/ft}^2$

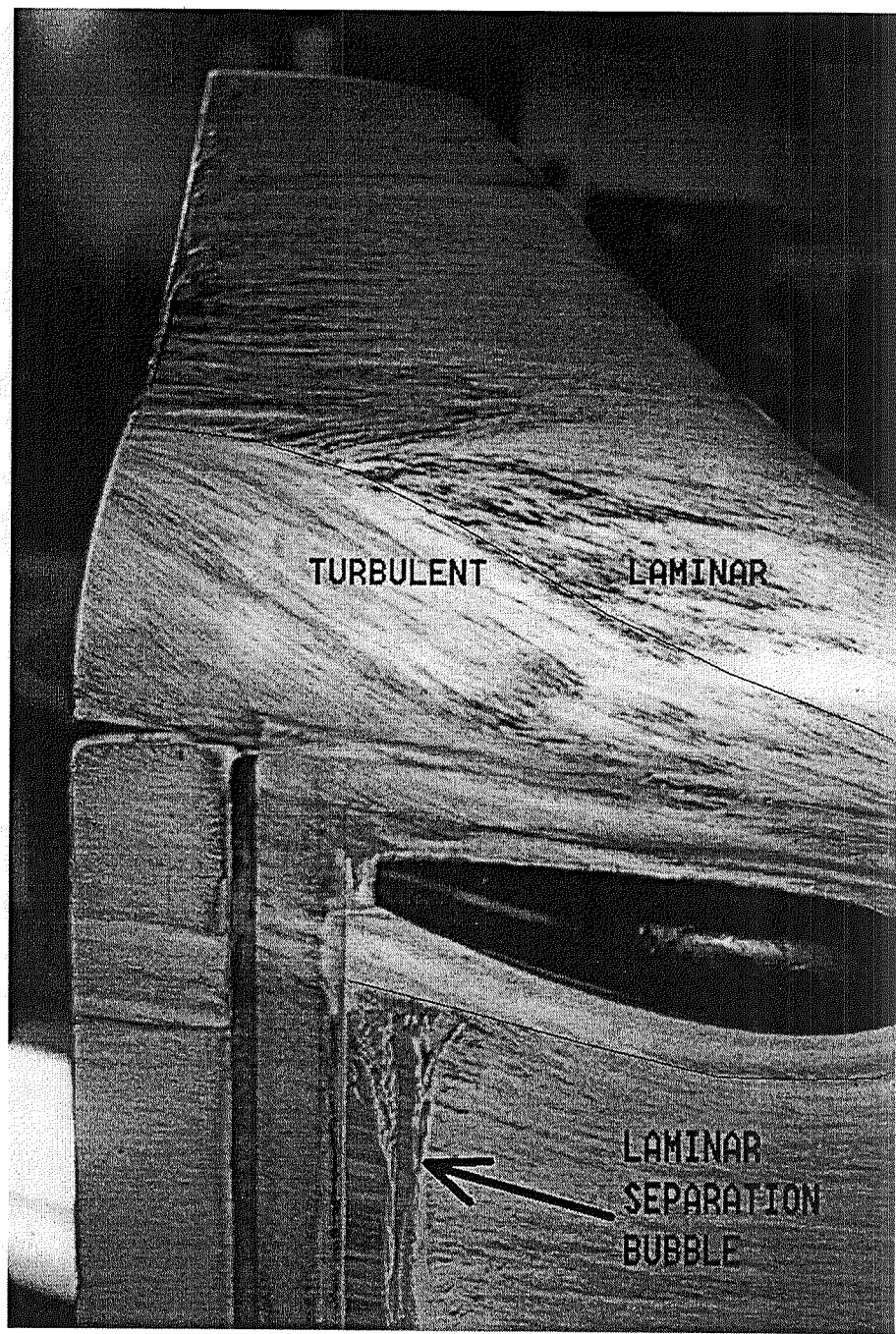


Figure 26. Flow Visualization of Winglet Pressure Side. Laminar Flow to 98 Percent. $\alpha = 10.0^\circ$, $Q = 10.85 \text{ lb/ft}^2$

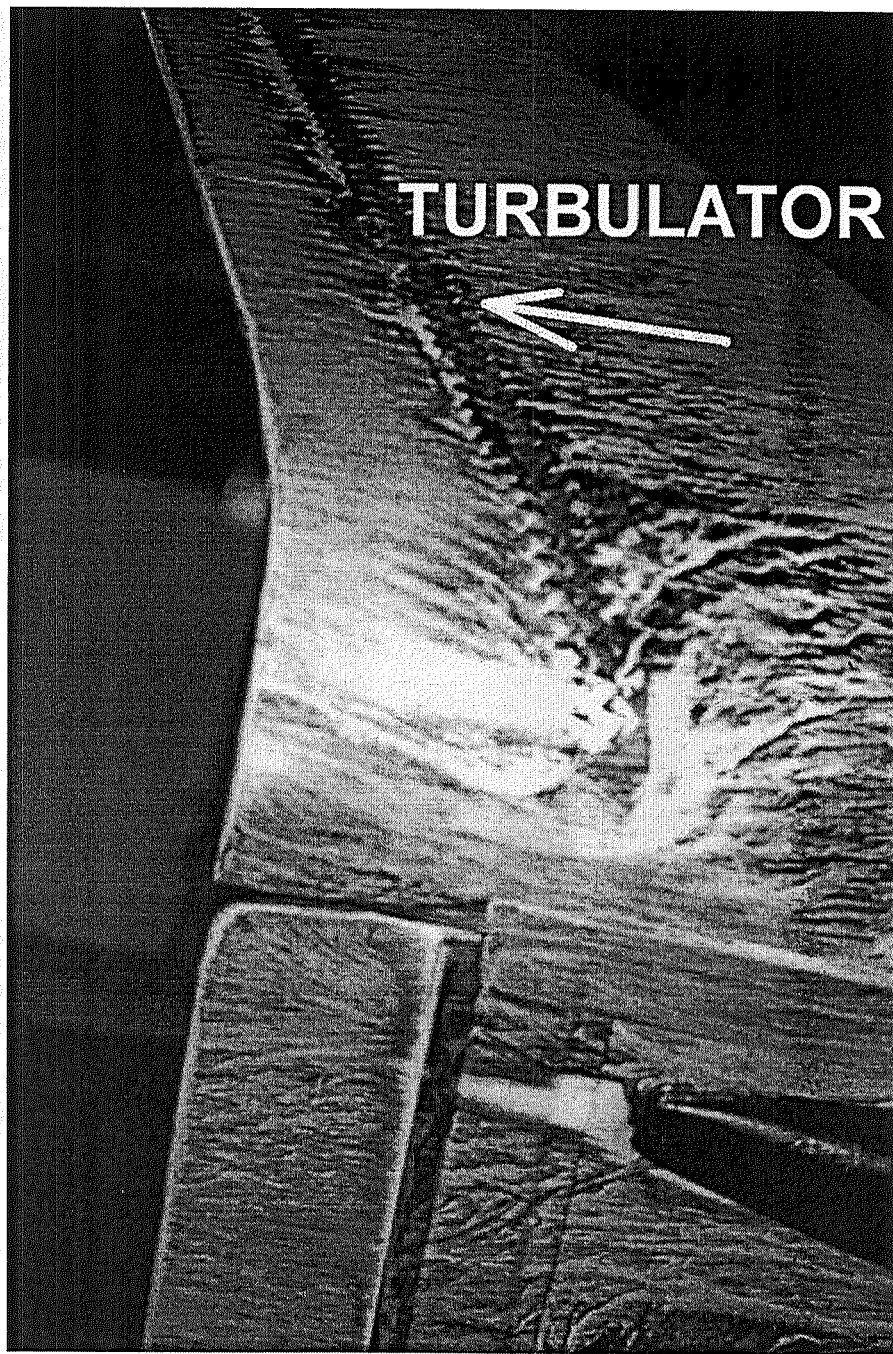


Figure 27. Installation of Turbulator Strip on Pressure Side of Winglet Prevents Laminar Flow Separation.

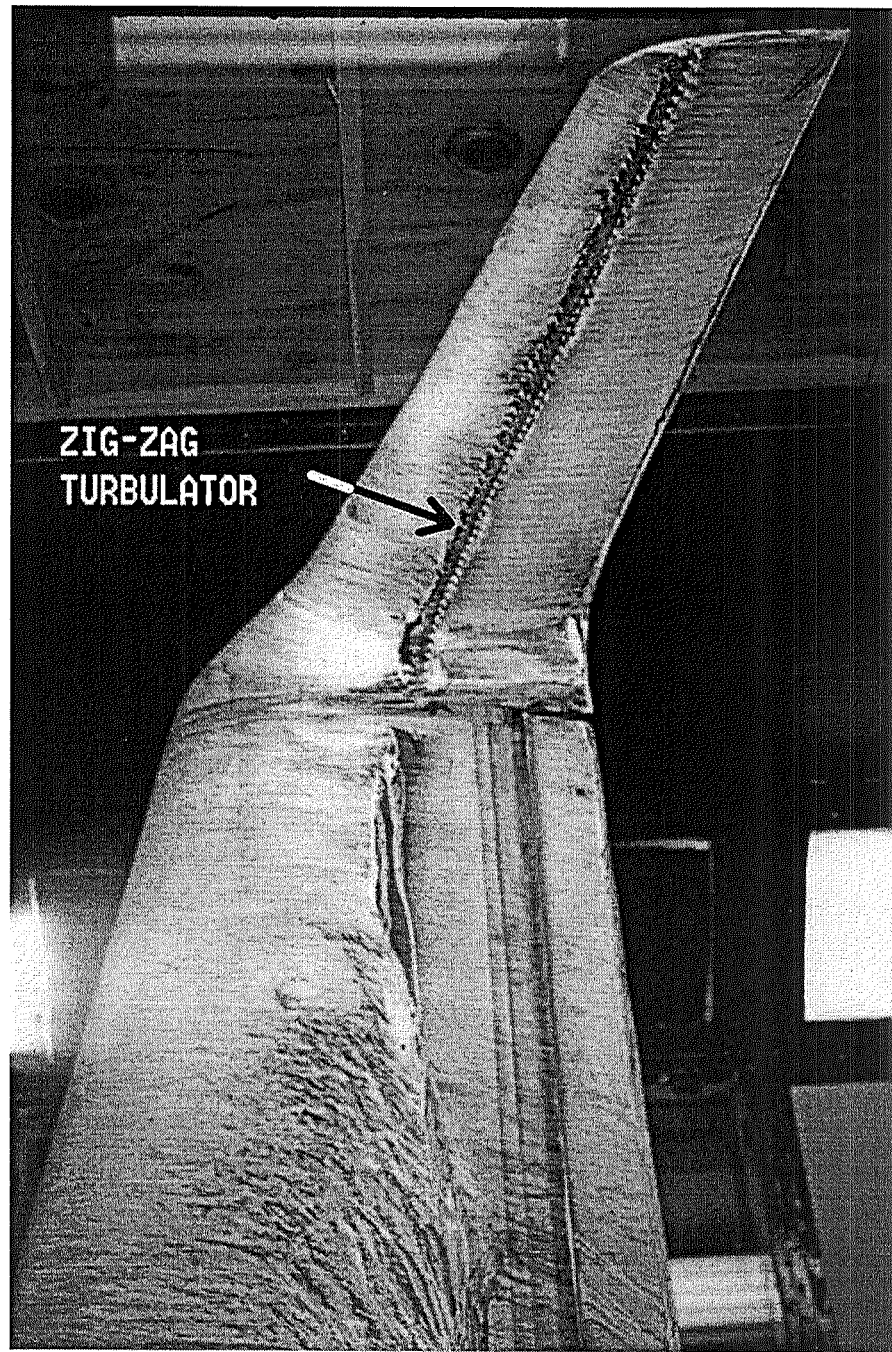


Figure 28. Installation of Turbulator Strip on Suction Side of Winglet Prevents Laminar Separation Bubble.

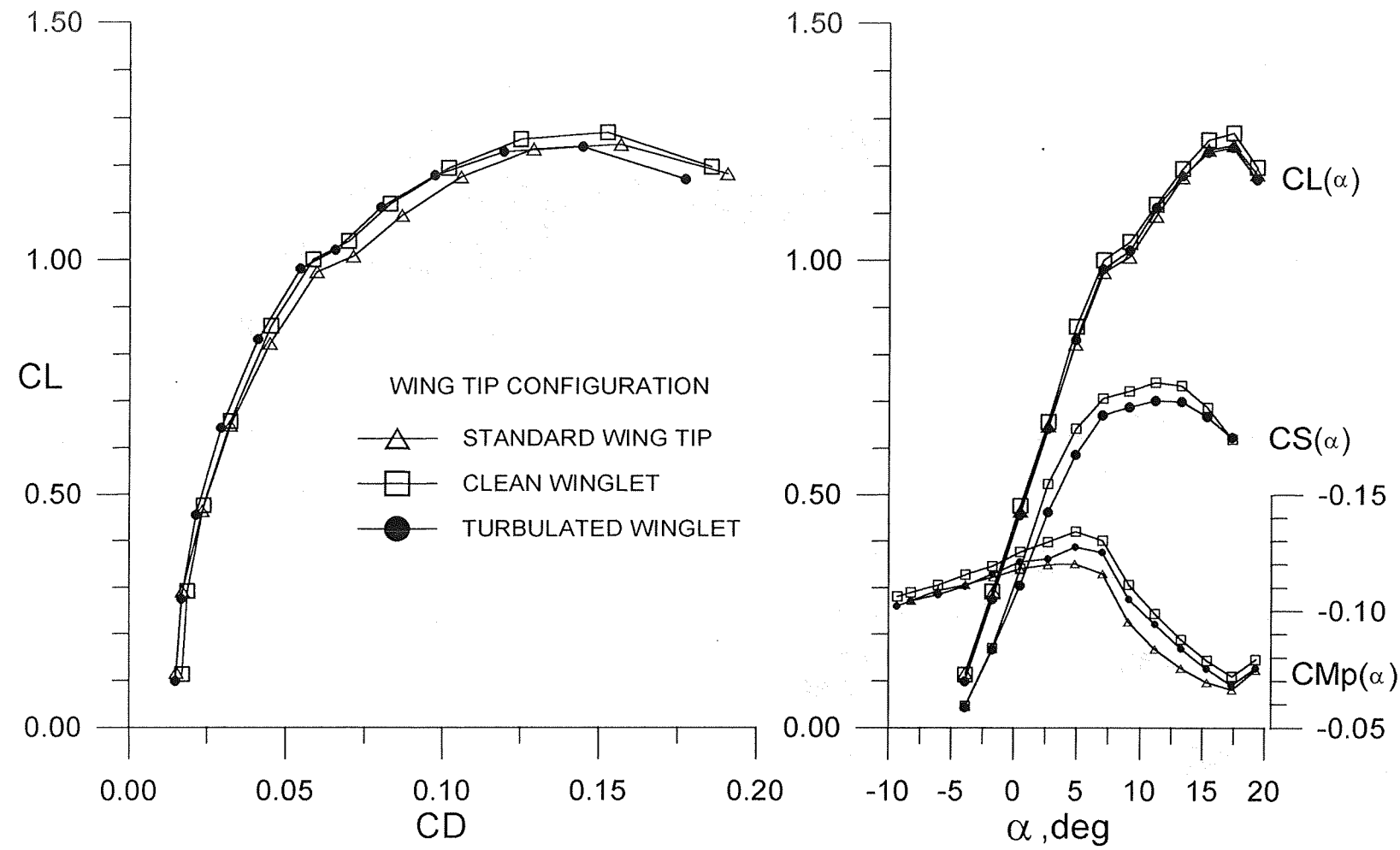


Figure 29. Drag Polar, Lift Curve, Side Force Curve, and Pitching Moment Coefficients for the Standard Wing Tip, Clean Winglet, and Turbulated Winglet. Reynolds Number $6.1 \times 10^5 \text{ ft}^{-1}$.

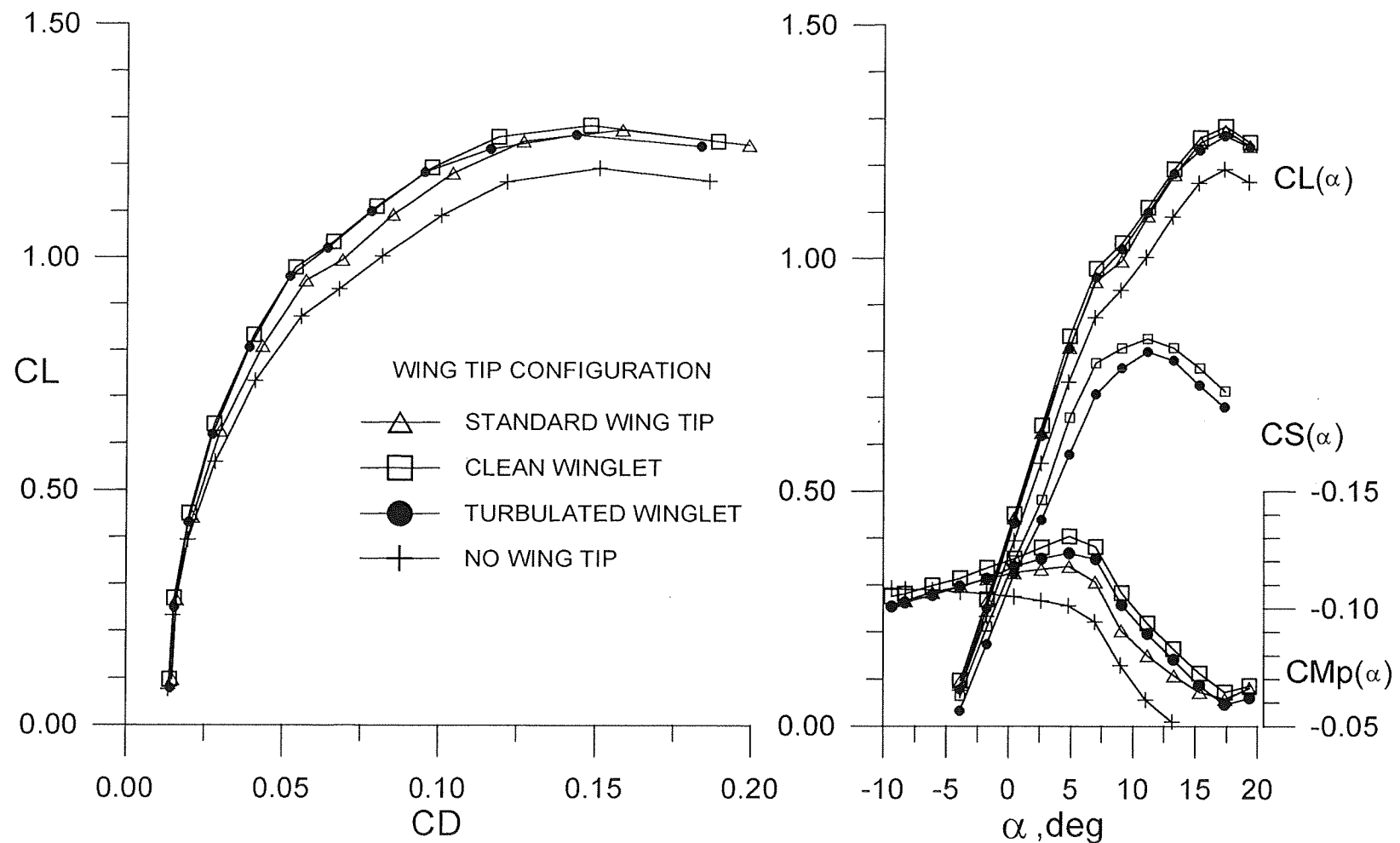


Figure 30. Drag Polar, Lift Curve, Side Force Curve, and Pitching Moment Coefficients for the Standard Wing Tip, Clean Winglet, and Turbulated Winglet. Reynolds Number $8.2 \times 10^5 \text{ ft}^{-1}$.

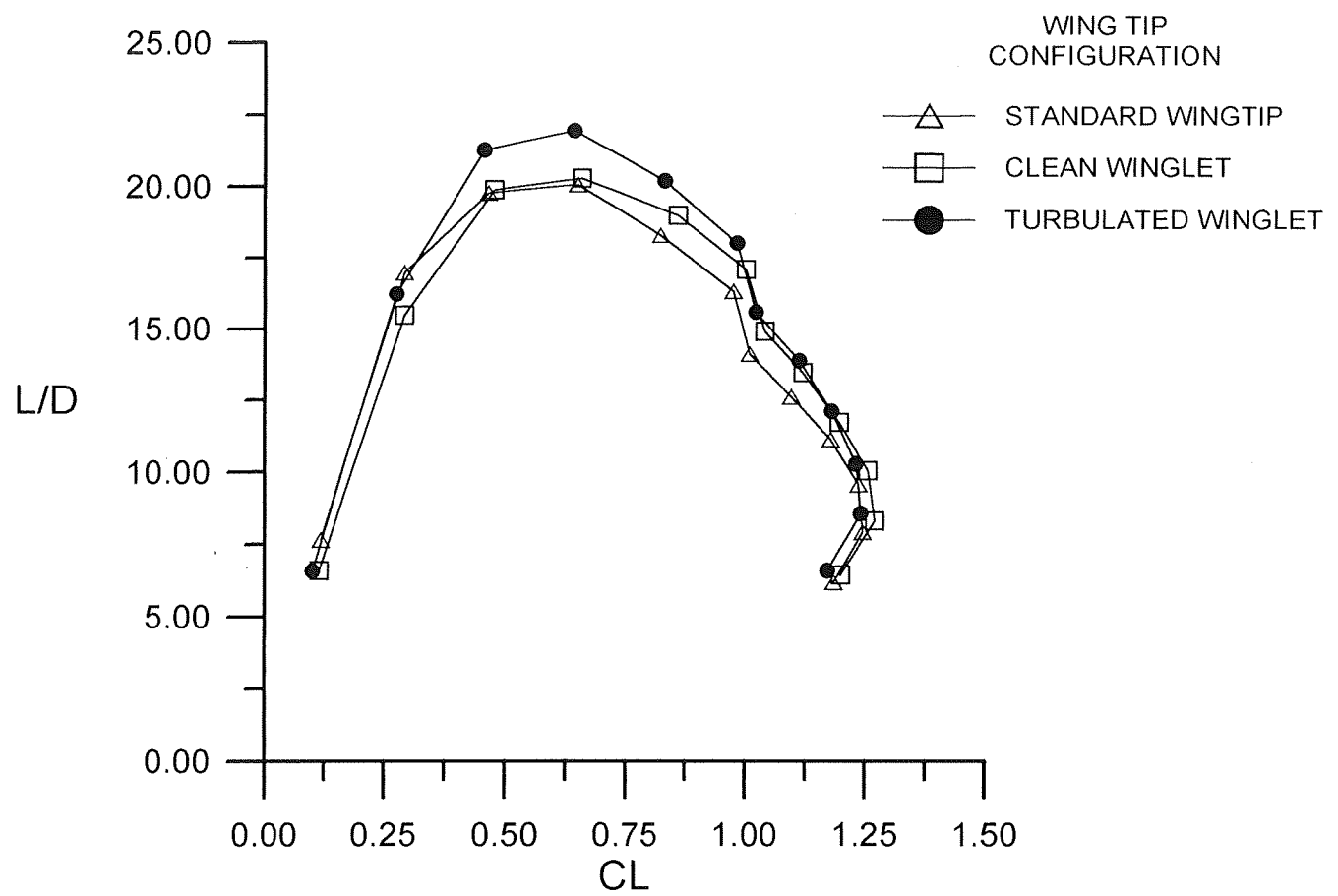


Figure 31. Lift to Drag Ratio for Standard Wing Tip, Clean Winglet , and Turbulated Winglet.
Reynolds Number $6.1 \times 10^5 \text{ ft}^3$.

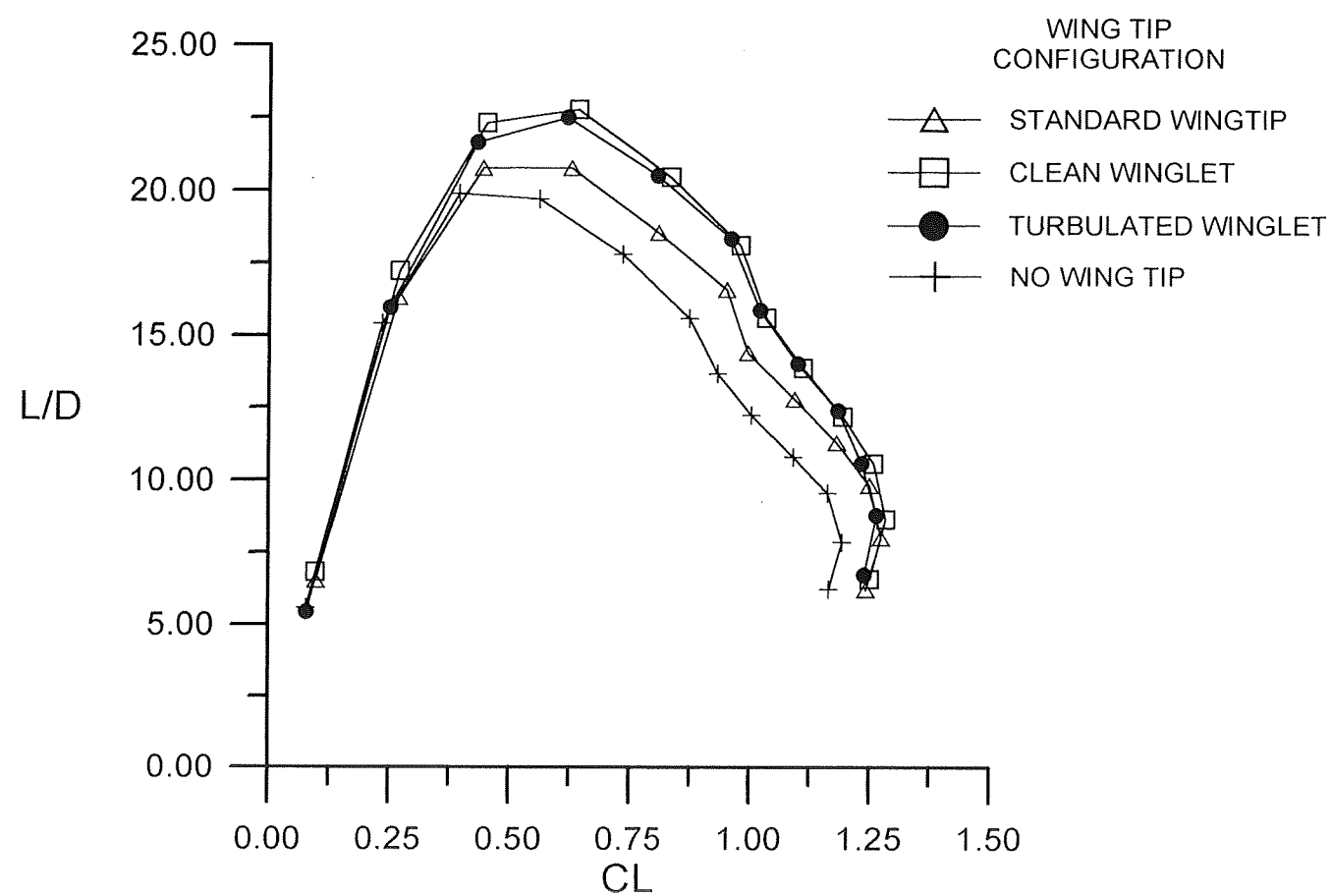


Figure 32. Lift to Drag Ratio for Standard Wing Tip, Clean Winglet , and Turbulated Winglet.
Reynolds Number $8.2 \times 10^5 \text{ ft}^{-1}$.

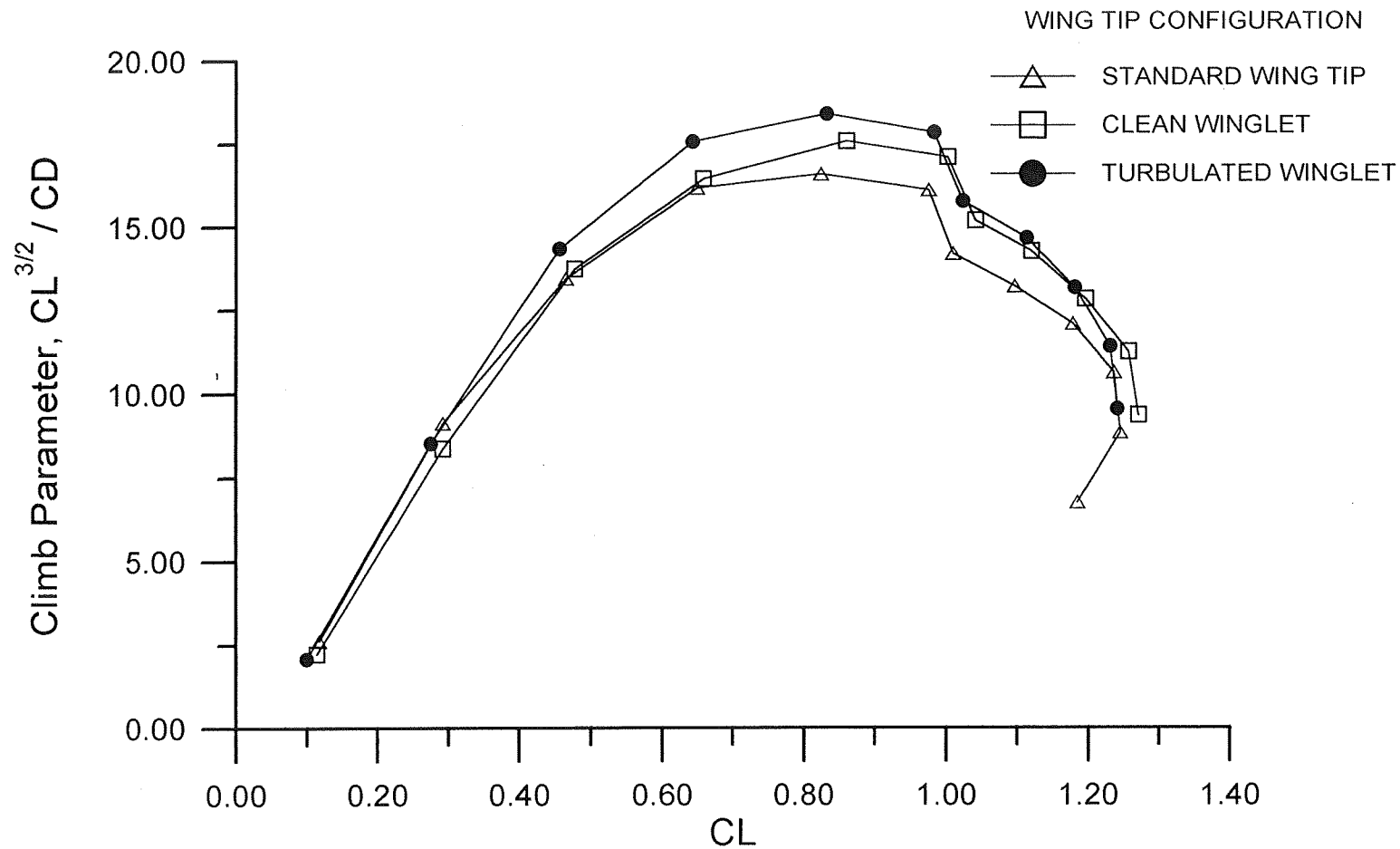


Figure 33. Climb Parameter for Standard Wing Tip, Clean Winglet , and Turbulated Winglet.
Reynolds Number $6.1 \times 10^5 \text{ ft}^{-1}$.

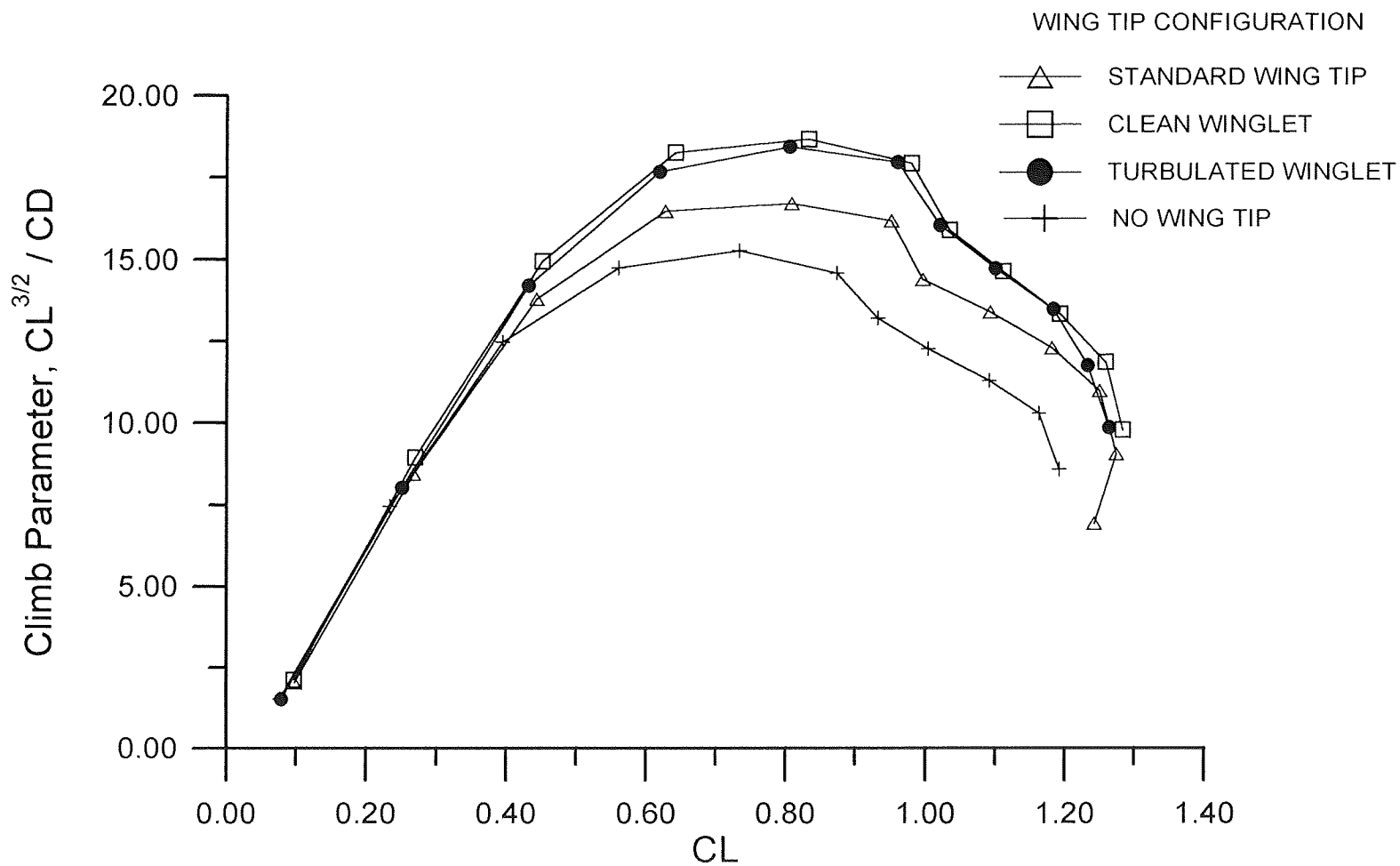


Figure 34. Climb Parameter for Standard Wing Tip, Clean Winglet , and Turbulated Winglet.
Reynolds Number $8.2 \times 10^5 \text{ ft}^{-1}$.

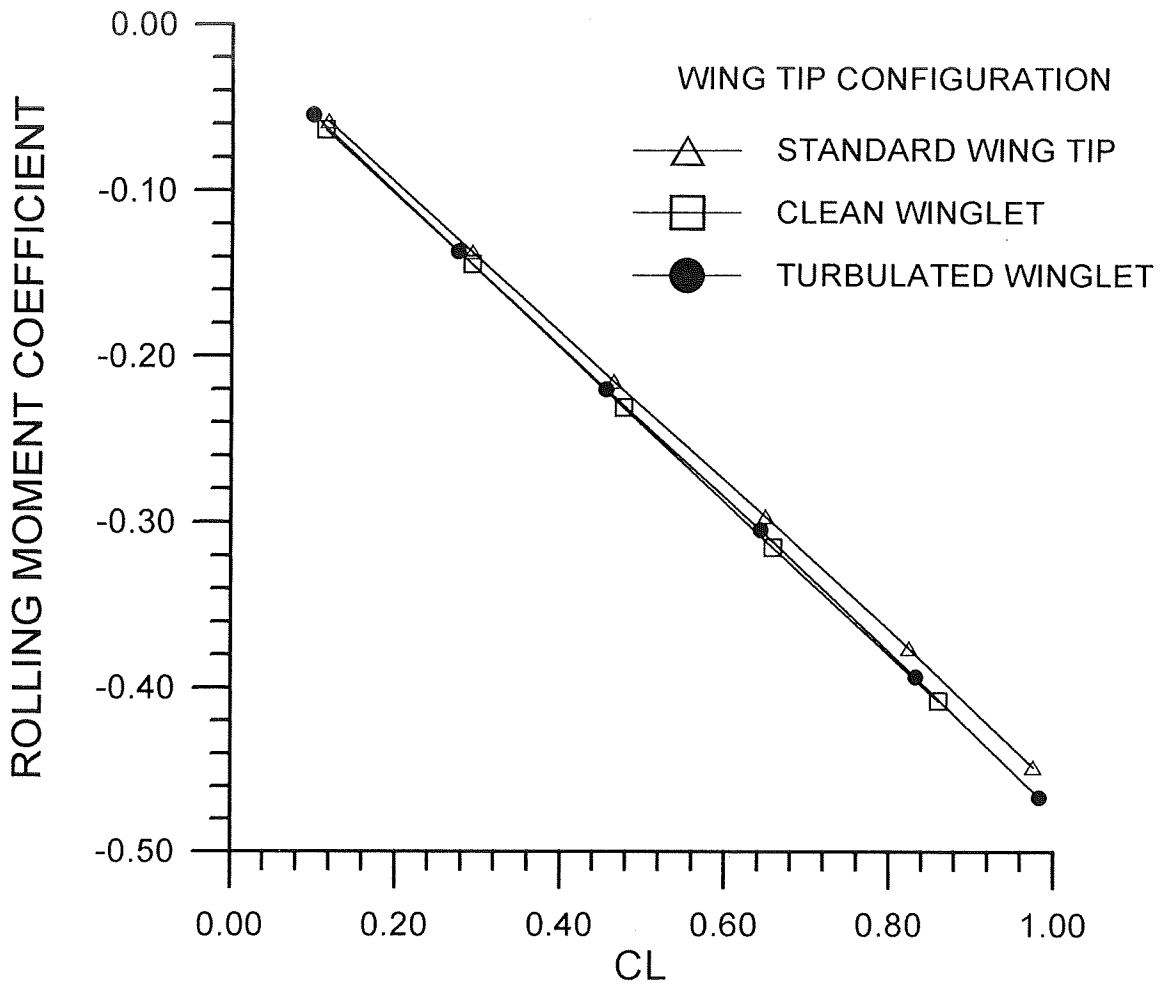


Figure 35. Rolling Moment for Standard Wing Tip, Clean Winglet , and Turbulated Winglet.
Reynolds Number $6.1 \times 10^5 \text{ ft}^{-1}$.

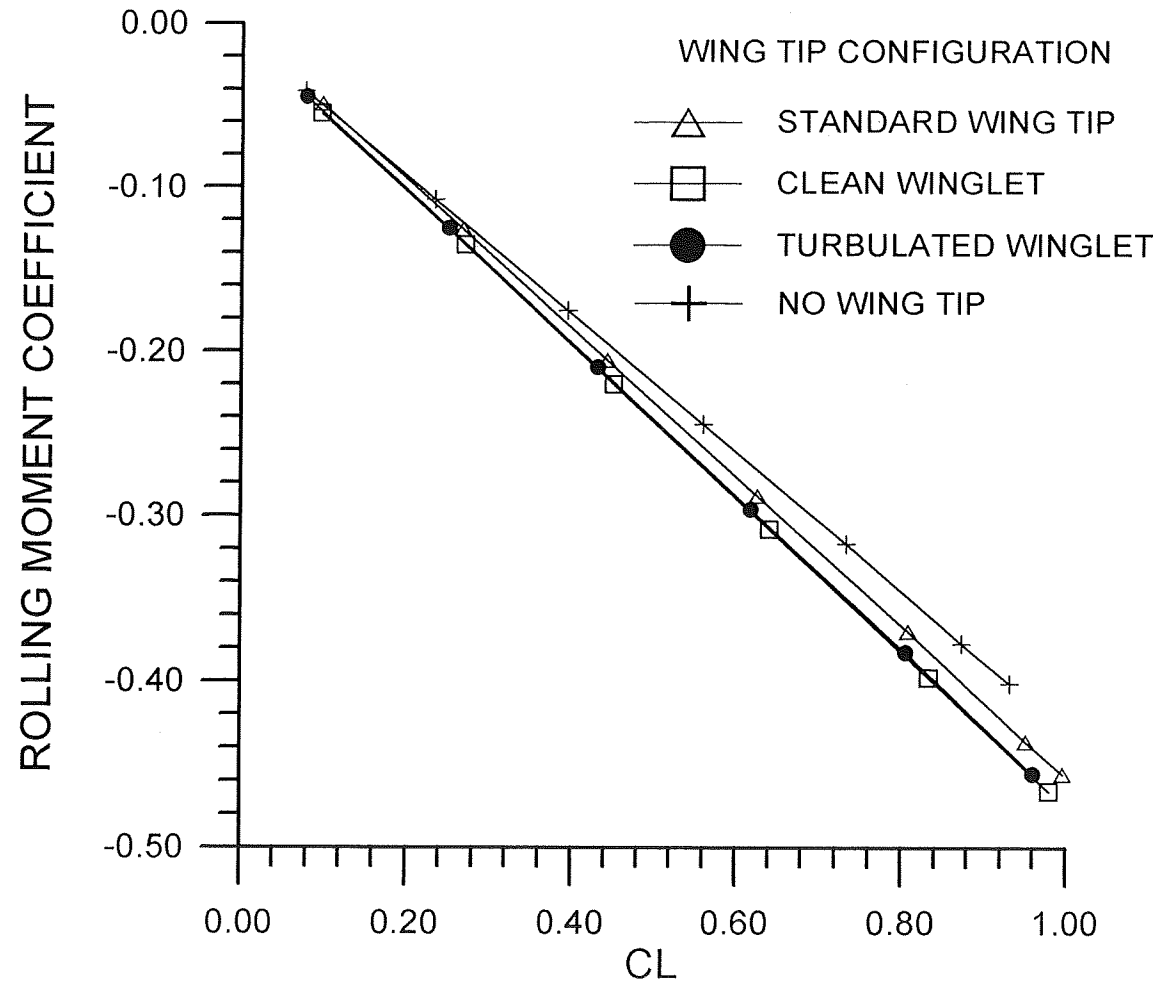


Figure 36. Rolling Moment for Standard Wing Tip, Clean Winglet , and Turbulated Winglet.
 Reynolds Number $8.2 \times 10^5 \text{ ft}^{-1}$.

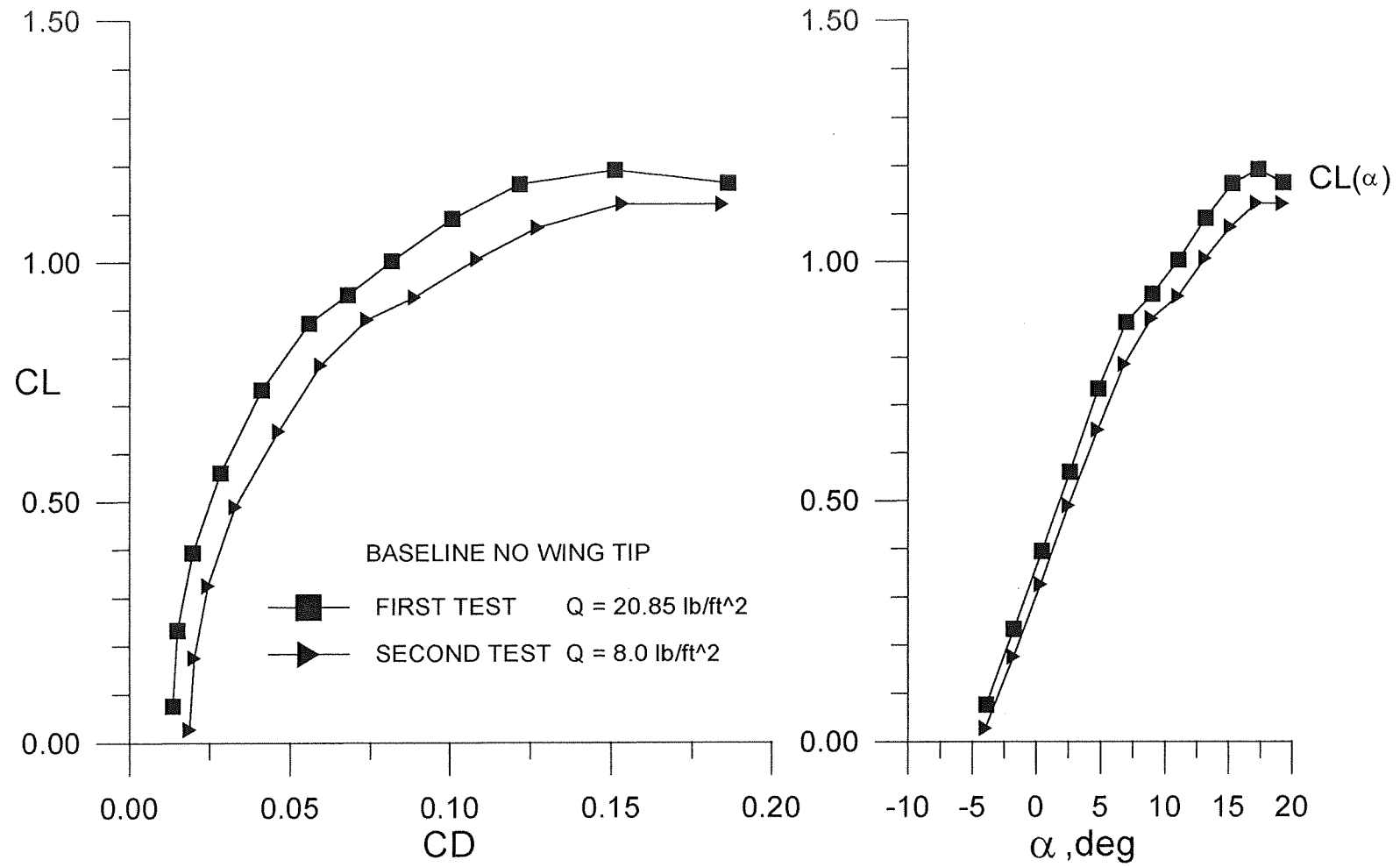


Figure 37. Drag Polar and Lift Curve of Baseline Comparison for the First and Second Wind-Tunnel Test.

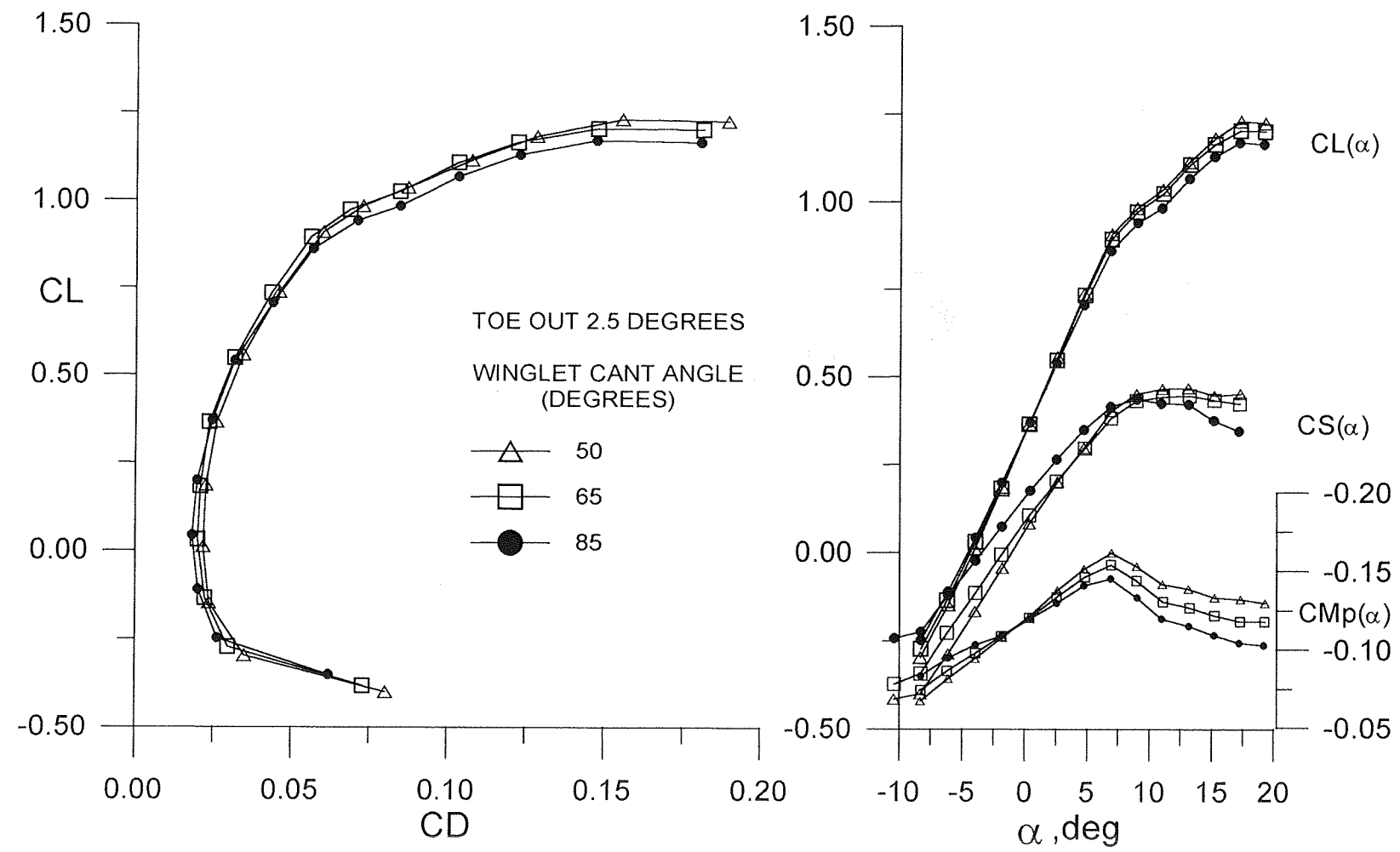


Figure 38. Effects of Cant Angle on the Drag Polar, Lift Curve, Side Force Curve, and Pitching Moment Coefficients at a Toe-Out Angle of 2.5 Degrees. Reynolds Number $5.2 \times 10^5 \text{ ft}^{-1}$.

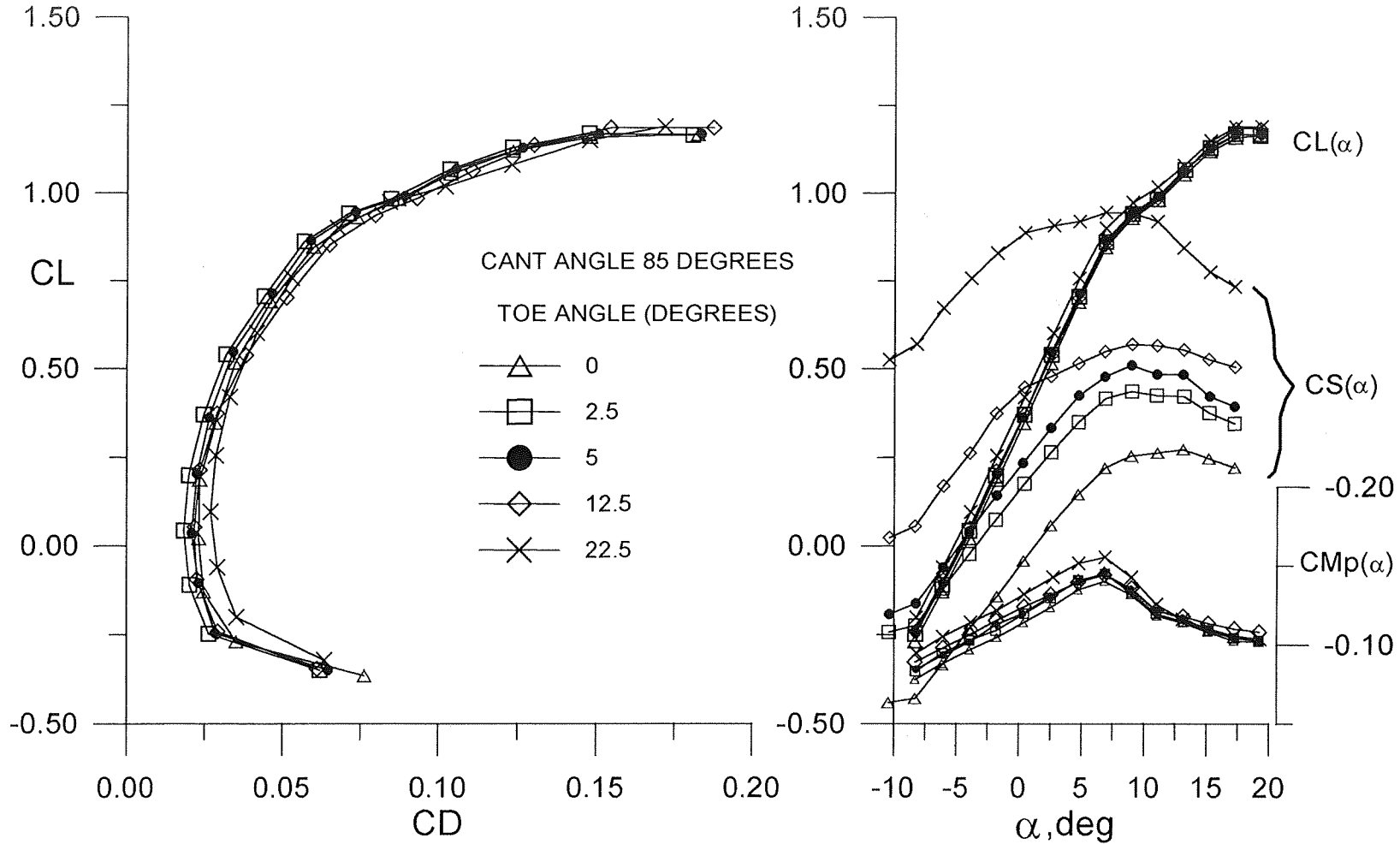


Figure 39. Effects of Toe-Out Angle on the Drag Polar, Lift Curve, Side Force Curve, and Pitching Moment Coefficients at a Cant Angle of 85 Degrees. Reynolds Number $5.2 \times 10^5 \text{ ft}^{-1}$.

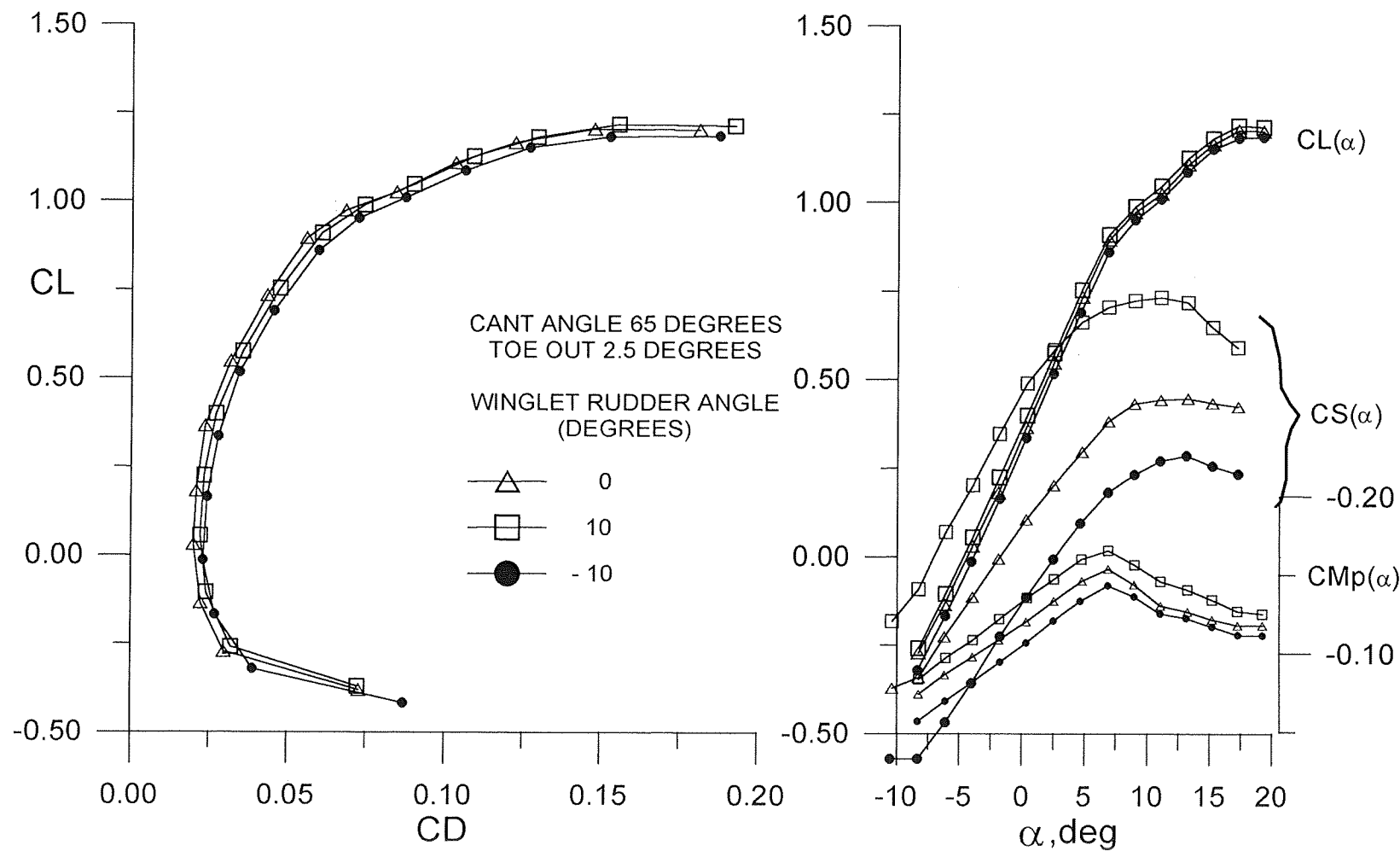


Figure 40. Effects of Winglet Rudder Angle on the Drag Polar, Lift Curve, Side Force Curve, and Pitching Moment Coefficients at a Cant Angle of 65 Degrees, Toe-Out Angle of 2.5 Degrees.
 Reynolds Number $5.2 \times 10^5 \text{ ft}^{-1}$.

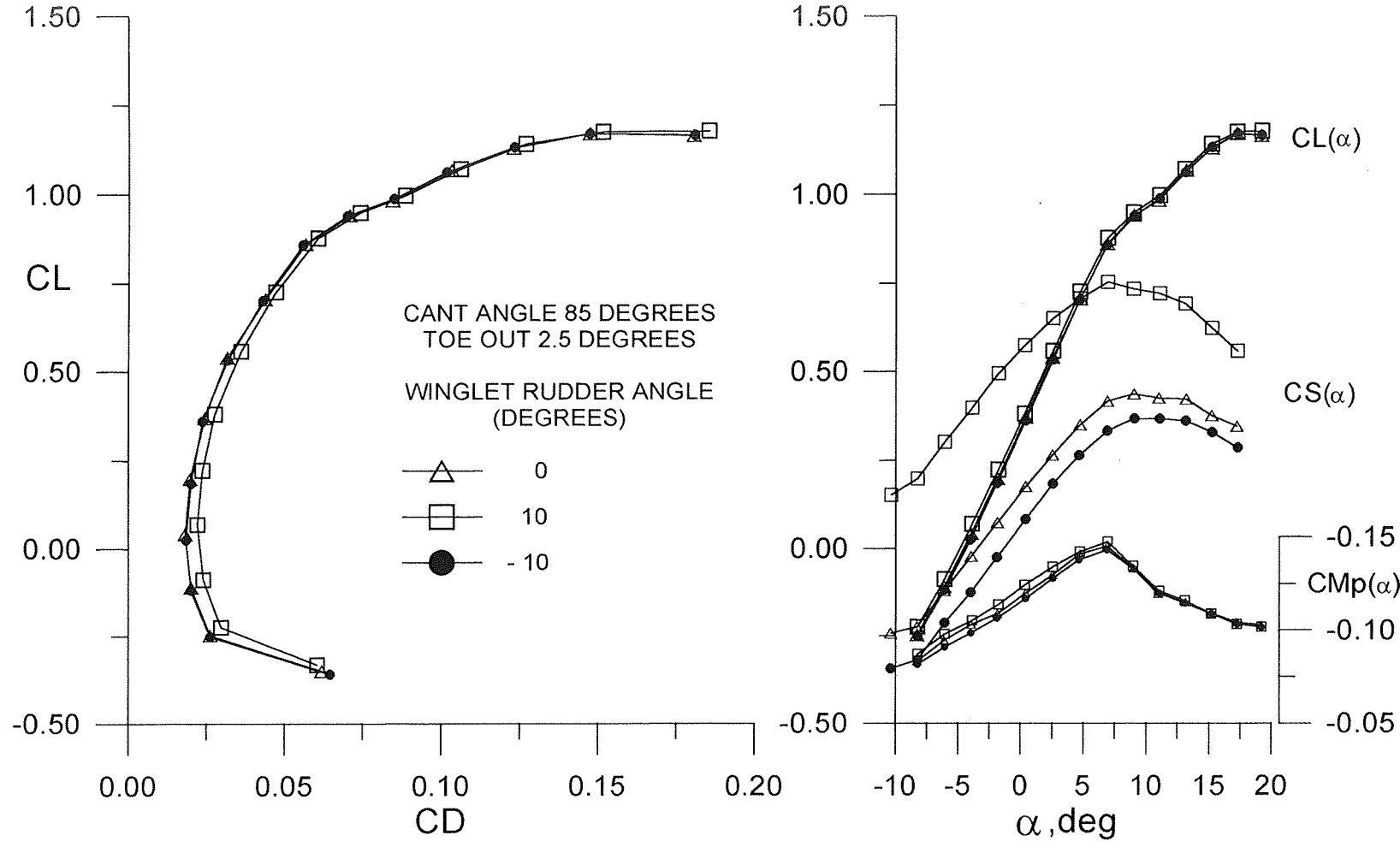


Figure 41. Effects of Winglet Rudder Angle on the Drag Polar, Lift Curve, Side Force Curve, and Pitching Moment Coefficients at a Cant Angle of 85 Degrees, Toe-Out Angle of 2.5 Degrees. Reynolds Number $5.2 \times 10^5 \text{ ft}^{-1}$.

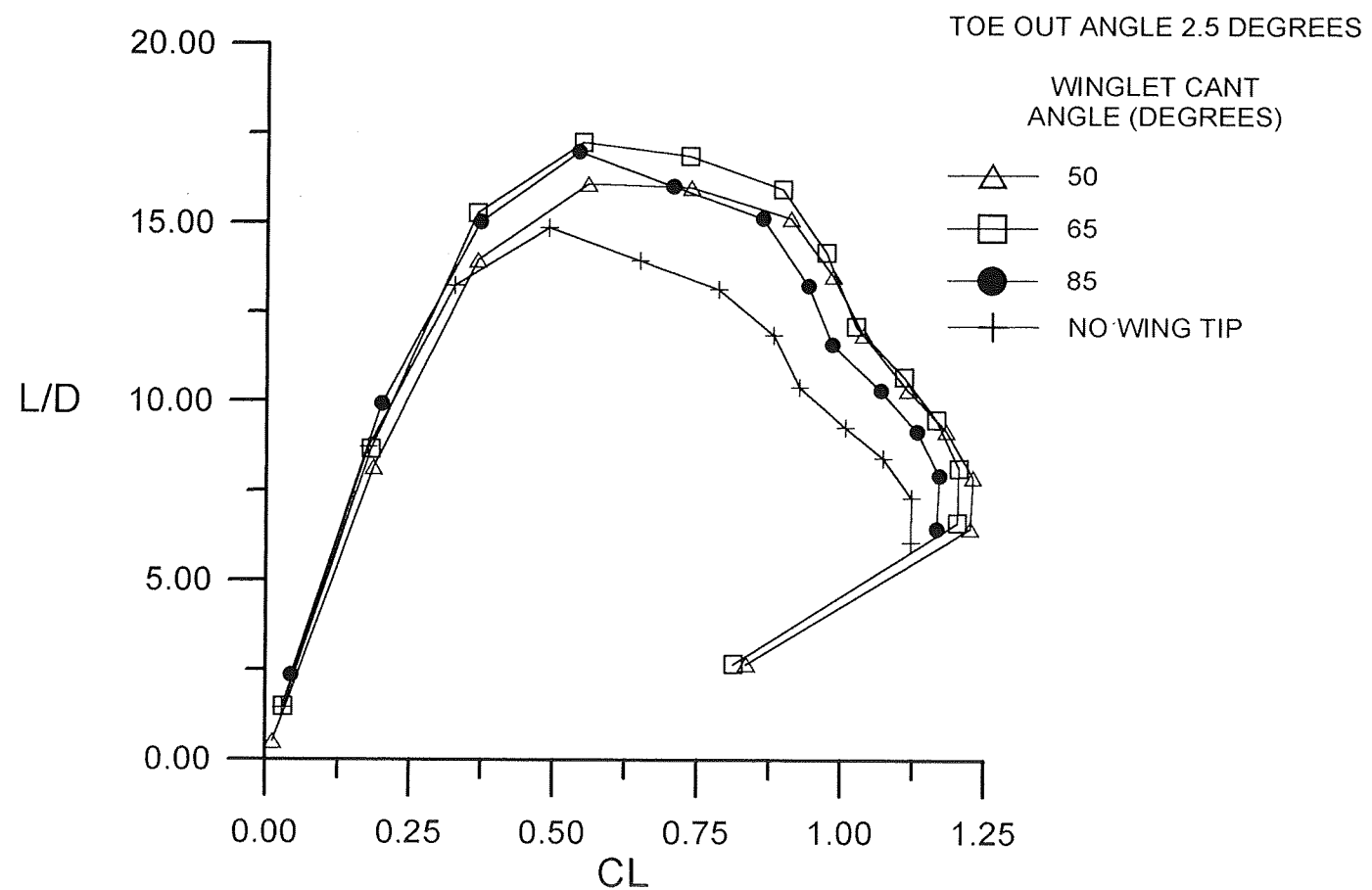


Figure 42. Effects of Cant Angle on the Lift to Drag Ratio at a Toe-Out Angle of 2.5 Degrees.
Reynolds Number $5.2 \times 10^5 \text{ ft}^{-1}$.

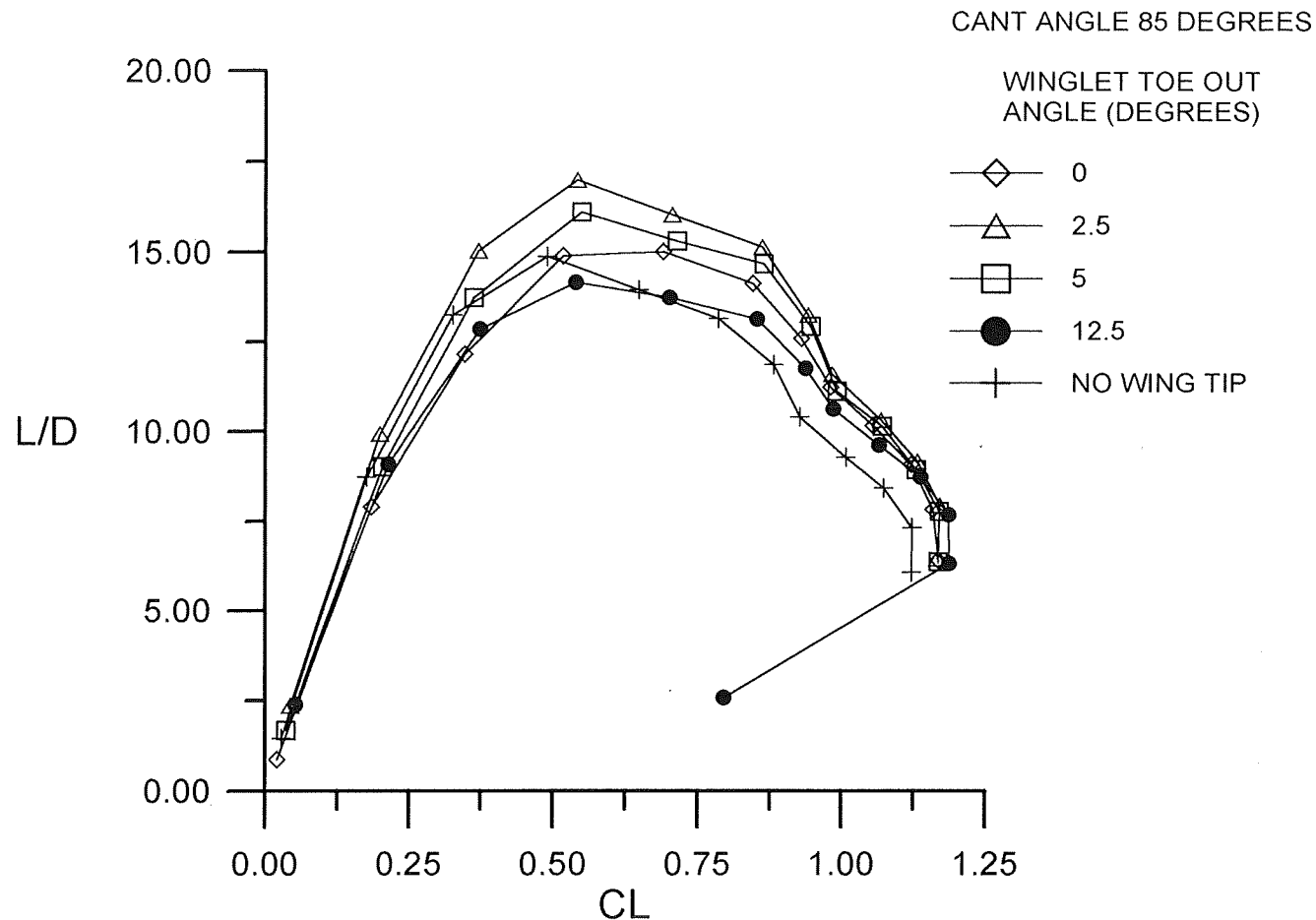


Figure 43. Effects of Toe-Out Angle on the Lift to Drag Ratio at a Cant Angle of 85 Degrees.
Reynolds Number $5.2 \times 10^5 \text{ ft}^{-1}$.

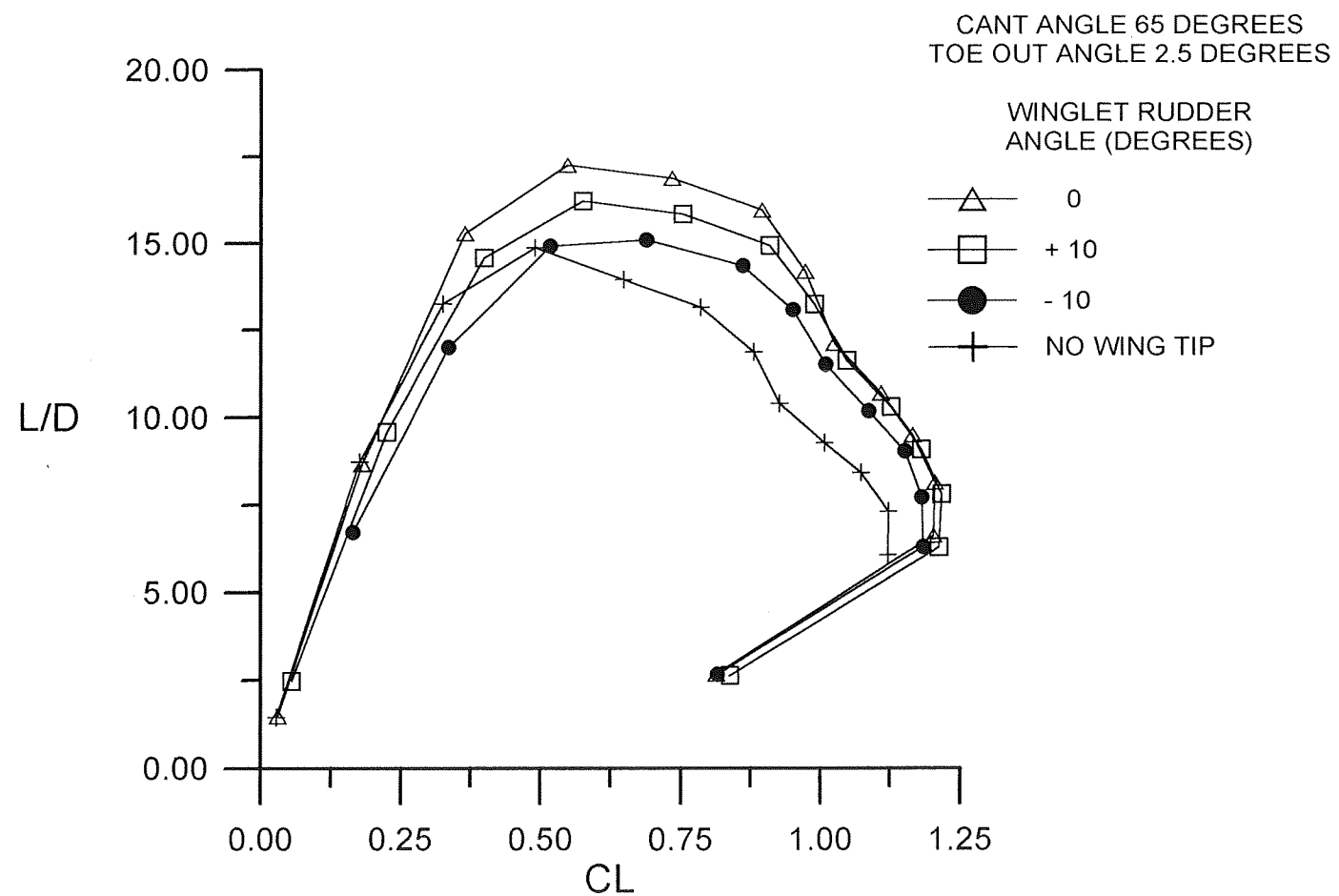


Figure 44. Effects of Winglet Rudder Angle on the Lift to Drag Ratio at a Cant Angle of 65 Degrees, Toe-Out Angle 2.5 Degrees. Reynolds Number $5.2 \times 10^5 \text{ ft}^{-1}$.

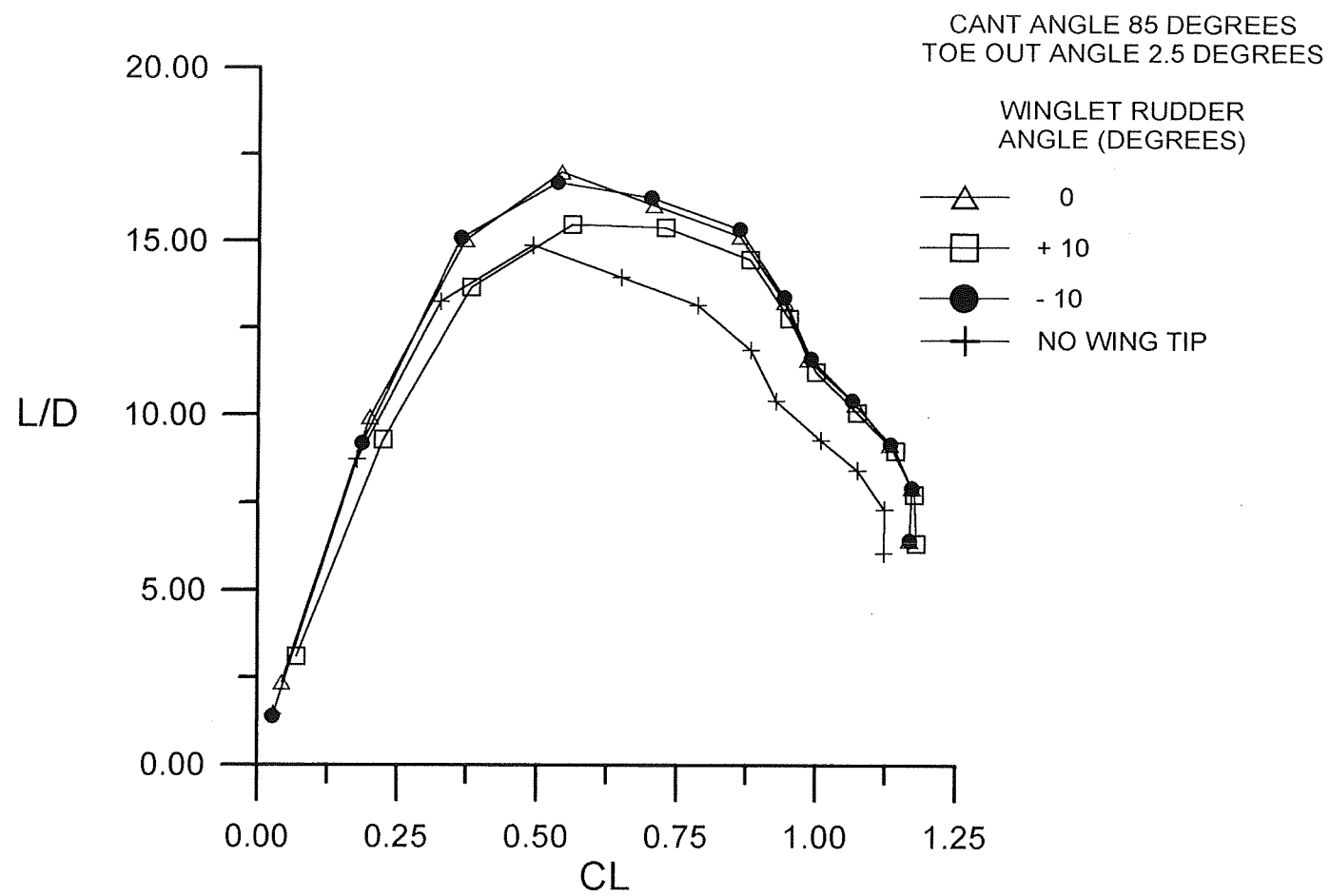


Figure 45. Effects of Winglet Rudder Angle on the Lift to Drag Ratio at a Cant Angle of 85 Degrees, Toe-Out Angle 2.5 Degrees. Reynolds Number $5.2 \times 10^5 \text{ ft}^{-1}$.

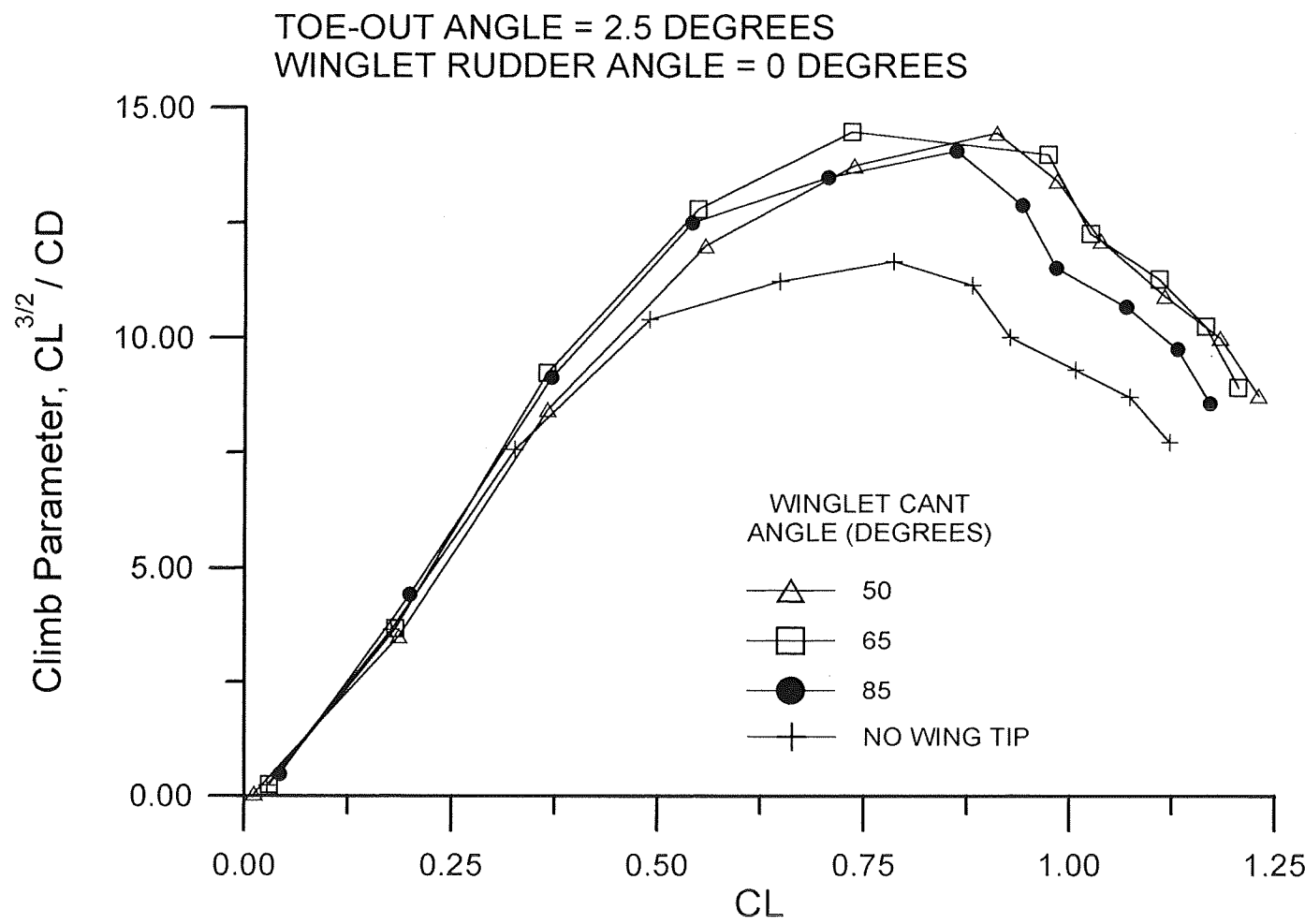


Figure 46. Effects of Cant Angle on the Climb Parameter at a Toe-Out Angle of 2.5 Degrees.
Reynolds Number $5.2 \times 10^5 \text{ ft}^{-1}$.

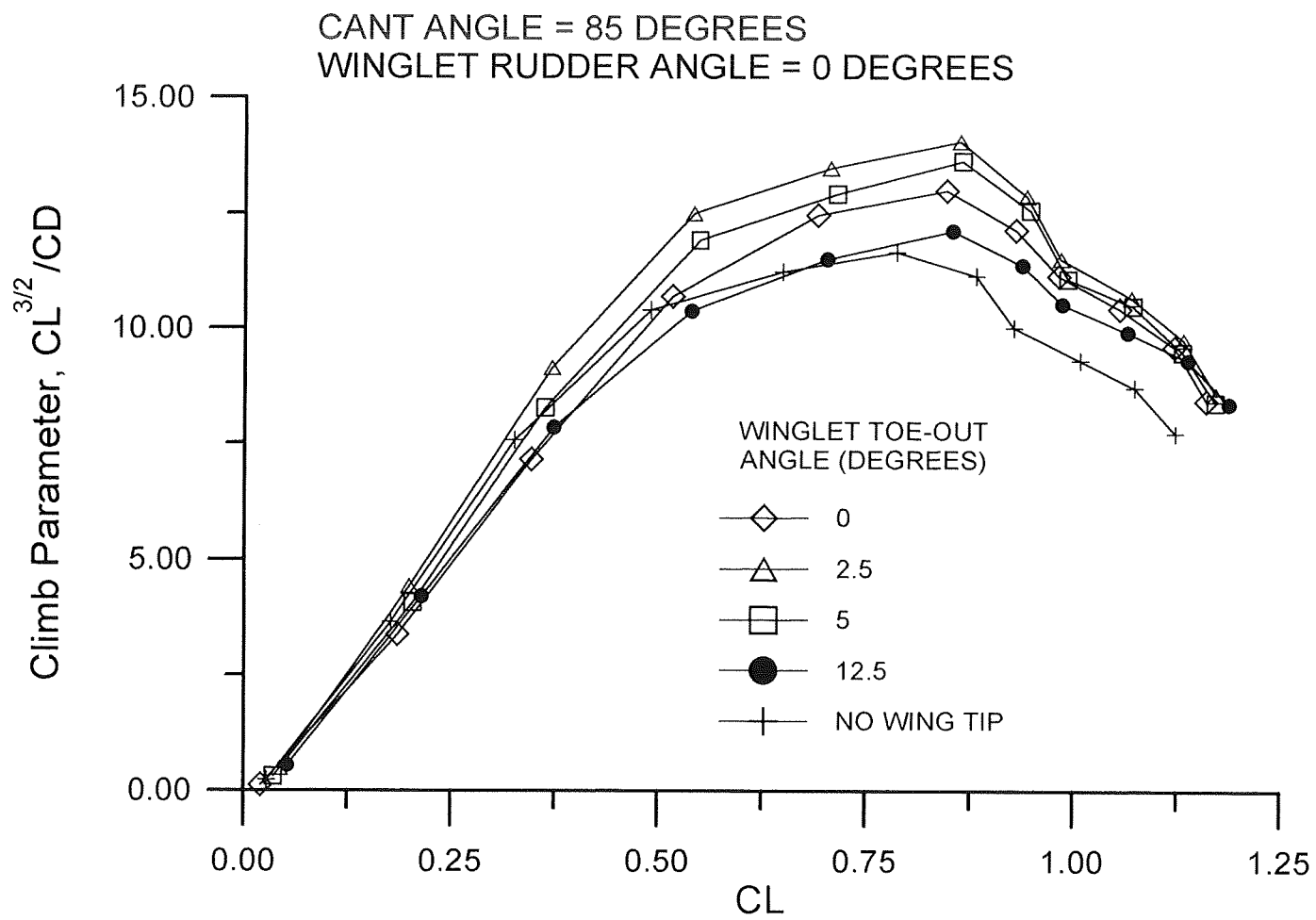


Figure 47. Effects of Toe-Out Angle on the Climb Parameter at a Cant Angle of 85 Degrees.
Reynolds Number $5.2 \times 10^5 \text{ ft}^{-1}$.

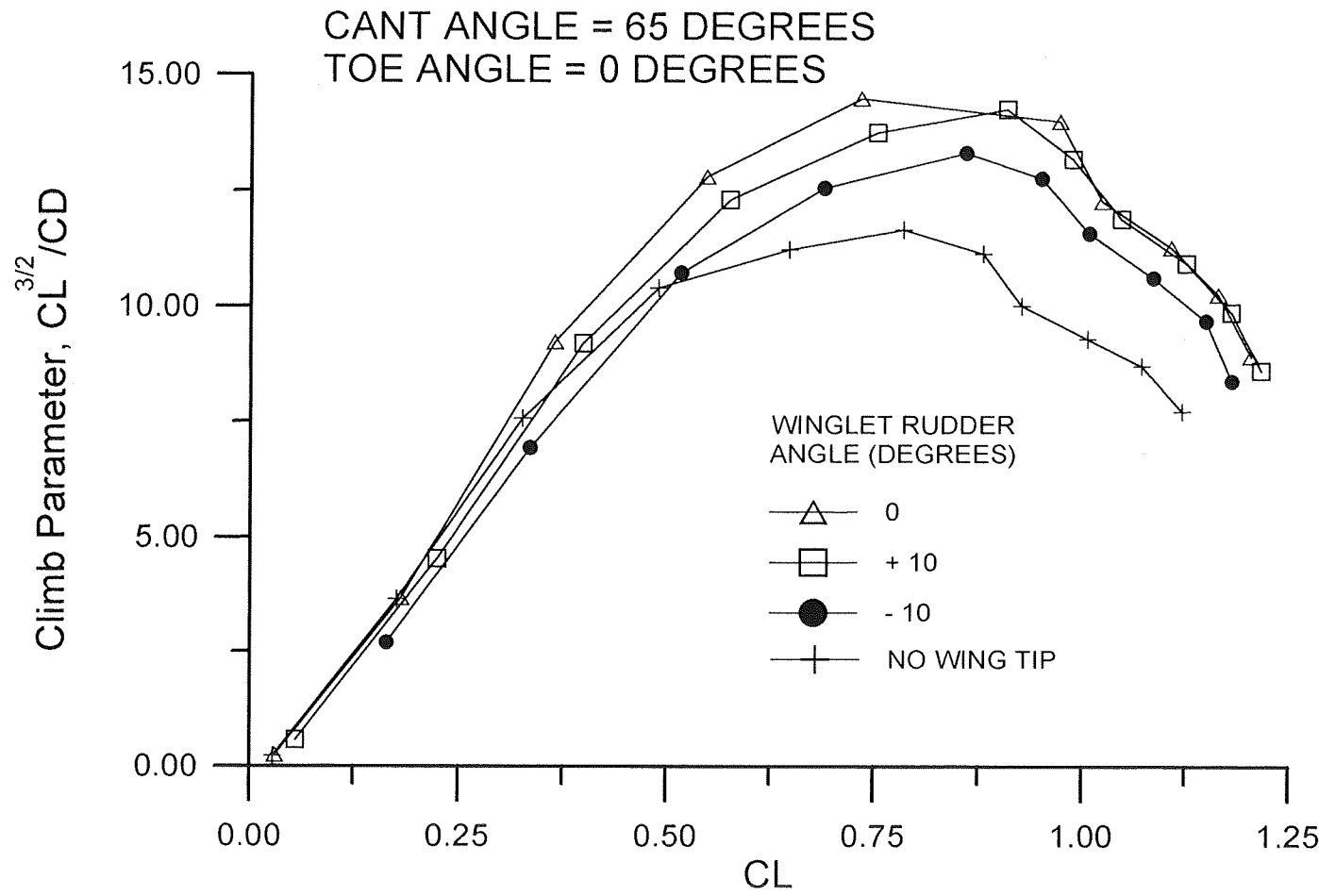


Figure 48. Effects of Winglet Rudder Angle on the Climb Parameter. Cant Angle 65 Degrees.
Toe-Out Angle 2.5 Degrees. Reynolds Number $5.2 \times 10^5 \text{ ft}^{-1}$.

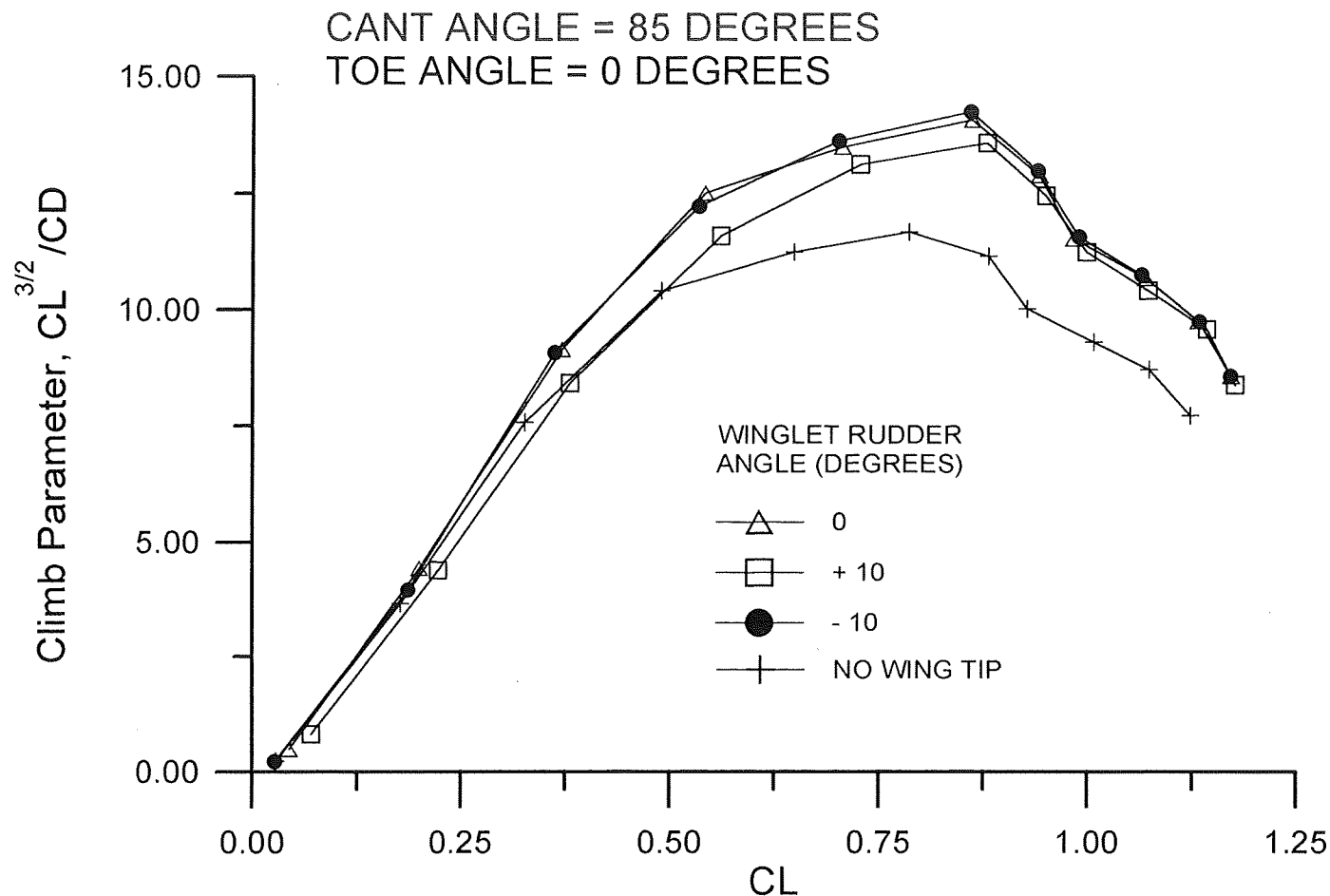


Figure 49. Effects of Winglet Rudder Angle on the Climb Parameter. Cant Angle 85 Degrees.
Toe-Out Angle 2.5 Degrees. Reynolds Number $5.2 \times 10^5 \text{ ft}^{-1}$.

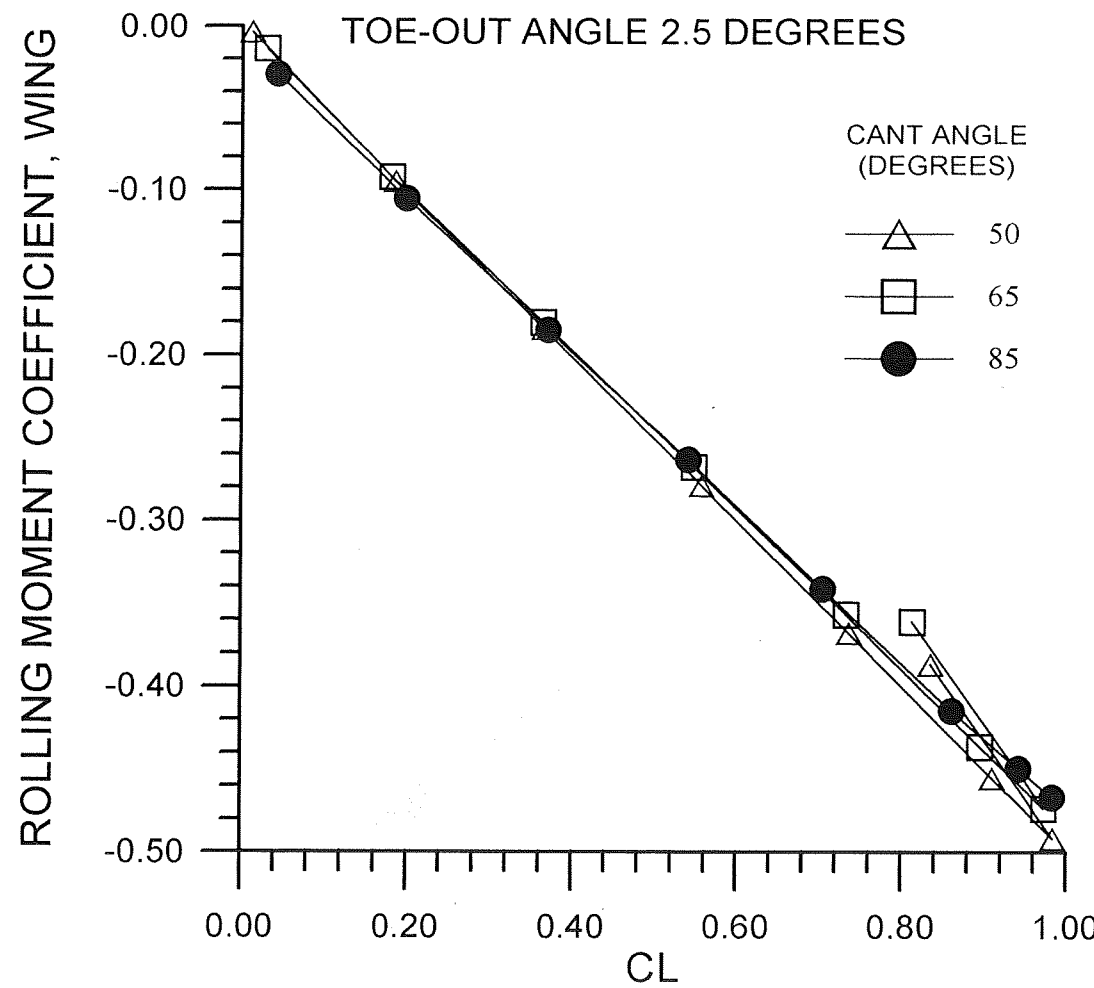


Figure 50. Effects of Cant Angle on the Rolling Moment. Toe-Out Angle 2.5 Degrees.
Reynolds Number $5.2 \times 10^5 \text{ ft}^{-1}$.

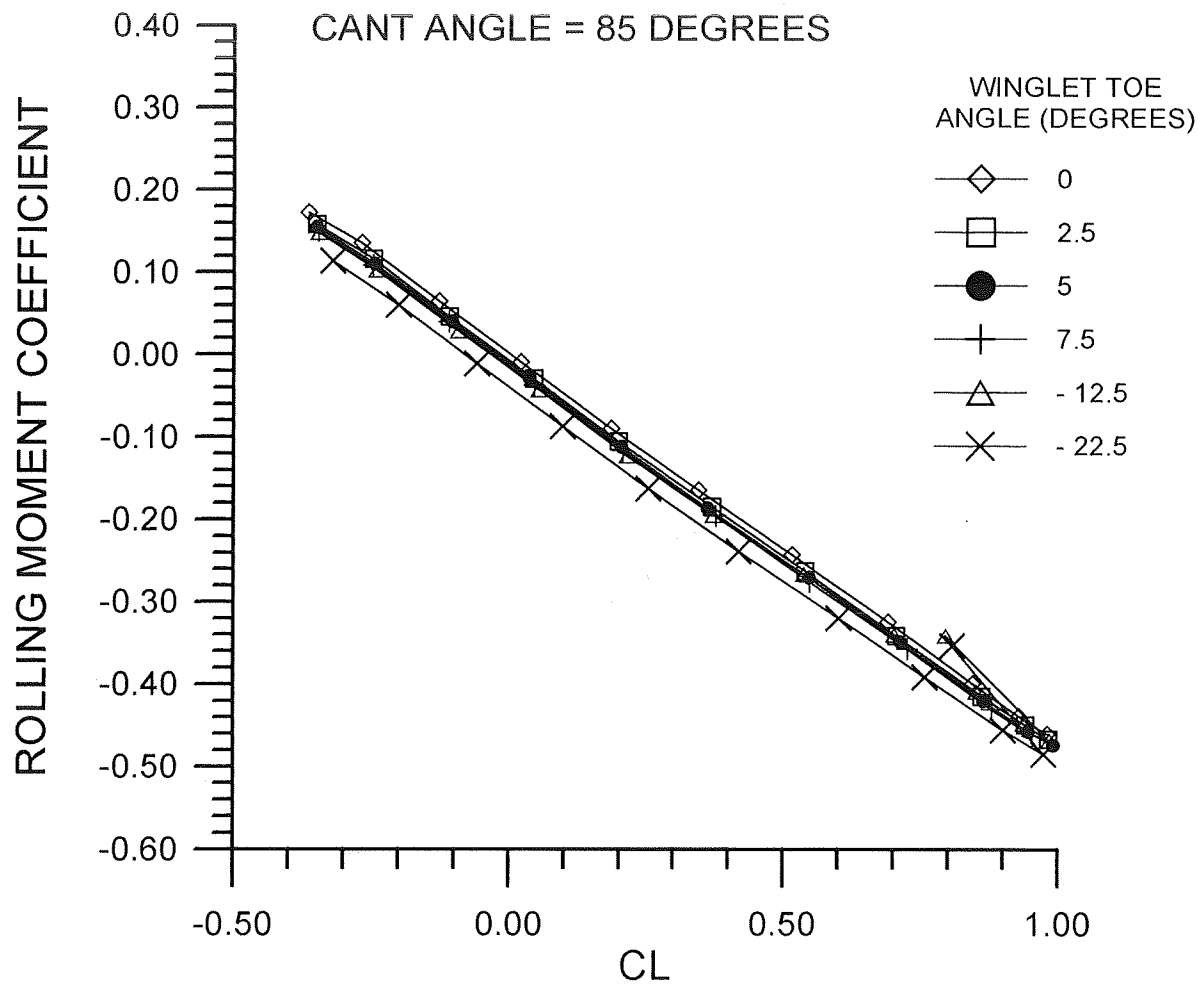


Figure 51. Effects of Toe-Out Angle on the Rolling Moment. Cant Angle 85 Degrees.
Reynolds Number $5.2 \times 10^5 \text{ ft}^{-1}$.

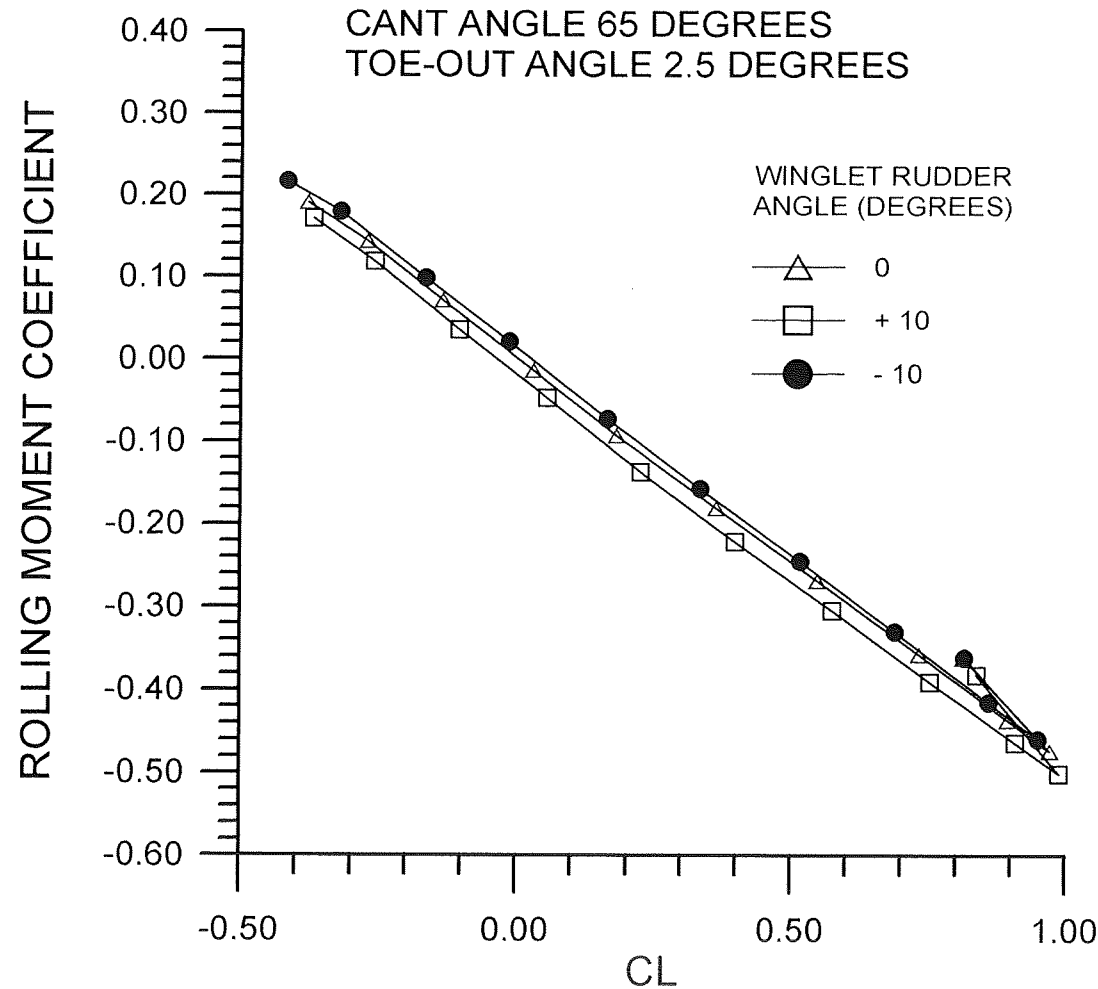


Figure 52. Effects of Winglet Rudder Angle on the Rolling Moment. Cant Angle 65 Degrees.
Toe-Out Angle 2.5 Degrees. Reynolds Number $5.2 \times 10^5 \text{ ft}^{-1}$.

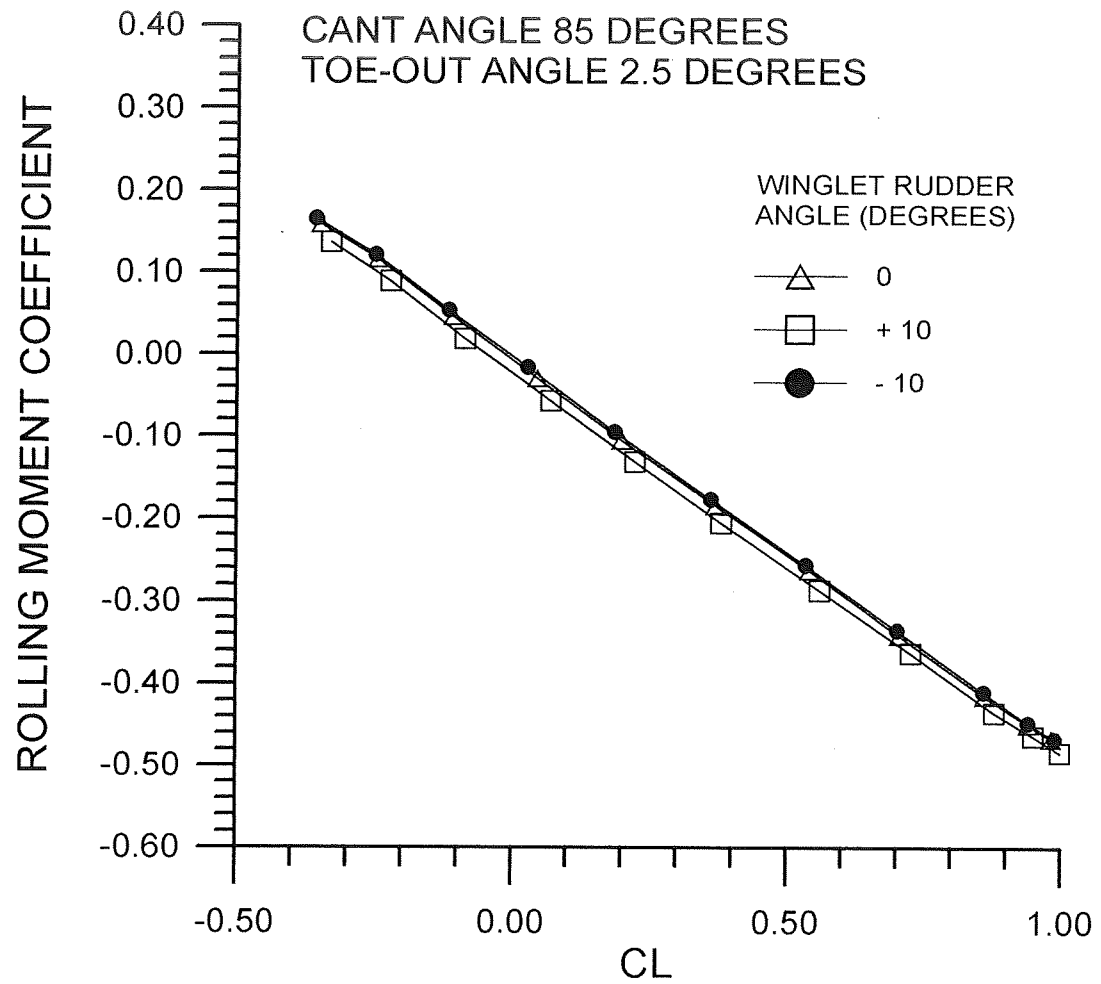


Figure 53. Effects of Winglet Rudder Angle on the Rolling Moment. Cant Angle 85 Degrees. Toe-Out Angle 2.5 Degrees. Reynolds Number $5.2 \times 10^5 \text{ ft}^{-1}$.

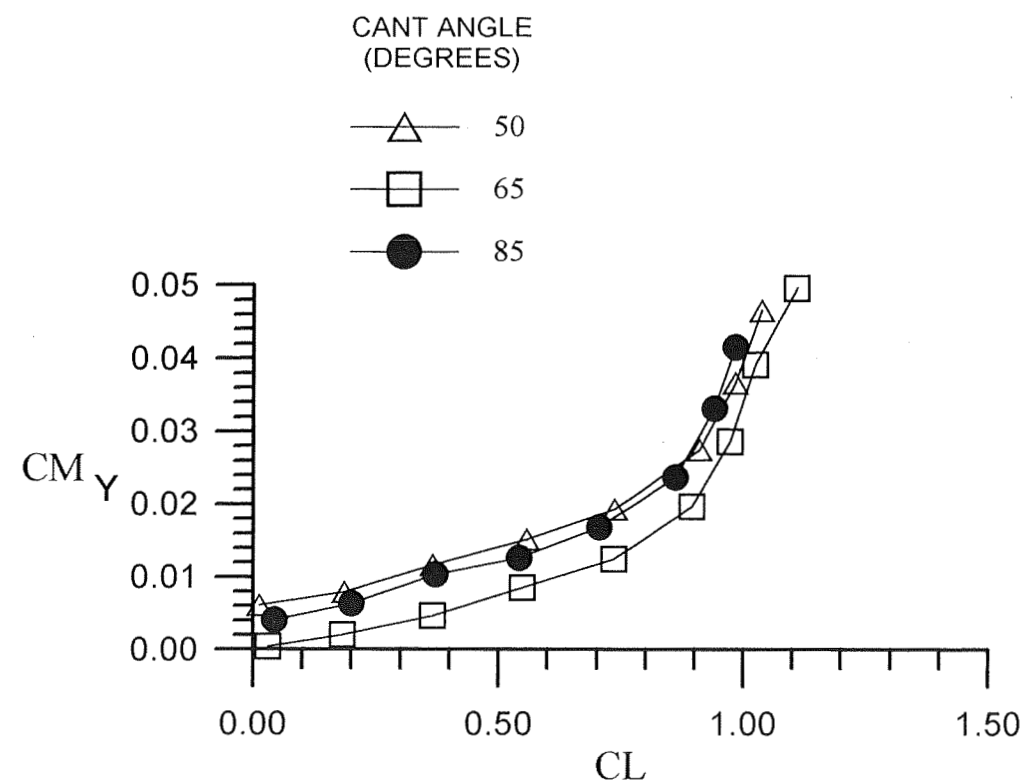


Figure 54. Effects of Cant Angle on the Yawing Moment at a Toe-Out Angle of 2.5 Degrees.
Reynolds Number $5.2 \times 10^5 \text{ ft}^{-1}$.

a-2

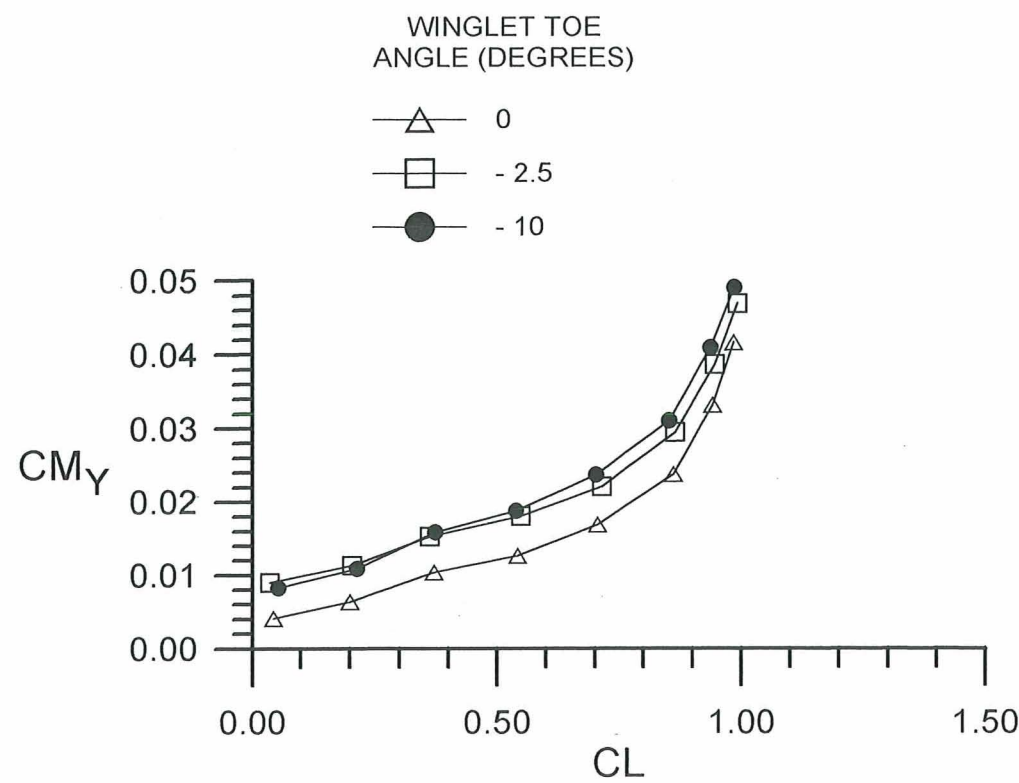


Figure 55. Effects of Toe-Out Angle on the Yawing Moment. Cant Angle 85 Degrees.
Reynolds Number $5.2 \times 10^5 \text{ ft}^{-1}$.

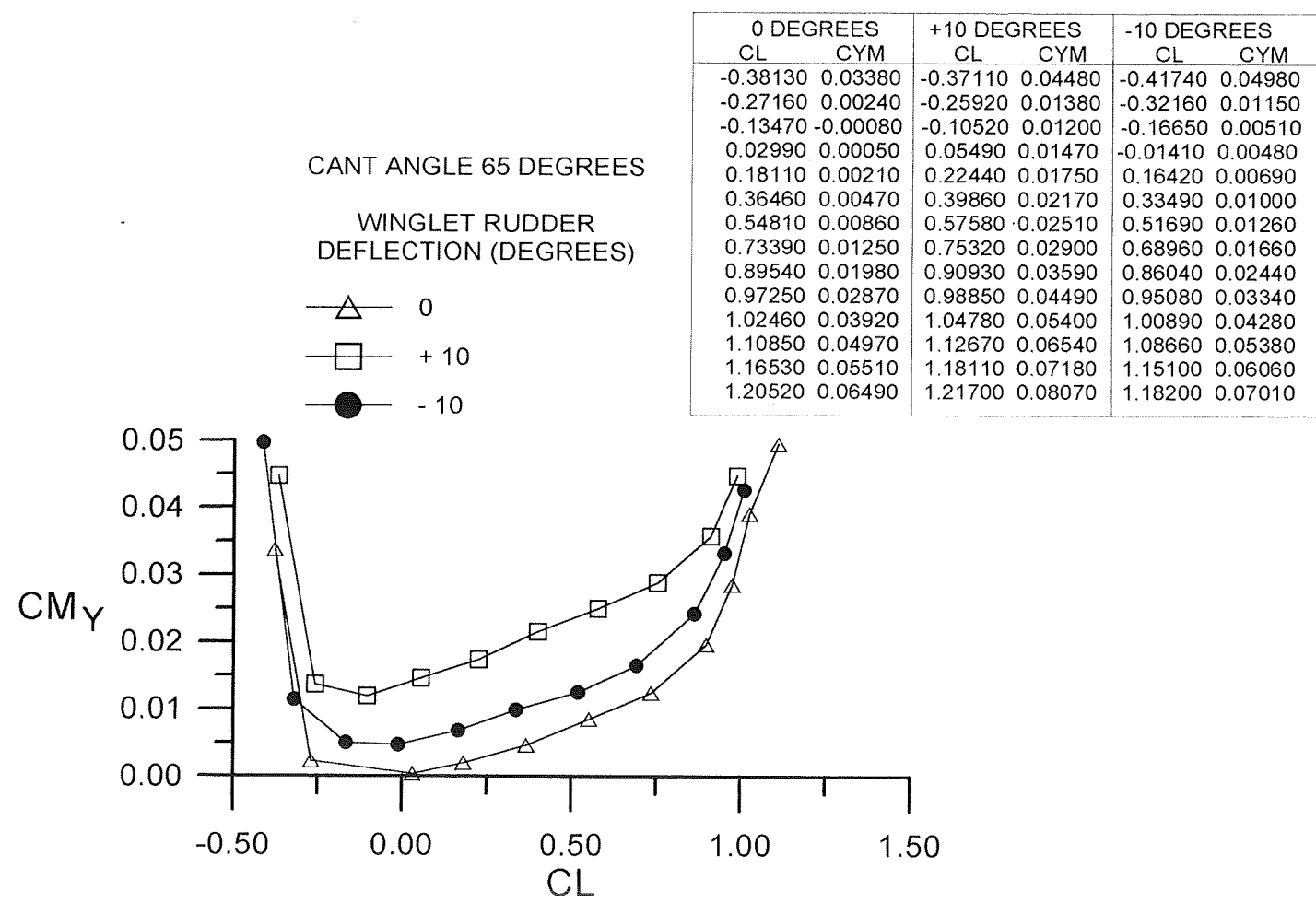


Figure 56. Effects of Winglet Rudder Angle on the Yawing Moment. Cant Angle 65 Degrees.
Toe-Out angle 2.5 Degrees. Reynolds Number $5.2 \times 10^5 \text{ ft}^{-1}$.

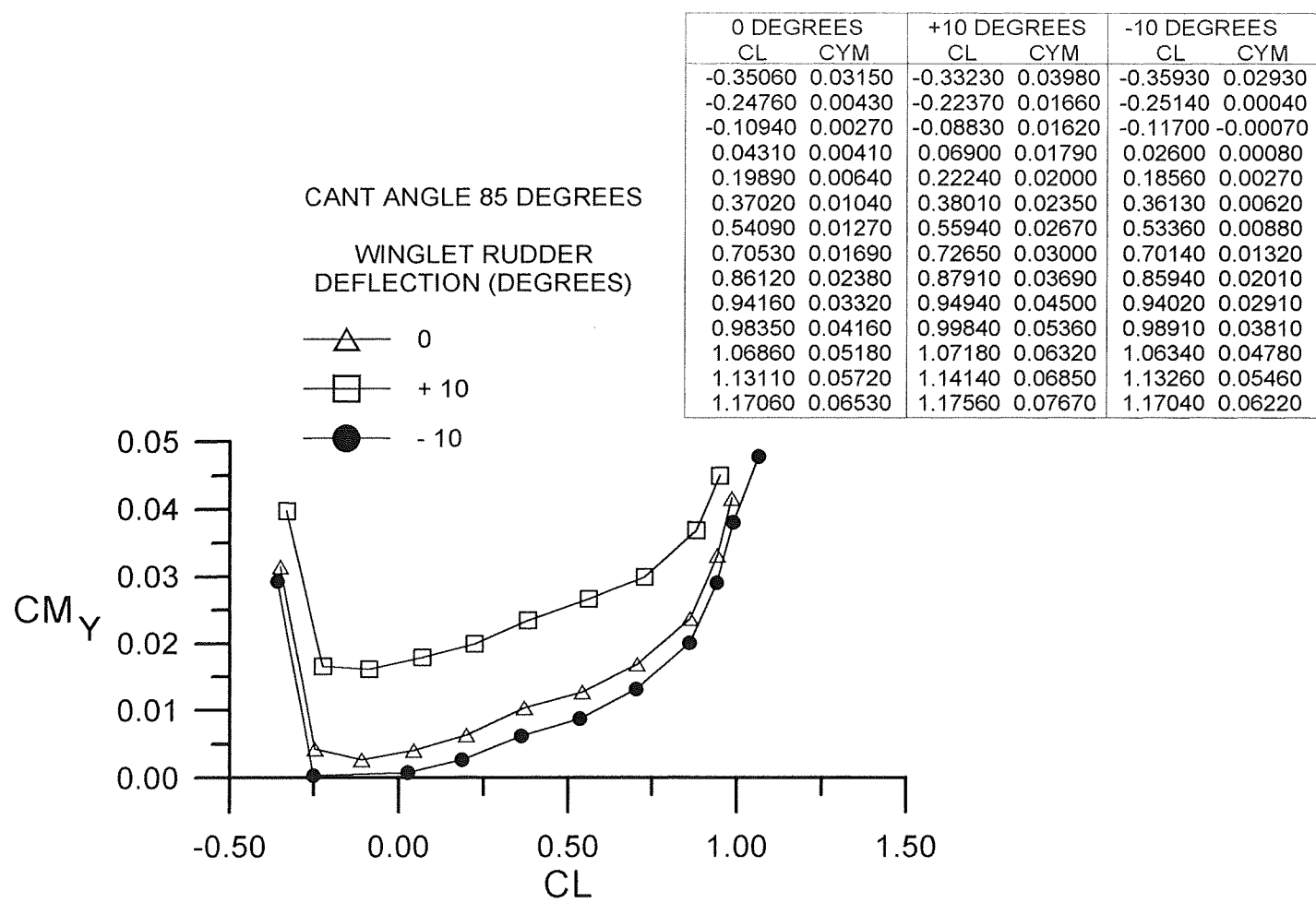


Figure 57. Effects of Winglet Rudder Angle on the Yawing Moment. Cant Angle 85 Degrees.
Toe-Out angle 2.5 Degrees. Reynolds Number $5.2 \times 10^5 \text{ ft}^{-1}$.

VITA

James David Colling was born on [REDACTED] in [REDACTED]. He graduated from W. B. Ray High School in Corpus Christi, Texas in May 1983. He received his Bachelor of Science degree in Aerospace Engineering from Texas A&M University in May 1988. In January 1989, he started his graduate work towards a Master of Science in Aerospace Engineering at Texas A&M University. In July 1989, he started full-time employment at Loral Space Information Systems, in Houston, Texas, as a programmer for the Space Shuttle Guidance, Navigation, and Control Flight Software. Later that year, he moved into an engineering position to provide support for the NASA Shuttle Program Office at the Johnson Space Center, Houston, Texas. In August 1993, he returned to Texas A&M University as a full-time student to finish his Masters degree in Aerospace Engineering. During this time, he worked as a contract engineer for High Performance Engineering, in Houston, Texas, to design and build a prototype 15-meter sailplane. This sailplane was flown at the World Soaring Championships which were held January 1995, in Omarama, New Zealand. His research work focused on winglets for high performance sailplanes. However, other research projects during the course of completing his Master of Science degree included: performance of counter rotating propellers on single engine airplanes, performance degradation of helicopter rotor blades due to leading-edge icing, the design and finite element analysis of a crescent shaped composite sailplane wing, and finite element stress and dynamic analysis of two and three blade propellers for single engine airplanes.

His permanent address is: 609 Barracuda, Corpus Christi, TX 78411.